AFML-TR-68-175

AD 673515

INVESTIGATION OF CRATER GROWTH AND EJECTA CLOUD RESULTING FROM HYPERVELOCITY IMPACT OF ALUMINUM SPHERES ON THICK ALUMINUM TARGETS

Lt. Col. Russell H. Smith
Air Force Institute of Technology

TECHNICAL REPORT AFML-TR-68-175

June 1968

This document has been approved for public release and sale; its distribution is unlimited.

Air Force Materials Laboratory
Air Force Systems Command
Wright-Patterson Air Force Base, Ohio

131

NOTICES

When Government drawings, specifications, or other data are used for any purpose other than in connection with a definitely related Government procurement operation, the United States Government thereby incurs no responsibility nor any obligation whatsoever; and the fact that the Government may have formulated, furnished, or in any way supplied the said drawings, specifications, or other data, is not to be regarded by implication or otherwise as in any manner licensing the holder or any other person or corporation, or conveying any rights of permission to manufacture, use, or sell any patented invention that may in any way be related thereto.

ACCESSION for

CFSTI WHITE SECTION ☑

DDC BUFF SECTION ☐

UNANNOUNCED ☐

JUSTIFICATION .....

.....

BY .....

DISTRIBUTION/AVAILABILITY CODES

DIST.	AVAIL. and/or SPECIAL	

Copies of this report should not be returned unless return is required by security considerations, contractual obligations, or notice on a specific document.

INVESTIGATION OF CRATER GROWTH AND EJECTA CLOUD RESULTING FROM HYPERVELOCITY IMPACT OF ALUMINUM SPHERES ON THICK ALUMINUM TARGETS

Lt. Col. Russell H. Smith
Air Force Institute of Technology

This document has been approved for public release
and sale; its distribution is unlimited.

FOREWORD

This report was prepared by Lt. Col. Russell H. Smith of the Air Force Institute of Technology as partial fulfillment of requirements for the degree Master of Science. The work was administered by Mr. Alan K. Hopkins of the Air Force Materials Laboratory under Project 7360, Chemistry and Physics of Materials, Task 736006, Hypervelocity Impact Studies.

The author gratefully acknowledges the assistance of members of the staff of the University of Dayton, particularly Mr. Hallock F. Swift for pertinent suggestions, timely advice and guidance, and the hypervelocity impact range staff headed by Mr. Lewis Shiverdecker, for their experimental assistance provided under Contract F33615-68-C-1138, Response of Materials to Pulse Loads. The author also wishes to thank his AFIT faculty advisors for their counsel and help in completing this report, and Capt. R. F. Prater of MAYH for his assistance and counsel in data reduction and establishing computer programs.

The manuscript was released by the author in June 1968 for publication as a Technical Report.

This technical report has been reviewed and is approved.

Herbert M. Rosenberg, Chief
Exploratory Studies Branch
Materials Physics Division
AF Materials Laboratory

ABSTRACT

An experimental investigation was conducted of crater growth and ejecta cloud formation from the impact of 3.2 mm aluminum spheres on thick aluminum targets at 7 km/sec. Crater growth and transient shape were determined through sequential flash x-rays. Growth followed a decaying exponential pattern, and the tangent angle to the crater wall at the target surface remained virtually constant. Relationships between ejecta-cloud parameters and crater diameters were investigated. Cloud-edge motion was determined and an effort made to determine particle origin. Velocities of discrete particles in the cloud were determined. No direct relationship between cloud parameters and crater dimensions could be established.

Contents

		Page
Forward		ii
Abstract		iii
List of Figures		vi
List of Tables		ix
I.	Introduction	1
	Background	1
	Purpose	6
II.	Postulated Model and Experimental Approach	9
	Postulated Model for Cratering in Thick Targets	9
	Approach to Testing the Model	11
	Hypervelocity Range	18
	Time Determination	21
	Switches	24
	Target Tank Pressure	26
	Measurement Techniques	28
	Projectiles and Targets	31
III.	Crater Growth Investigation	32
	X-ray Layout	32
	Radiographic Results	37
	Measurements of Final Craters	45
IV.	Ejecta Cloud Investigation	50
	Camera Layouts	50
	Framing Camera	50
	Image Converter Camera System	53
	Optical Results	55
	Framing Camera Photographs	55
	Image Converter Photographs	65

Contents (Continued)

Page

V. Discussion of Results, Conclusions, and Recommendations 71

Discussion of Results 71
Conclusions 82
Recommendations 85

Bibliography 86

Appendix A: Computer Program for Determining Crater Parameters from Ejecta Cloud Edge Positions . . 89

Appendix B: Raw Data and Sample Computations 99

Time Computations (Shot #2464) 99
Optical Data 100
Discrete Particle Computations 100
Image Converter Camera Data 101
Radiographs 101
Crater Depth Measurements 101

Appendix C: Atmospheric Drag Effects 111

Appendix D: Computer Program Sensitivity Tests 116

List of Figures

Figure		Page
1	Schematic of Hypervelocity Impact Cratering Process	10
2	Typical Early-Time Photograph of Ejecta Cloud	12
3	Simulated Ejecta Curves Produced by Constant-Velocity Particle Ejection Program	13
4	Graphical Presentation of Cloud-Edge Computer Program Routine	15
5	Typical Late-Time Photograph of Ejecta Cloud	17
6	Ejecta Impact Pattern on Paper Placed on Face of Vertical X-ray Cassette Located 21.6 cm Uprange from Target	19
7	Graphical Presentation of Scheme for Solution from Discrete Particle Travel	19
8	Schematic of AFML Light-Gas Fun Range	20
9	Photograph of Dynafax Camera and Associated Winker System	23
10	Signal-Flow Diagram for Experiments Employing X-rays and Framing Camera	25
11	Signal-Flow Diagram for Experiments Employing Image Converter Cameras	27
12	Photograph of Microviewer Used for Analyzing Optical and X-ray Films	29
13	Photograph of Equipment Used for Measuring Crater Depths and Diameters	30
14	Diagram of Crater Measurement Technique	30
15	Positioning of Vertical X-ray Heads	33
16	Positioning of Horizontal X-ray Heads	34

List of Figures (Continued)

Figure		Page
17	Schematic of Target and Vertical X-ray Cassette Holders	35
18	Photograph of Target and Vertical X-ray Cassette Holders	37
19	Radiographs of Crater Profile During and After Shot #2386 (Vertical X-ray Setup)	38
20	Radiographs of Crater Diameter During and After Shot #2386 (Horizontal X-ray Setup)	39
21	Angle Between Tangent to Crater Wall at Original Target Surface and Target Face	41
22	Plot of Crater Diameter Growth	43
23	Plot of Crater Depth Growth	44
24	Photographs of Cratered Targets	46
25	Photograph of Beckman & Whitley Model 300 Framing Camera with Example of Picture Format	51
26	Schematic of Arrangement of Beckman & Whitley Model 300 Framing Camera with Light Source and Kerr Cell	51
27	Integrated Schematic of Instrumentation System Used in Experiments Employing Framing Camera and X-ray Setups	52
28	Schematic of Optical Alignment of Image Converter Cameras	54
29	Photograph of Image Converter Cameras and Mirrors in Position on the Range	54
30	Examples of Early-Time Framing Camera Photographs of Ejecta Cloud from Shot #2385 with Times from Impact (μ sec)	56

List of Figures (Continued)

Figure		Page
31	Comparison of Observed Cloud Edge with Computer-Produced Constant-Velocity and Decelerating Particle Curves.	59
32	Examples of Late-Time Framing Camera Photographs of Ejecta Cloud from Shot #2387 with Times from Impact (μ sec)	61
33	Crater Parameters vs. Time Determined from Analysis of Discrete Particle Motion, Shot #2387	64
34	Image Converter Photographs of Ejecta Cloud and Calibration Grid, Shot #2464	66
35	Plots of Ejecta Cloud Base and Throat Growth	70
36	Comparison of Ejecta Cloud Base and Throat Data with Crater Diameter Growth Curves	75
37	Radiographs of Crater Profile During and After Shot #2384 (Vertical X-ray Setup)	104
38	Radiographs of Crater Diameter During and After Shot #2384 (Horizontal X-ray Setup)	105
39	Radiographs of Crater Profile During and After Shot #2385 (Vertical X-ray Setup)	106
40	Radiographs of Crater Diameter During and After Shot #2385 (Horizontal X-ray Setup)	107
41	Radiographs of Crater Profile During and After Shot #2387 (Vertical X-ray Setup)	108
42	Radiographs of Crater Diameter During and After Shot #2387 (Horizontal X-ray Setup)	109

List of Tables

Table		Page
I	Check of Accuracy of Cloud-Edge Computer Program	16
II	X-ray Film Measurements of Crater Diameter and Depth	42
III	Direct Measurements of Crater Diameter and Depth	47
IV	Comparison of Crater Diameters Scaled According to the Cube Root of Impact Energy	48
V	Cloud-Edge Computer Program Outputs, Shot #2385	58
VI	Crater Parameters Determined from Discrete Ejecta Particle Movement, Frames 36 to 44, Shot #2387	63
VII	Cloud-Edge Computer Program Outputs, Shot #2464	68
VIII	Purpose, Instrumentation, and General Results of Shots	72
IX	Results of Cloud-Edge Computer Program Sensitivity Tests	79
X	Data Used in Discrete Particle Investigation	102
XI	Film and Real-Space Coordinates of Cloud-Edge "C" from Image Converter Photograph, Shot #2464	103
XII	Crater Measurement Raw Data	110
XIII	Kinetic Thickness and Drag Coefficient	112
XIV	Approximate Distances Traveled by Various Size Particles in Losing 5% of Initial Velocity of 7 km/sec in Atmospheric Pressures of 25.2 and .09 Torr	115
XV	Detailed Results of Computer Program Sensitivity Tests	117

INVESTIGATION OF CRATER GROWTH AND EJECTA CLOUD RESULTING FROM HYPERVELOCITY IMPACT OF ALUMINUM SPHERES ON THICK ALUMINUM TARGETS

I. Introduction

Background

With the advent of the space age, the problem of material damage caused by projectiles impacting targets at hypervelocities became one of paramount concern. Earlier calculations, based on Bernoulli's equation for incompressible fluid flow, were carried out by Pugh in the United States and by Hill et al. in Great Britain in connection with the "shaped-charge" developed in World War II for penetrating armor. These calculations were found to be inapplicable to the problem of randomly oriented bodies impacting solid targets. In 1958, employing classical hydrodynamics of compressible media as a starting point, Bjork developed what is generally considered the first comprehensive theoretical treatment of the problem of hypervelocity impact and resulting crater formation. Bjork used a digital computer to obtain numerical solutions to the two-dimensional, time-dependent hydrodynamic equations for a compressible medium (Ref 1:220). Subsequently, the hydrodynamic approach was employed by Walsh and Tillotson (Ref 30) and by Riney (Ref 24).

Concurrently with the development of these theories, experimenters in laboratories both here and abroad started amassing data which might presumably serve to support or refute these or other theories. An idea of the acceleration of the pace of theory development and experimentation in hypervelocity impact can be inferred from the volumes reporting the proceedings of the biennial Hypervelocity Impact Symposia. The unclassified results of the Second Symposium occupy a single volume, while the unclassified proceedings of the Seventh Symposium fill six separate volumes, each of size comparable to that of the single volume resulting from the Second Symposium.

Unfortunately, much of the data thus acquired and presented is not suitable for completely testing the cited theories. The practical limit on velocities attainable in light-gas guns launching projectiles of known dimensions and mass is currently on the order of 10 km/sec. Such impacts will generate and sustain pressures sufficient to ensure true hydrodynamic conditions for only a few microseconds. Thus a large part of the crater formation process in laboratory experiments occurs at lower pressures where material properties cannot be ignored. While conceding that in the final stages of crater formation material characteristics may become significant, Olshaker and Bjork dismiss the problem of determining precisely at what point in the process this transition occurs in the belief that at the higher meteoroid velocities of interest (11 to 72 km/sec), hydrodynamic effects will far outweigh any late stage strength effects (Ref 19:225). The treatment

of the problem by Walsh and by Riney is different in that both terminate the hydrodynamic computations well before the crater has stopped growing. Implicit in both treatments is the assumption that the strength of the impacted material cannot be ignored, even at arbitrarily high impacting velocities (Ref 11:239).

From their observations, most experimenters echo Riney's and Walsh's insistence on including consideration of target strength in any tenable theory of crater formation. Rae and Kirchner state the majority view succinctly when they write:

> ...The establishment of a crater of fixed size implies that material has been brought to rest, and... there is no mechanism for accomplishing this feat within the framework of an inviscid theory. Thus it appears that at large time a transition must be made to a theory which accounts for the strength of the target.... Thus we ought to assign as a boundary of the hydrodynamic theory some level of pressure comparable with target strength (Ref 23:210).

Precisely what this boundary represents is, unfortunately, not at all clear. That it is in some way related to target strength is quite well established. Several investigators have found that cratering efficiency in terms of projectile energy per unit crater volume is directly proportional to the Brinell hardness number of the target material over a wide range of materials and values of hardness (Ref 10:165). The influence of the density of either the target or the projectile remains a subject of considerable controversy. Expressed opinions range from quadratic relations (between crater volume and projectile density) to no effect (Ref 4:334). Frasier et al. find good

agreement between Walsh's hydrodynamic treatment and their experimental data down to pressures about an order of magnitude above the Hugoniot elastic limit of the target (Ref 8). Sorensen concludes that all metal-on-metal impacts up to 7.5 km/sec produce crater volumes which are inversely proportional to target shear strength to the 0.845 power (Ref 26). Several investigators employ the ratio of projectile velocity to target dilational wave velocity (v/c) in the empirical equations which they derive, but there is little agreement as to how this ratio enters the equation. Maiden et al. find that penetration varies as $(v/c)^2$ (Ref 18); on the other hand, Summers et al. conclude that it varies as $(v/c)^{2/3}$ (Ref 27).

On the fringes of the empiricist group stand a few who deny the validity of the hydrodynamic approach in toto. For example, Feldman finds that the ratio of kinetic energy to crater volume is the same for jets and pellets and therefore concludes that hypervelocity impact is basically a problem in plastic flow, not shock wave phenomena (Ref 7). Engle proposes that hypervelocity impact is best treated by the analogy of liquid droplets impacting a fluid surface (Ref 6). And Pond et al. find that major proportions of kinetic energy are expended in strain-hardening various metals, a viewpoint which is in marked contrast to the hydrodynamic approach (Ref 22).

But by far the majority of experimenters share the more moderate view that although hypervelocity impact may be amenable to hydrodynamic treatment, still for impact velocities at least up to the

limits currently attainable, target strength is significant in determining final crater dimensions. In fact, Kineke and Richards find no indication that the influence of mechanical strength is decreasing for impacts up to 15.5 km/sec (Ref 15).

A report published by Hermann and Jones in an effort to analyze and correlate the various experimental data aptly summarizes the state of confusion currently existing:

> A great deal of experimental data has been published by a number of laboratories, and considerable theoretical work has appeared during the last few years. Limited comparisons of data from one laboratory with those from another and of experimental data with theoretical predictions have shown some large discrepancies. Considerable confusion exists because, except in a few instances, the data from one laboratory are not directly comparable with those from another since identical materials, projectile shapes, and velocity ranges were not used. Each laboratory has produced a different empirical expression which was found to fit the limited range in experimental parameters explored at the laboratory. The empirical expressions are more or less contradictory, and when extrapolated to velocities of interest in space applications, lead to large disagreements in predicted penetrations (Ref 12:390).

Although this particular report was published some five years ago, the situation does not appear to have improved significantly since then.

In his Summary of Theoretical and Experimental Studies of Crater Formation presented at the Sixth Hypervelocity Impact Symposium, Eichelberger makes some penetrating (and occasionally caustic) comments on this apparent inability of theoreticians and experimentalists to find a common meeting ground to permit the

testing of theory with meaningful experimental data. He concedes that because of velocity limitations, the early or purely hydrodynamic stages will probably not vary sufficiently to permit a clearcut choice between theories. Rather, he says, "It is more likely that experiments involving detailed observations of transient conditions during the later stages of the crater formation process will provide decisive comparisons" (Ref 5:688-689).

Purpose

In all the welter of reported observational data, surprisingly little attention has been paid to the cloud of ejecta which inevitably accompanies and results from the process of crater formation. Apparently most experimenters have considered the cloud only an annoying obstacle preventing their direct viewing of the crater formation process in which they were primarily interested. Yet it seems plausible that since the ejecta cloud is intimately associated with whatever process or processes are operative in forming the crater, valuable information about these processes might be obtained by careful examination and analysis of pictures taken of the ejecta cloud during the cratering process.

If, as Riney suggests, the mechanism of crater formation is essentially one of cavitation (Ref 24:161), then determination of the trajectories of the particles thus ejected should enable one to acquire some information on the forces and conditions responsible for their

ejection. Kinslow's experimental observations support Riney's views. He infers that as the expanding shock wave becomes detached from the crater, material flows along the walls of the crater and is ejected at velocities up to eight or ten times the impacting velocity of the projectile (Ref 16:279). While agreeing in principle with this view, most other experimenters place a lower value on the maximum ejecta velocity of perhaps triple the impact velocity (Refs 14; 17). Kineke also notes that as ejection continues, the ejected pieces increase in size and decrease in velocity (Ref 14:351-352). Detailed studies of the ejecta produced by hypervelocity impact of metallic spheres into rock targets conducted by Gault et al. confirm this finding of generally monotonically increasing ejecta size combined with decreasing ejecta velocities. Gault also finds that for basalt ejecta, following the initial jetting phase, the angle of ejection (measured from the target face) increases to 60 degrees, decreases to about 50 degrees, and finally tends toward 90 degrees (Ref 9:446-449). This departure from a monotonically increasing ejection angle has apparently not been observed or reported in the ejecta from metallic targets. But as noted previously, the ejecta patterns from metallic targets have not been studied as extensively as has basalt ejecta.

These observed variations in ejecta parameters with time and their inferred dependence on conditions existing within the crater at the time of ejection reinforce the view that a detailed examination and analysis of sequential pictures of the ejecta cloud might provide

information on crater parameters as a function of time during the crater formation process. The purpose of this study, then, was to examine possible relationships between ejecta cloud parameters and crater growth and shape.

The study was designed in two independent but closely related phases. In a series of hypervelocity impact experiments crater growth data would be obtained through the use of a battery of sequential flash x-rays. At the same time, optical photographs would be made of the ejecta cloud resulting from the impact. It was felt that accurate measurement of changing cloud-edge and ejecta particle positions in sequential optical photographs would yield information on ejecta particle velocities and times and points of ejection. Concurrently, sequential x-ray photographs (radiographs) of crater profile and plan would provide information on crater parameters and shapes as a function of time. Comparison of ejecta parameters determined from cloud photographs with radiographic data on crater growth would permit correlation of the two phenomena. The establishment of a significant correlation would provide an extremely useful technique to experimentalists concerned with the problem of testing theoretical predictions of crater growth in thick metallic targets.

II. Postulated Model and Experimental Approach

Postulated Model for Cratering in Thick Targets

In order to establish logical relationships between crater formation and the resulting ejecta cloud, it was necessary to postulate a model of crater formation. Despite the cited disagreements on the relative importance and effects of material properties, most investigators agree that crater formation in thick targets occurs in the following stages. The projectile penetrates the target surface creating a very intense shock wave. Cavitation is initiated behind the shock wave. The velocity of the expanding crater surface decreases, and the shock wave detaches from the surface. Material flows along the crater walls and is ejected. The crater continues to expand at a decreasing rate until crater growth is arrested by the dynamic strength of the material. The amplitude of the expanding shock wave decreases as energy is dissipated throughout the material until the wave decays into an elastic wave (Ref 16:279).

A simplified schematic of the outlined cratering process is presented in Fig. 1. Consideration of the previous discussion and crater geometry leads to the following set of assumptions constituting a proposed model for crater and ejecta cloud formation:

a. Material departs the crater as ejecta along vectors tangent to the crater wall at or very close to the original target

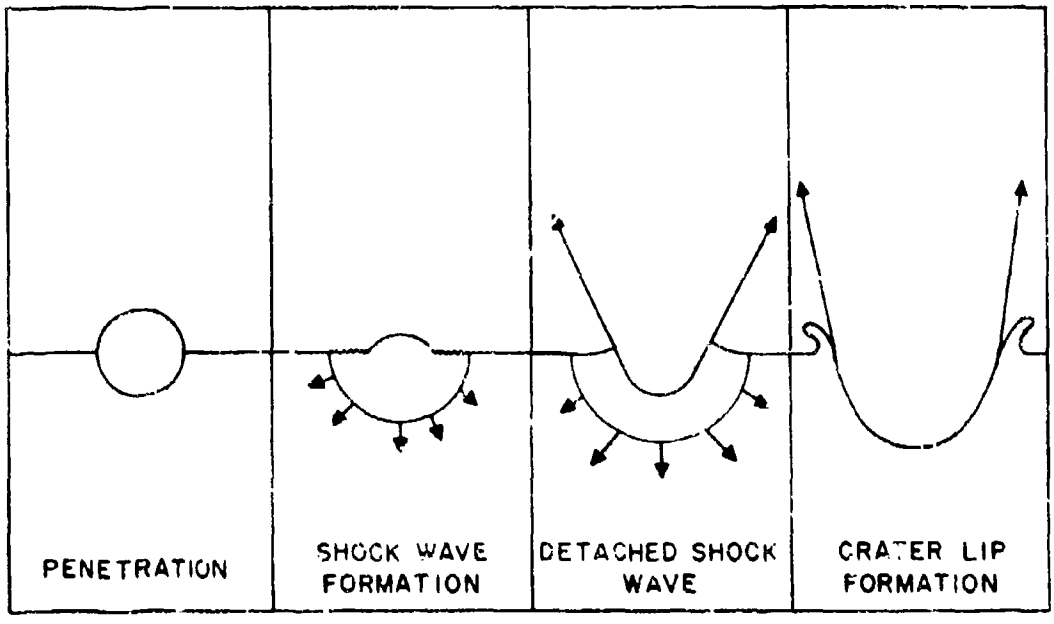

Fig. 1. Schematic of Hypervelocity Impact Cratering Process

surface. Therefore, the points of particle ejection are virtually identical to the crater radius at all times.

b. At any instant, particles are being ejected at nearly identical velocities.

c. As the crater enlarges, the angle of ejection increases toward the vertical with respect to the target face.

d. As the pressure dissipates, the velocity of ejection decreases.

e. No significant pressure field exists outside the crater to alter particle velocity. Therefore, after being ejected, particles travel in straight lines at constant velocities except for deceleration due to atmospheric drag effects.

Approach to Testing the Model

As the ejection process occurs, the characteristic shape of the ejecta cloud varies with time. For purposes of the following discussion, "early time" refers to times less than approximately 10-15 microseconds after impact. The remainder of the ejection process will be referred to as "late time". In early time, the cloud edges form smooth curves which slope inward toward the cloud centerline from their intersection with the target face. After reaching a limiting point of minimum width of the "throat" of the cloud, the cloud edges slope back away from the cloud centerline and become less distinct with increasing distance from the target face (Fig. 2). To a first approximation, the cloud appears symmetrical about a centerline which presumably coincides with the trajectory of the impacting projectile. At this stage in the process, discrete particles forming the ejecta cloud are not discernible. However, it would seem logical that the cloud edges constitute lines of discrete although indistinguishable particles. If the velocities of ejection are monotonically decreasing at this stage, and if the particles can be assumed to travel at relatively constant velocity following their ejection, then it follows that the same particles which form the cloud edge at one point in time must necessarily form the cloud edge in subsequent times. Hence it should be possible to use a set of sequenced photographs of a developing ejecta plume to reconstruct the straight-line trajectories of individual particles. The distance traveled by a particle between

Fig. 2. Typical Early-Time Photograph of Ejecta Cloud [Magnification = 5.3 (nom); Time = 1.03 μ sec; Velocity of Impact = 7 km/sec]

cloud photographs is in the same ratio as the time between frames. Once the correct geometrical relationships are established, particle velocities can be uniquely determined. By extending the straight line of each particle trajectory back to the target face, its origin, ejection time, and angle of ejection can all be determined.

In order to test the feasibility of establishing the required geometrical relationships, a simple computer program was written to eject hypothetical particles which travel at constant velocity. Particle origin was moved outward with time (simulating crater growth). Velocities of ejection were monotonically decreased, and angles of ejection from the target face were monotonically increased. A plot of

particle positions thus determined as a function of time for three times appears as Fig. 3, with straight lines indicating particle trajectories.

The problem of constructing the particle-trajectory straight lines by working backward from cloud photographs was initially attempted graphically. However, as can be seen from Fig. 3, the trajectory lines intersect the cloud edge curves at such low angles that a graphical solution is subject to considerable error. Consequently, a computer program was developed to solve the problem by repeated iteration.

The cloud edges were fit by a standard least squares program to polynomials of order 2 through 10, and the best fit selected to represent the cloud edge in the program. The x-axis was placed

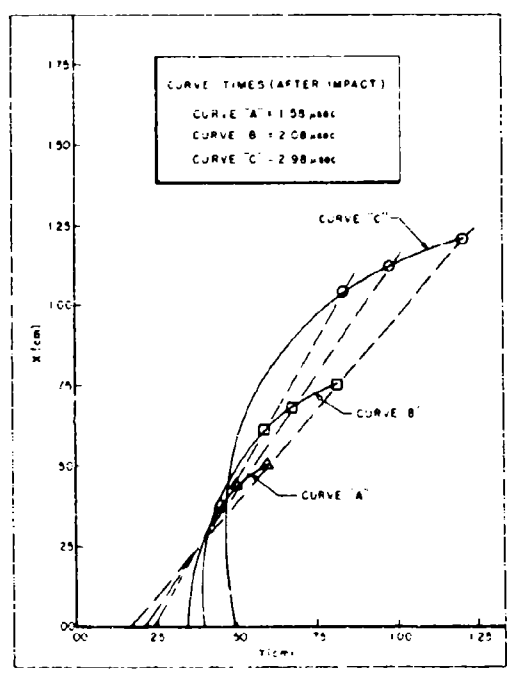

Fig. 3. Simulated Ejecta Curves Produced by Constant-Velocity Particle Ejection Program

along the symmetry axis of the cloud, with x-distance increasing away from the target face (uprange). The y-axis was placed on the target face, with origin at the intersection of the x-axis with the target face. With the three cloud curves designated A, B, and C in order of increasing time, a point was arbitrarily selected on the A curve. A logical estimate was made of the position of origin on the target face. The point of intersection with the B curve of a straight line from the assumed origin through the point on the A curve was then determined by standard Newton-Raphson iteration techniques. The intersection of this line with the C curve was then similarly determined. The distances between curve intersections were compared with the time differences between the frames represented by the three curves. On the basis of the resultant error, the assumed origin was corrected to bring the distance ratios into agreement with the interframe times, and the iteration process continued until acceptable agreement was achieved. A graphical portrayal of the scheme is presented in Fig. 4.

The accuracy of the completed program (Appendix A) was checked against the artificial cloud generation program with the results shown in Table I. Since the resulting errors appeared to be within reasonable limits and considerably less than might be expected from a purely graphical solution, use of the program was considered warranted.

In later times during the ejection process, as increasingly larger particles are ejected, the characteristic ejecta cloud shape

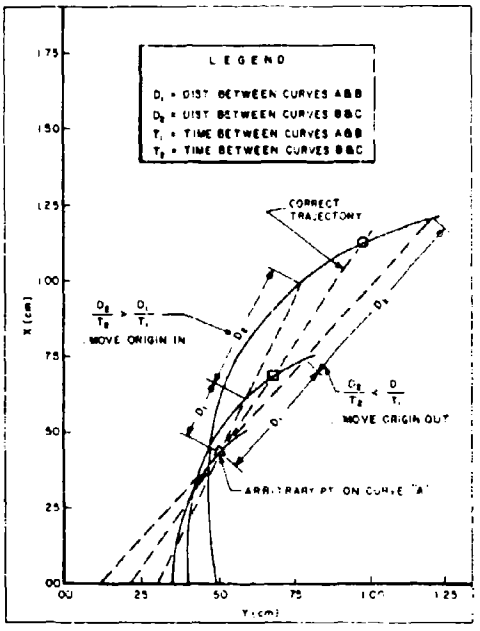

Fig. 4. Graphical Presentation of Cloud-Edge Computer Program Routine

undergoes marked alterations (Fig. 5). The bottom, inward-sloping segment of the cloud edge gradually disappears until the narrowest portion or throat of the cloud coincides with its intersection with the target face. The cloud now consists largely of discrete and readily discernible particles. Inclusion of these particles in the formerly smooth cloud edge causes the cloud edge to appear more ragged. Rather than a line of indistinguishable particles it now represents a train of photographically resolved fragments. Because the cloud edge is not clearly defined and because its shape and dimensions vary only a slight amount in the later stages of ejection, it was not felt advisable to attempt to determine particle trajectory from the cloud edges in

TABLE I

Check of Accuracy of Cloud-Edge Computer Program

Time of Ejection (μ sec)	Origin			Angle of Ejection			Velocity of Ejecta		
	Actual Input (cm)	Program Output (cm)	Error (%)	Actual Input (Deg)	Program Output (Deg)	Error (%)	Actual Input (km/sec)	Program Output (km/sec)	Error (%)
.980	.28641	.28773	+0.46	65.963	66.196	+0.35	4.9652	4.9429	-0.45
.880	.26688	.26401	-1.08	63.231	62.881	-0.55	5.1797	5.2242	+0.86
.780	.23655	.23693	+0.16	59.799	59.865	+0.11	5.4770	5.4985	+0.39
.680	.20622	.21587	+4.68	55.358	56.534	+2.12	5.9164	5.7702	-2.47

Fig. 5. Typical Late-Time Photograph of Ejecta Cloud [Magnification = 0.34 (nom); Time = 37.84 μ sec; Velocity of Impact = 7 km/sec]

this portion of the ejection process. Rather, it was decided to attempt to identify and follow specific particles from frame to frame.

True lateral particle motion in the y-direction is recorded only for those particles on the cloud edge. (All other particles possess a velocity vector toward or away from the camera.) First consideration would then indicate that only particles lying on the cloud edge could be used for velocity determination. However, if the particles are ejected from the crater wall with some outward velocity vector, then the ejecta cloud must at all times be hollow. Experimental evidence supports this conclusion. Ejecta impacts recorded on the uprange wall of the target tank invariably reveal a roughly

circular pattern, with virtually no evidence of significant impacts within this circle. This pattern of ejecta impact was recorded on a clean piece of paper affixed to the downrange face of the vertical x-ray cassette (to be described later) (see Fig. 6).

If the cloud is indeed hollow, as this evidence suggests, then all particles visible in the ejecta cloud must in fact be on or very close to the edge of the cloud. And if symmetry can be assumed, the radial motion of any particle between frames must be represented by the y-motion of the cloud edge between corresponding x-positions in the two frames (see Fig. 7). Under these assumptions, the true velocity of any particle can be determined, and this approach was decided upon for late-time frames.

Hypervelocity Range

This investigation was conducted using the Air Force Materials Laboratory (AFML) hypervelocity ballistic range. The portion of the range used in this experiment consisted of the light-gas gun (Fig. 8) and associated instrumentation. The light-gas gun is a device for accelerating small projectiles of various materials to very high velocities (6-7 km/sec). The projectiles proceed down the gun barrel and impact targets of various materials and configurations mounted in the target tank. Since the gun barrel is evacuated to low pressures (25.2 torr), the projectile experiences very little deceleration.

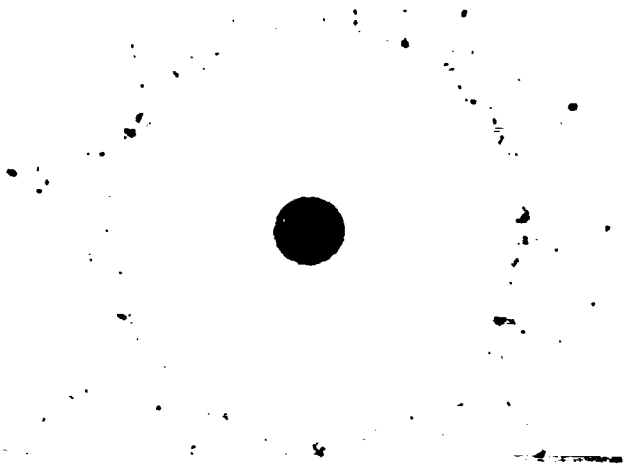

Fig. 6. Ejecta Impact Pattern on Paper Placed on Face of Vertical X-ray Cassette Located 21.6 cm Uprange From Target

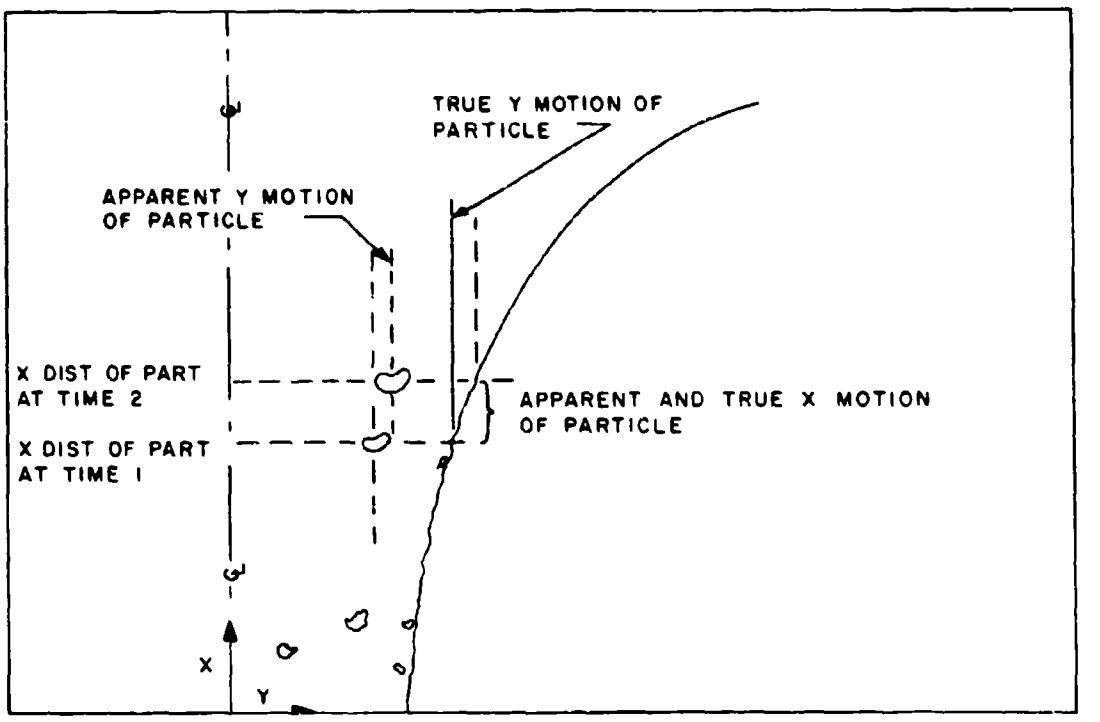

Fig. 7. Graphical Presentation of Scheme for Solution From Discrete Particle Travel

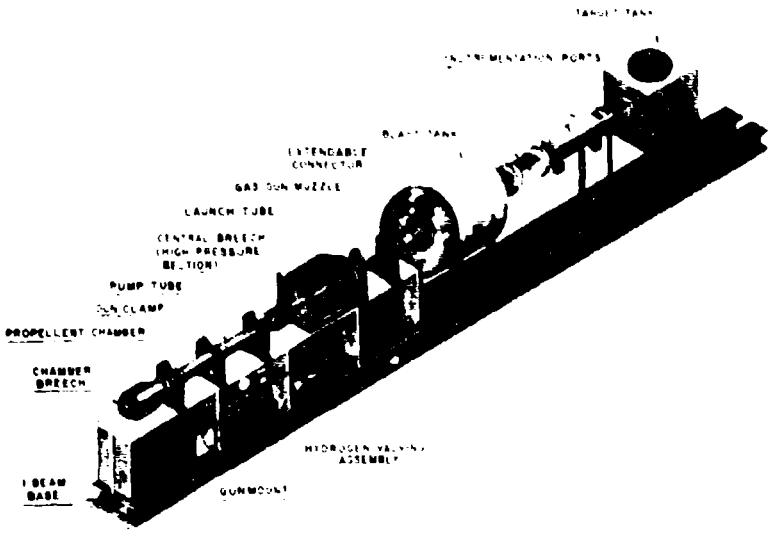

Fig. 8. Schematic of AFML Light-Gas Gun Range

The flash x-ray systems employed in the range facility consisted of three 300 kv and two 105 kv heads. When pulsed, these heads emit a very intense burst of x-ray energy of approximately 20-30 nanosecond duration. This short pulse duration produces radiographs of high-speed events with negligible motion blur. The output of x-ray energy from each head was sensed by a switch physically mounted on each head (Ref 29). The electrical pulse generated by each switch was used to fire a xenon flash tube (winker) which was photographed on the range time-recording films (to be discussed later). This permitted very accurate determination of the time of firing of each x-ray head. Inasmuch as a complete description

of the facility is available elsewhere (Ref 28), only those modifications of and additions to range facilities and apparatus necessary for this experiment will be discussed in detail. Radiography and optical photography layouts are discussed in Chapters III and IV.

Time Determination

Elapsed times between electronic events occurring in the course of hypervelocity impact experiments conducted on the AFML range are recorded on and determined from reel-type streak camera (Fastax)* films. The recording of the time of non-electronic events such as impact is more difficult. This problem was solved by aiming a photomultiplier (PM) tube at the target face. The impact flash caused the PM to put out a low-voltage signal which, after amplification, was similarly used to fire xenon winkers.

With this basic system, the relative time between any two events can be determined to an accuracy of 60 nanoseconds (Ref 28:19). At the outset of the experiment this basic Fastax winker system was used to determine the times of x-ray firings, the output of each x-ray head switch being recorded by a separate winker. Under the basic system, these times could be related to the time of impact only by employing projectile velocity. In an effort to decrease the possible error in time of impact resulting from either errors in velocity determination or deceleration of the projectile after such determination, an

* Wollensak 16 mm "Fastax" oscillographic camera.

additional rotating-drum type streak g camera (Dynafax)* was employed to record the actual impact flash as well as such events as x-ray firings and, later, PM tube output and camera shutter signals. The Dynafax is capable of attaining about three times the film speed of the Fastax camera. By essentially "paralleling" the two camera records, it was possible to determine relative time between events with a maximum error of about 40 nanoseconds.

The procedure employed to determine the times of image converter camera shutter operation is typical of system operation and will be discussed in some detail. Basic time information was derived from the Fastax system. Timing marks (placed on the Fastax film through the operation of a light-chopper driven by a high speed, precisely synchronized electric motor) permitted accurate determination of Fastax film speed. The Fastax film distances between winkers marking PM tube output (T_o) and the winkers actuated by each camera shutter signal were then converted to times. On the Dynafax film, distances were determined between the T_o winkers and the winkers marking camera shutter operation. (Two winkers were utilized, one on each side of the film track to correct for possible slit misalignment). Division of each distance on the Dynafax film by its appropriate time from the Fastax calculations furnished three values for Dynafax film speed. The average of the three values was then adopted as the

* Beckman & Whitley "Dynafax" Model 3193 camera.

true Dynafax film speed. The distances on the Dynafax film between the impact flash and the camera shutter-signal winkers were then divided by Dynafax film speed to yield the times from impact to each camera shutter operation. Raw data and computations for shot #2464 appear in Appendix B. A photograph of the Dynafax camera and associated winker system appears as Fig. 9.

Accurate determination of effective interframe times in the B&W 300 camera is extremely difficult. Between any two frames, errors of as much as 10% of the nominal (or average) interframe time seem probable. Over an interval of many frames, the resultant error would probably be less because errors would tend to cancel out. Since the exposure time is roughly 25% of the interframe time, the precision

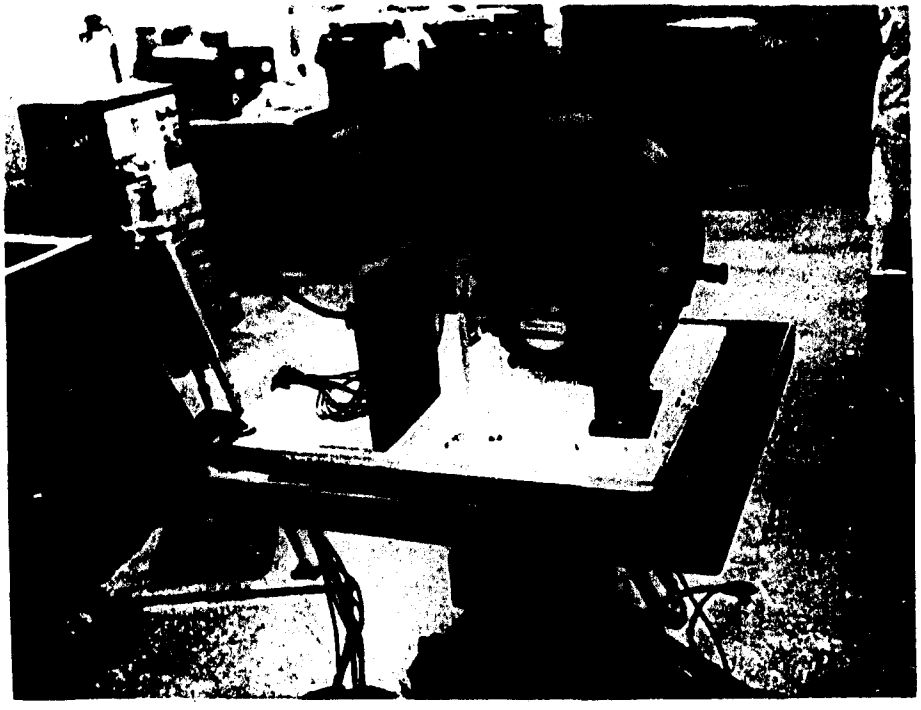

Fig. 9. Photograph of Dynafax Camera and Associated Winker System

of the data acquired is limited to about .2 to .4 mm in object plane spatial resolution and .25 to .50 microseconds in time resolution.

Switches

Throughout the course of the experiments, various types of switches were employed to initiate the timing cycle. The two types employed with the B&W 300 camera were mylar-foil switches, closed by projectile perforation (Ref 2:93) and ion-probe switches, closed by projectile passage between the probes (Ref 28:18). Fig. 10 presents a schematic signal-flow diagram of the instrumentation discussed thus far. The output signal of the initiating switch (ion-probe or mylar-foil) was directed to actuate the light source, either directly or through a time delay generator depending upon the distance of the switch from the target face. The initiating signal simultaneously actuated three separate time delay generators. The output of each generator then fired appropriate x-rays. The last time delay generator simultaneously activated the Kerr cell, thereby shutting off the source of light for the B&W 300 camera. The initiation or T_0 signal, the output of the three x-ray time delay generators, and the firing signal from each x-ray head switch were recorded on the Fastax film record through the activation of xenon winkers. The T_0 signal and the outputs of the first and last time delay generators were likewise recorded on the Dynafax film record, along with the impact flash.

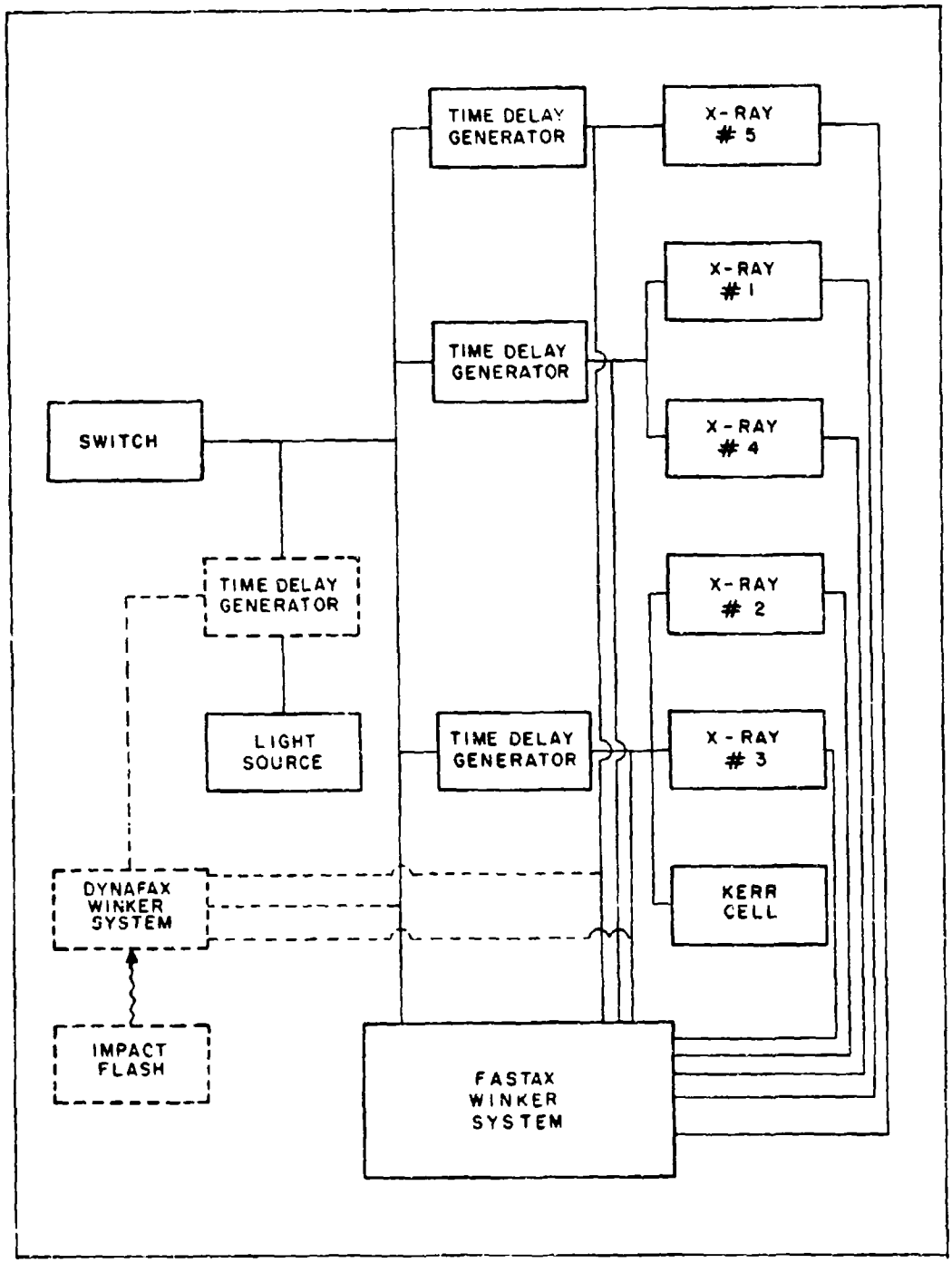

Fig. 10. Signal-Flow Diagram for Experiments Employing X-rays and Framing Camera

The mylar-foil and ion-probe initiating switches employed in conjunction with the B&W 300 camera did not prove entirely satisfactory for the purposes of this experiment. The mylar-foil switch invariably functions correctly; but once closed, it frequently gives repeated output signals as the triggering networks repeatedly discharge through the short-circuited switch. Also, debris resulting from penetration of the switch proceeds downrange with the projectile and interferes with the desired optical record of the ejecta cloud formation. While the ion-probe switch is free from the problems of debris and repeated output signals, it is a much less positive device. For these reasons, it was decided to employ a photomultiplier (PM) tube to sense the impact flash. Because the output of the PM tube is only a few volts, it was necessary to amplify the output to a level sufficient to activate the time delay and thyratron networks. A signal flow diagram of the resulting system appears in Fig. 11. The output of the signal amplifier was recorded on the Fastax and Dynafax film records along with the impact flash (Dynafax only) and image converter camera shutter operations. Recording of the impact flash was necessary since measurements indicated that there was a delay of about 1 microsecond between PM tube activation and the resulting winker firing.

Target Tank Pressure

Because aerodynamic drag is required to separate from the projectile the plastic sabots currently in use at the AFML facility, it

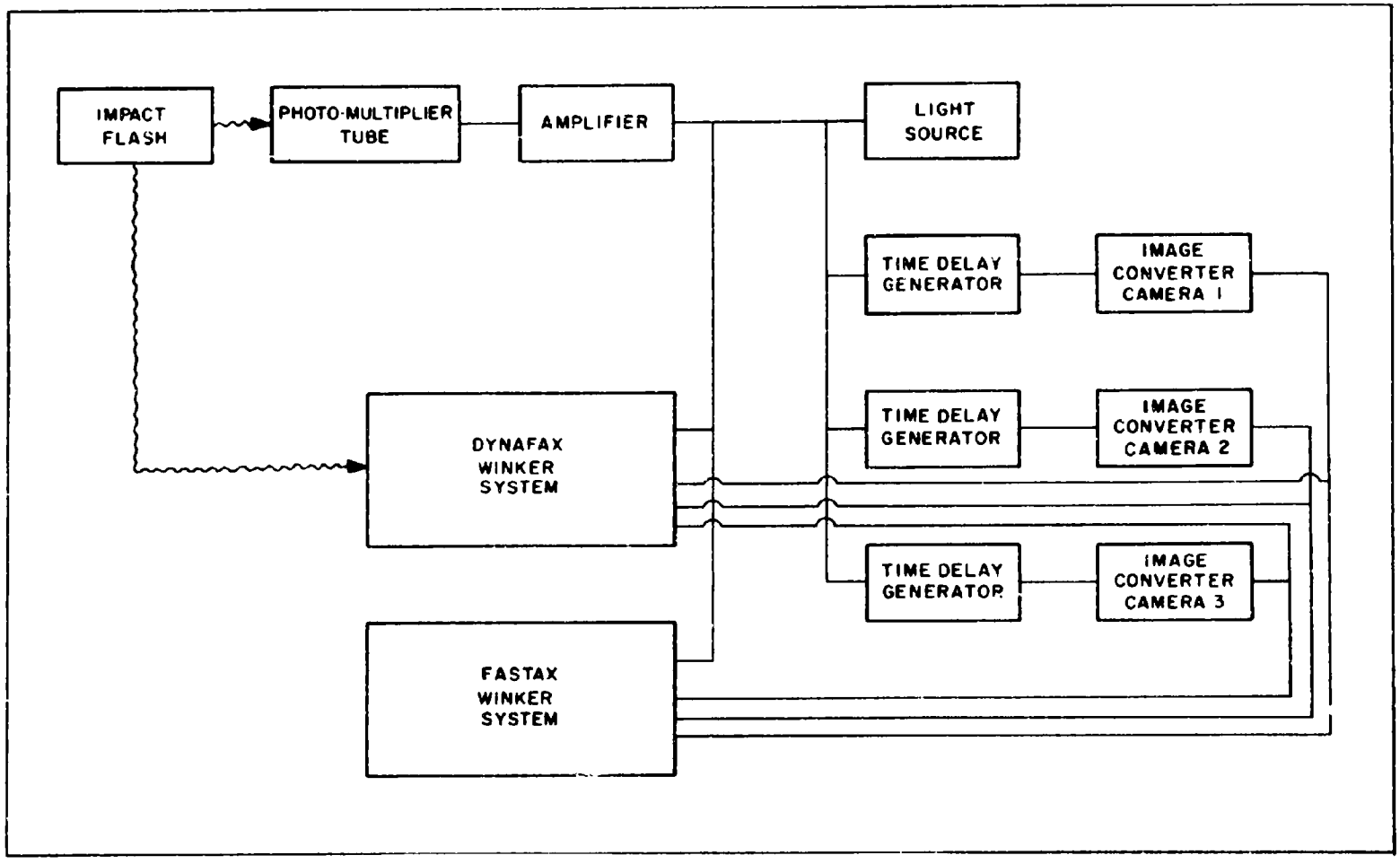

Fig. 11. Signal-Flow Diagram for Experiments Employing Image Converter Cameras

was necessary to maintain range pressure no lower than 25.2 torr to ensure satisfactory separation. Early cloud measurements indicated that even this slight an atmosphere was sufficient to decelerate appreciably the extremely small particles constituting the early ejecta. Therefore for the image converter camera experiments, the target tank was isolated from the remainder of the range by a 6.5 μ mylar diaphragm. The pressure in the isolated target tank was then reduced to a range of .09-.175 torr by means of a supplementary vacuum pump.

Measurement Techniques

All film records, both optical and x-ray, were analyzed on a specially built microviewer (Fig. 12). (The radiographs were also analyzed on a high-resolution microdensitometer, but this method proved unsatisfactory because of insufficient film distance between bolts to establish an accurate baseline.) Experience has indicated that personnel familiar with the microviewer can determine, on high-quality negatives, the coordinates of a sharply defined point (such as the intersection of grid lines) to an accuracy of $\pm$.01 mm (.0005"). For less clearly defined points, the accuracy is naturally reduced. For the rather fuzzy outer extremities of an ejecta cloud curve, crater limits on a radiograph, or the determination of the position of the center of mass of a discrete particle, an error five times the .01 limit seems appropriate.

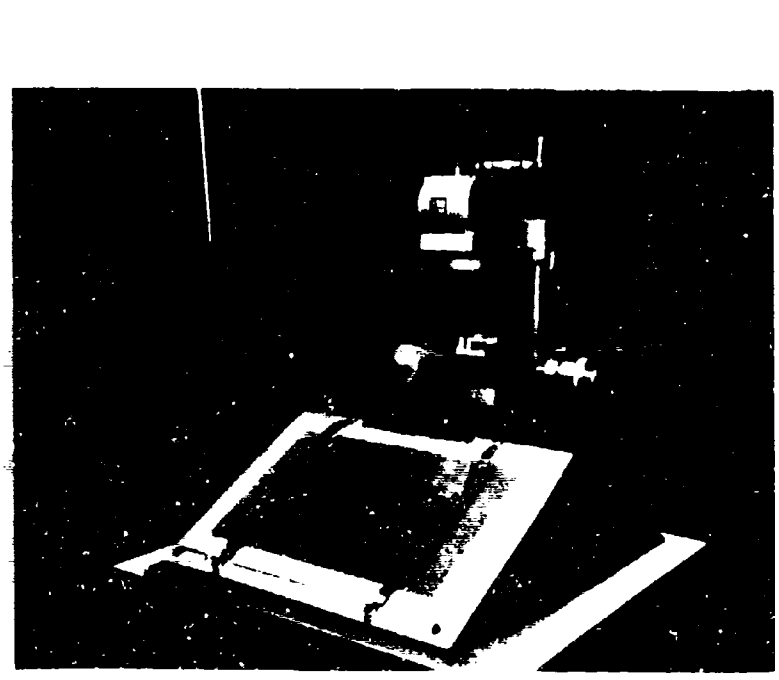

Fig. 12. Photograph of Microviewer Used for Analyzing Optical and X-ray Films

Actual crater depth and diameter measurements were obtained using a depth gage in conjunction with the calibrated-travel table of the microviewer (Fig. 13). The accuracy of measurement of both depth and diameter was on the order of ±.05 mm. However, because the craters are not perfectly symmetrical, the values determined for crater diameter depend to some extent on the axis of measurement. A review of the variation in measurements (Appendix B) indicates that the determined values are probably accurate to about ±0.3 mm. The method of measurement is shown in Fig. 14. Maximum depth of the crater (P_{CF}) was measured from the undisturbed target face. Crater diameter (D_{CF}) was established as the mean diameter

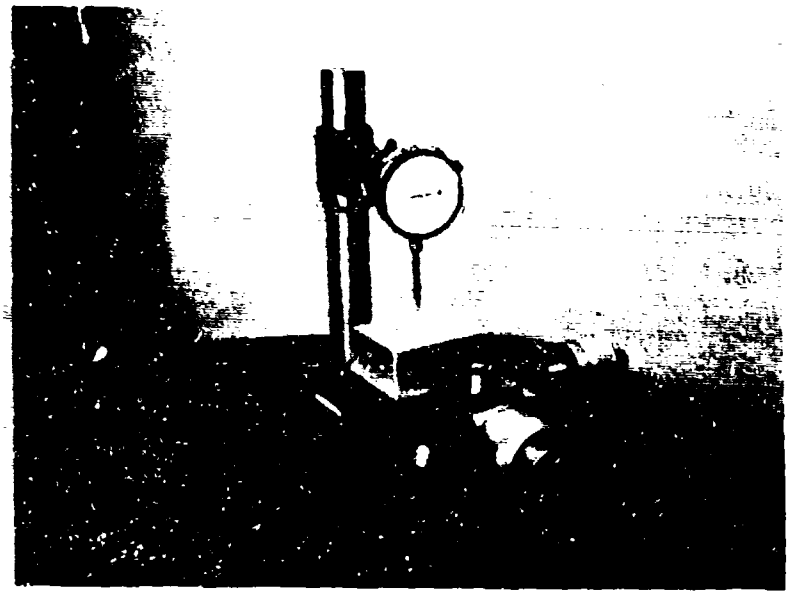

Fig. 13. Photograph of Equipment Used for Measuring Crater Depths and Diameters

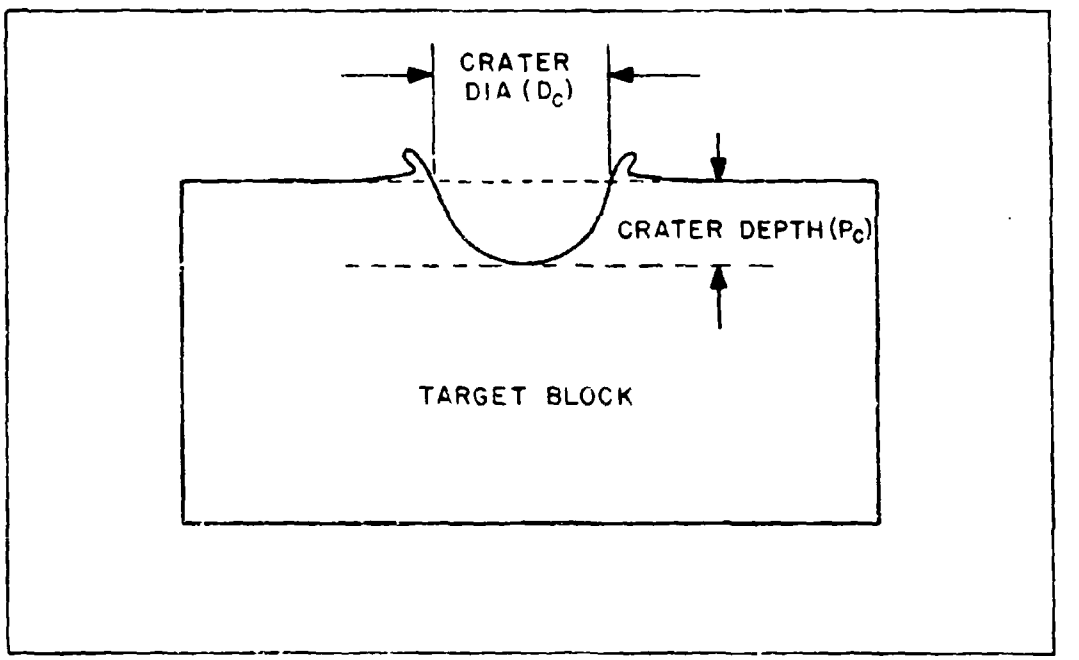

Fig. 14. Diagram of Crater Measurement Technique

represented by the intersection of the elevation of the undisturbed target face with the wall of the crater.

Projectiles and Targets

All experiments were conducted using 3.2 mm spheres of 2017 aluminum as projectiles. All targets were cut from a single ingot of 1100-0 aluminum. The ingot was specially cast and an attempt made to provide grains of uniform size. Subsequent metallurgical and tensile tests showed that all significant properties were homogeneous with respect to both position and orientation. The ingot possessed a uniform Brinell hardness value of 24 (Ref 25:32). Target dimensions (in cm) were as follows:

Shot No.	Length	Height	Depth
2384	8.9	3.6	2.4
2385	8.9	4.3	2.4
2386	8.9	5.0	2.4
2387	7.6	5.1	3.1
2463	8.3	7.7	4.0
2464	8.3	7.7	4.2

III. Crater Growth Investigation

X-ray Layout

In any hypervelocity impact on an opaque target, the ejecta cloud precludes direct optical viewing of the crater formation process. X-rays capable of penetrating the target material provide the most accurate means of following crater growth in these situations. A battery of five sequential flash x-rays were used in this investigation to generate data on crater growth as a function of time.

In order to obtain profiles of both crater diameter and depth, two 300 kv x-ray heads were positioned vertically above the target tank. They were aimed at the target through a plexiglass window in the top of the tank. The x-ray film (Kodak Royal Blue Medical) was placed in a cassette directly under the target holder in the bottom of the target tank. Experimental Dupont intensifier screens were used in the cassette to enhance the contrast obtainable in x-raying through the solid aluminum target. A schematic of the vertical x-ray layout appears in Fig. 15.

The remaining three x-ray heads (one 300 kv and two 105 kv) were positioned at the rear of the target tank. They were similarly aimed at the target through a plexiglass window in the rear of the tank. The x-ray film was placed in a cassette mounted vertically in the forward portion of the target tank. A hole was bored in the middle of the cassette to provide a means of projectile passage. Dupont

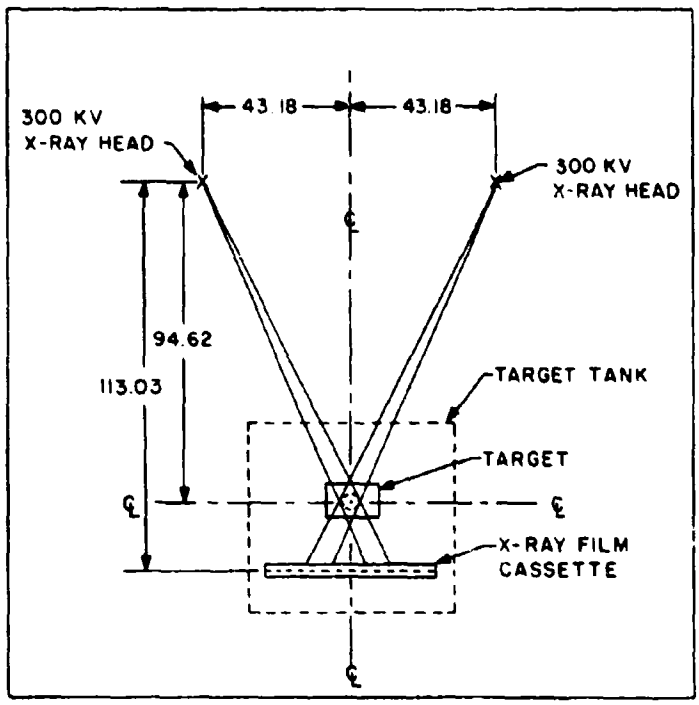

Fig. 15. Positioning of Vertical X-ray Heads
(Dimensions are in cm)

intensifier screens were also employed in this cassette to enhance contract. A schematic of the layout appears in Fig. 16.

Since x-rays can be considered neither a point nor a parallel source, determinations of true dimensions from a single radiograph are very difficult. However, characteristic dimensions of a symmetrically changing body (such as a crater) can be readily determined by using the technique of comparing the measurements on two radiographs, one taken during the event and the other after the process is complete. Of course, the geometrical relationships between x-ray head, target, and film plane must be identical for the two radiographs. The diameter and depth of the crater during the

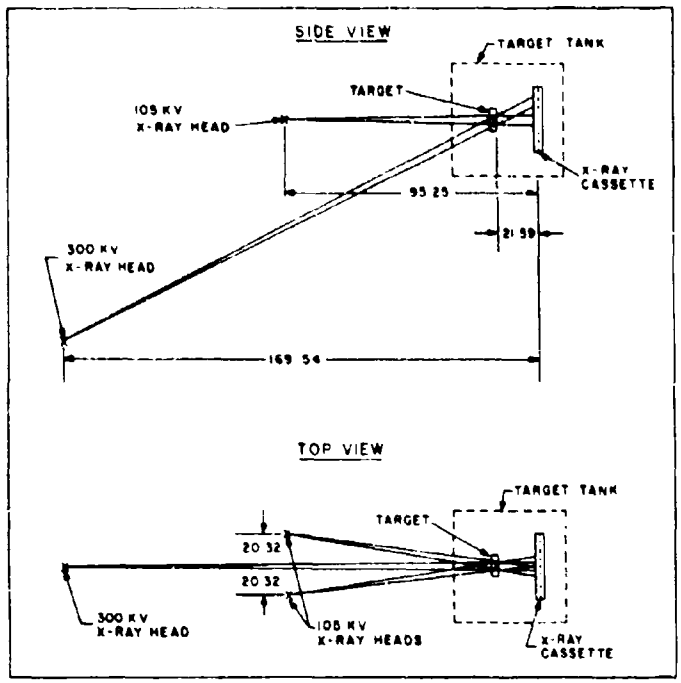

Fig. 16. Positioning of Horizontal X-ray Heads (Dimensions are in cm)

event are then readily obtained by applying the ratio of measured dimensions on the two radiographs to the final crater parameter as determined by actual measurement of the cratered target.

In order to ensure that the geometrical relationships could be held constant, a combined target- and x-ray cassette-holder was constructed (Fig. 17). The target was supported on a plexiglass ledge provided with a lip to hold the target securely against the vertical fiberboard target-holder. The plexiglass ledge (with target resting on it) was supported on bolts extending from the fiberboard target-holder. Wing nuts were affixed to the bolts to facilitate target mounting and removal and to allow the target to be held securely against the holder.

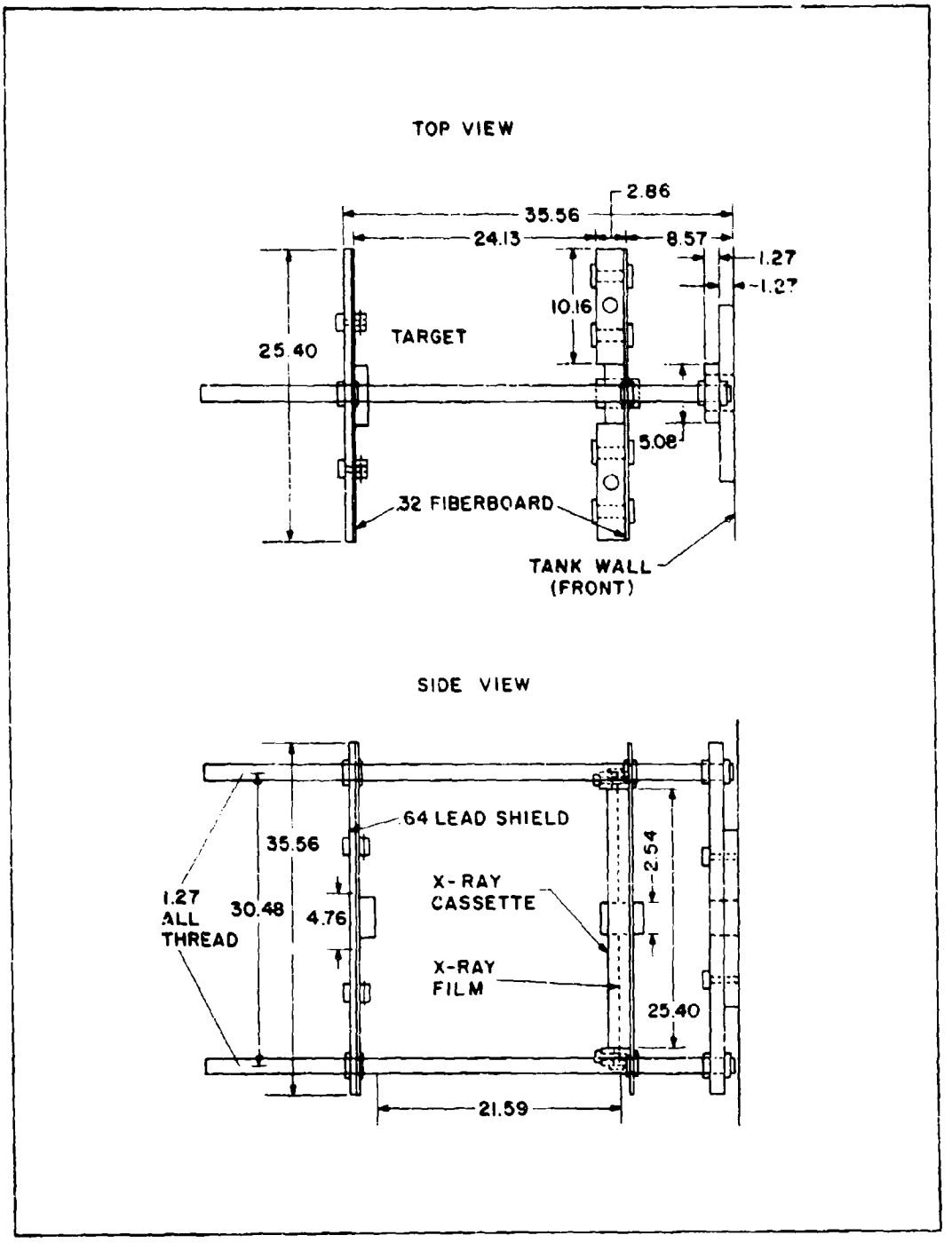

Fig. 17. Schematic of Target and Vertical X-ray Cassette Holders (Dimensions are in cm)

To prevent multiple-exposure of the x-ray film resulting from the firing of the three separate horizontal heads, a 6.4 mm lead shield was placed behind and bolted to the target-holder. A 4.76 cm hole was then bored through both lead shield and fiberboard target-holder directly behind the target position. Thus maximum x-ray energy from each head was allowed to pass through the target and strike different locations on the film in the vertical cassette.

In order to ensure that the x-ray cassette could be relocated for the radiograph to be taken after the shot in the same position it had occupied for the radiograph taken during crater growth, an x-ray cassette holder was similarly constructed of fiberboard. Plexiglass ledges were bolted to the fiberboard at the top and bottom, spaced so that the cassette fit snugly between. Thumb screws were added to clamp the cassette in position on the ledges. Through the 2.54 cm hole bored in both cassette and fiberboard was passed a short length of pipe. This assured correct horizontal positioning and helped to make the x-ray cassette light-tight around the hole. (The area where the pipe emerged from the cassette was repacked with Duxseal* each time the cassette was loaded with film.) Finally, both target-holder and x-ray cassette holder were rigidly fixed at the desired spacing by parallel sections of 1.27 cm diameter threaded rod at the top and bottom. The entire unit was affixed to the target tank by the same

---

* Brand name for a putty-like sealing and caulking compound used in the electrical industry.

threaded rod. A photograph of the completed unit appears in Fig. 18. The horizontal x-ray cassette (containing film to be exposed by the two vertically-mounted 300 kv heads) was supported in the bottom of the target tank on lead bricks and wedged securely under the target holder.

Radiographic Results

The radiographs from shot #2386 appear as Figs. 19 and 20. (Radiographs of shots #2384, 2385, and 2387 appear as Figs. 37 through 42 in Appendix B.) To the naked eye, the contrast is generally adequate to determine crater limits. However, the magnification resulting from viewing the negatives projected through the 10X head

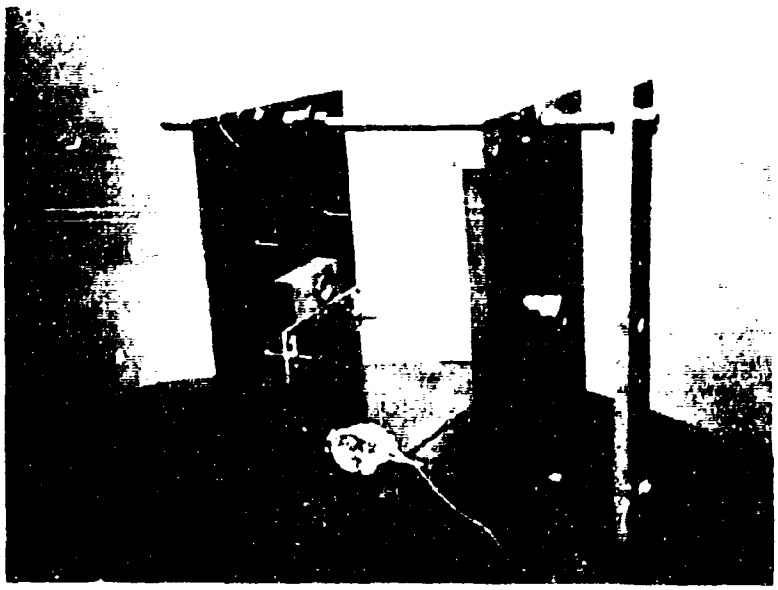

Fig. 18. Photograph of Target and Vertical X-ray Cassette Holders

During Shot

After Shot

13.48 μ sec

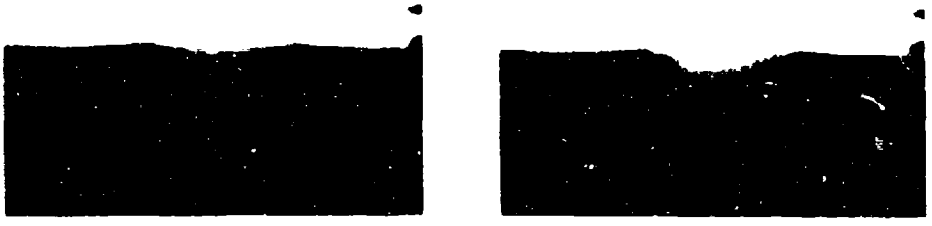

15.66 μ sec

Fig. 19. Radiographs of Crater Profile During and After Shot #2386 (Vertical X-ray Setup)

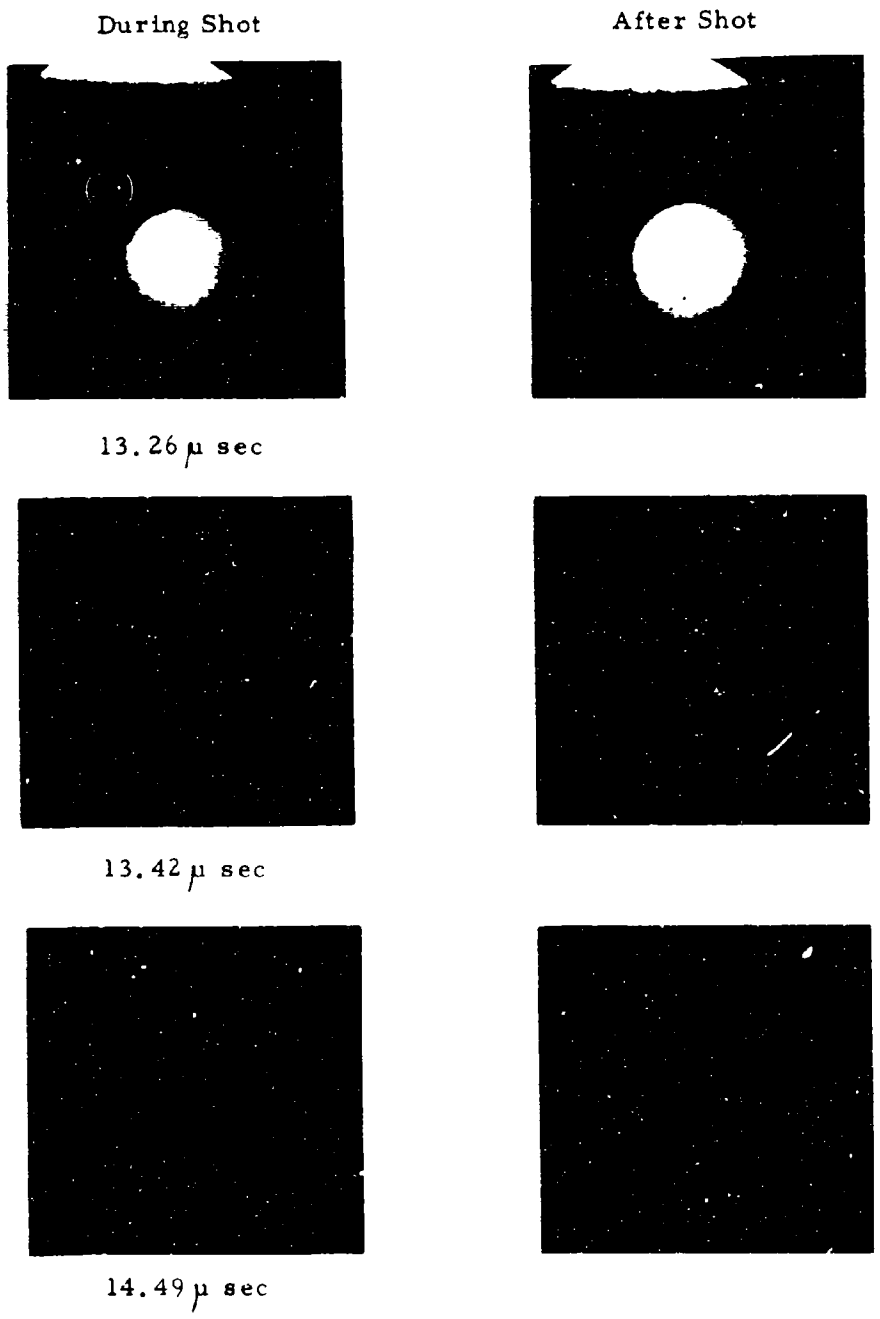

Fig. 20. Radiographs of Crater Diameter During and After Shot #2386 (Horizontal X-ray Setup)

of the microviewer greatly diminished the contrast. In order to provide a guide to the location of the crater limits, light pin-pricks were made along the crater limits. When placed on the microviewer, the pin-pricks made it possible to determine crater limits. On the profile-view pictures, crater diameter was measured along the line of the undistorted target face; maximum depth was similarly measured from this line. The angle between a tangent to the crater wall at the point or original target surface and the target face was determined for each profile view. The angle remained virtually constant (Fig. 21). On the radiographs taken from behind the target, the maximum width across the crater image on a horizontal line was measued. Identical procedures were used on both the radiographs taken during and those taken after the shot.

Film measurements of crater depth and diameter appear in Table II. From the film measurements, the ratios of crater parameters during and after the shot were computed. The resultant time-history of crater growth is presented graphically in Figs. 22 and 23.

Since the growth of both crater diameter and depth as determined in this study appeared to follow an exponential growth law, a curve of the form $1-e^{-kt}$, where t is measured in microseconds, was fit to the data. Best-fits were obtained for values of k = .220 in the case of diameter growth (standard deviation = 4.9% of final crater diameter) and k = .214 in the case of depth growth (standard deviation = 2.83% of final crater depth). In the latter case, using the value of

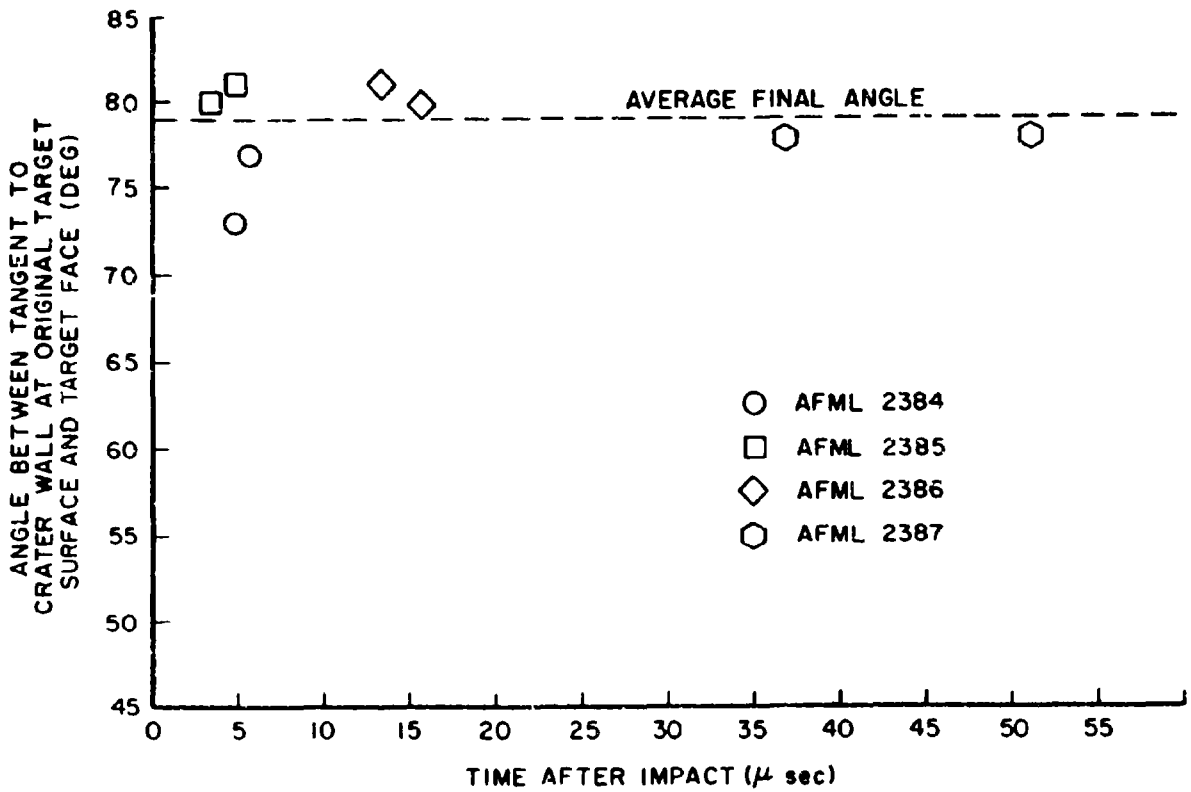

Fig. 21. Angle Between Tangent to Crater Wall at Original Target Surface and Target Face

TABLE II

X-ray Film Measurements of Crater Diameter and Depth

Shot No.	x-ray No.	During Shot		After Shot		Ratios		Time After Impact (μSEC)
		Diameter (D_{CD})(cm)	Depth (P_{CD})(cm)	Diameter (D_{CF})(cm)	Depth (P_{CF})(cm)	Diameter (D_{CD}/D_{CF})	Depth (P_{CD}/P_{CF})	
2384	1	1.5672	-	2.3906	-	.656	-	4.39
	2	1.5344	-	2.3266	-	.659	-	4.44 ± .50
	3	.6807*	.6835	.9517*	1.0310	.715	.663	5.28
	4	.7688*	.7064	1.0736*	1.0071	.716	.701	4.99
	5	1.1496	-	1.8080	-	.636	-	3.38
2385	1	1.0457	-	2.1854	-	.478	-	2.99
	2	1.3315	-	1.9251	-	.692	-	4.10
	3	1.1824	.6672	2.0002	1.0371	.591	.643	4.78
	4	1.0262	.5131	2.0668	1.0990	.496	.467	3.44
	5	.8844	-	1.9197	-	.461	-	3.21
2386	1	1.9032	-	2.0564	-	.926	-	13.42
	2	2.0536	-	2.1466	-	.957	-	14.49
	3	2.0310	1.0338	2.0851	1.0658	.974	.970	15.66
	4	1.9619	1.0198	2.0033	1.0549	.979	.967	13.48
	5	1.8306	-	1.8672	-	.980	-	13.26
2387	3**	2.0386	1.0462	2.0594	1.0749	.990	.973	51.23 ± .17
	4	1.9502	1.0086	2.0312	1.0102	.960	.998	37.00 ± 1.00
	5	1.8120	-	1.8245	-	.993	-	22.97 ± .20

* Radius measurements; portion of crater obscured by bolt.

** X-rays 1 and 2 of Shot #2387 were unreadable because of a light leak.

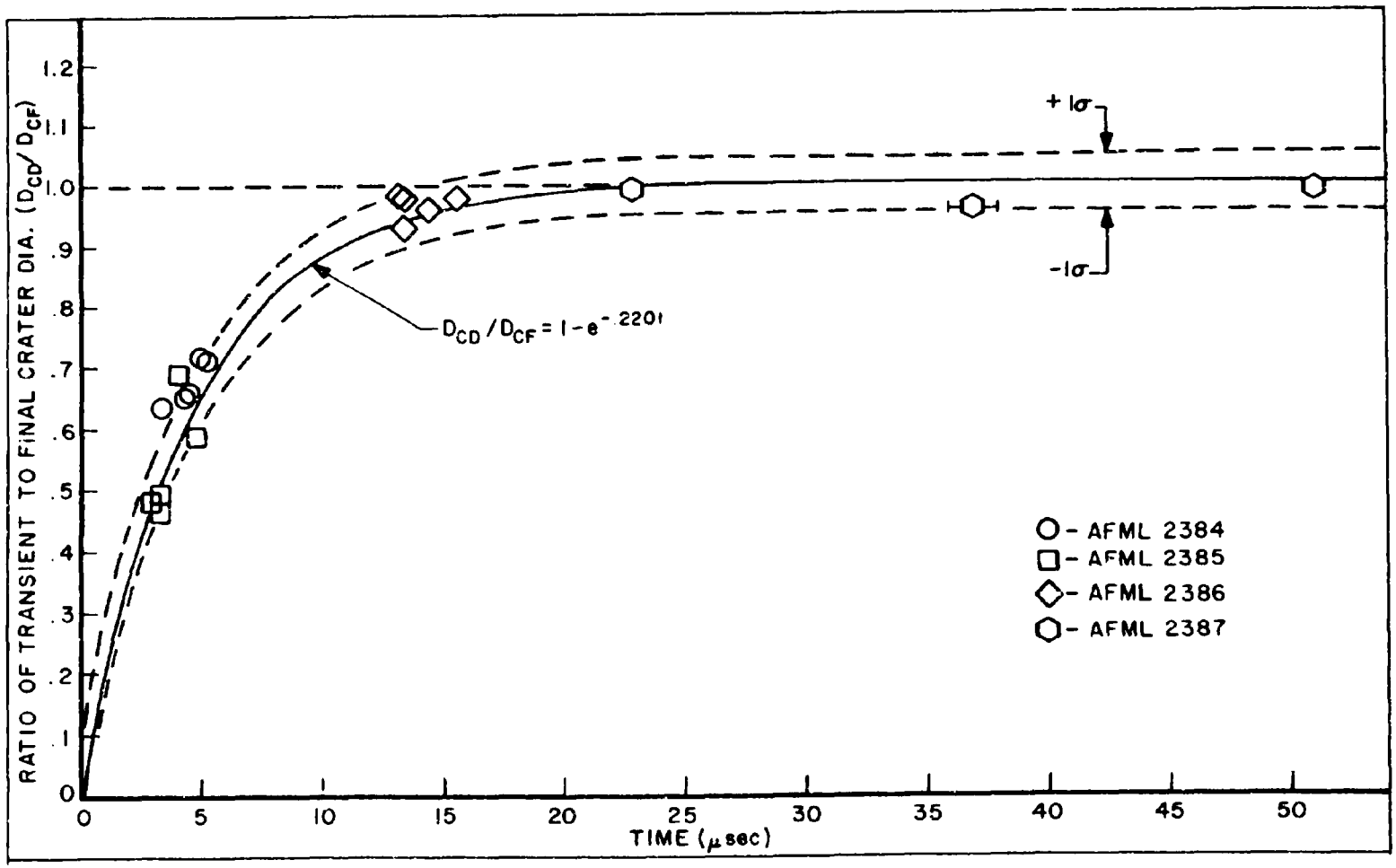

Fig. 22. Plot of Crater Diameter Growth

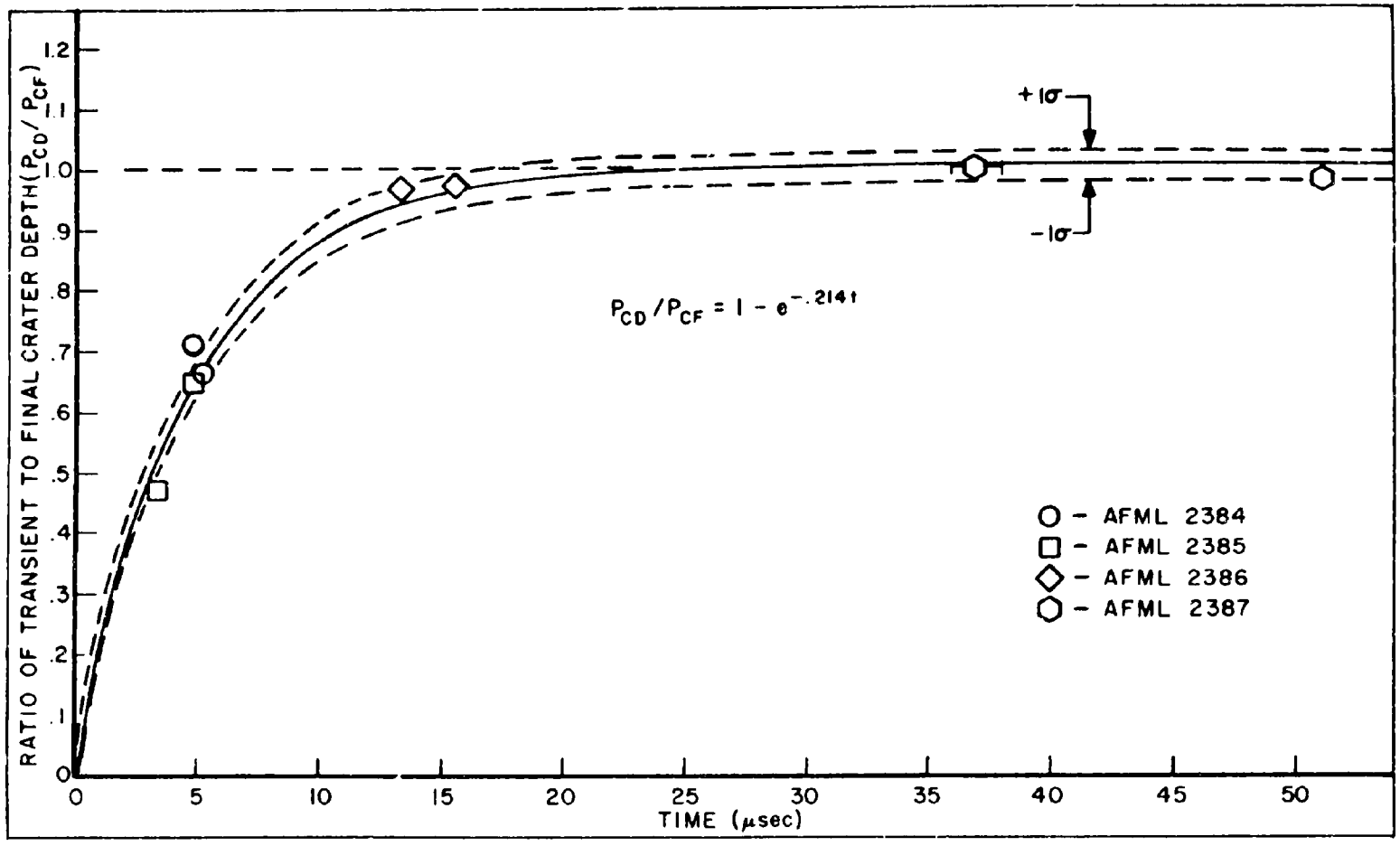

Fig. 23. Plot of Crater Depth Growth

k = .220 as determined for diameter growth provides a surprisingly good fit, with a standard deviation of only 2.96%. The best-fit curves are plotted on Figs. 22 and 23.

Measurements of Final Craters

A photograph of the six cratered targets appears as Fig. 24. Since the velocities of impact and projectile weights were controlled as carefully as possible to ensure constant impact energy, the resulting craters are very similar, as might be expected. Spallation, clearly visible on the target from shot #2384, did not result in any significant alteration of crater size or shape. Maximum crater depth, measured from the plane of the undisturbed target face, varied by only .66 mm. Two separate diameter measurements along perpendicular traverses were made for each crater, the diameter being measured from the intersection of the crater wall with the plane of the undisturbed target face in each case. The maximum variation in crater diameter was .7 mm. The resulting values of crater diameter and depth are presented in Table III. (Raw data and method of reduction appear in Appendix B.)

In an effort to determine the degree of reproducibility of the experiments, the crater diameters were scaled to shot #2386 as a standard according to the cube roots of impact energy. /Both Riney and Walsh concur in energy scaling, the latter with a slight reservation (Ref 3:257-258)./ As can be seen from Table IV, the resulting

Shot #2384 Shot #2385 Shot #2386

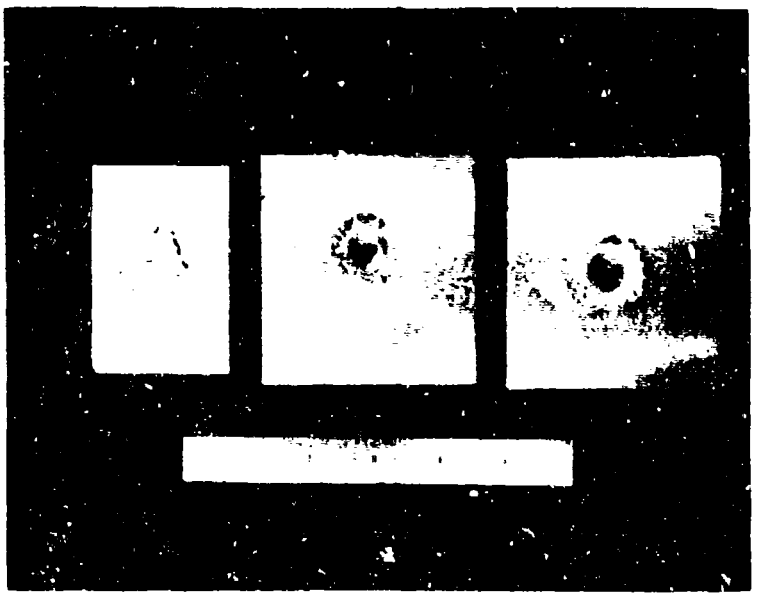

Shot #2387 Shot #2463 Shot #2464

Fig. 24. Photographs of Cratered Targets

TABLE III

Direct Measurements of Crater Diameter and Depth

Shot Number	Average Crater Diameter (cm)	Maximum Crater Depth (cm)
2384	1.65	.90
2385	1.67	.93
2386	1.64	.92
2387	1.60	.86
2463	1.53	.93
2464	1.60	.87

TABLE IV

Comparison of Crater Diameters Scaled According to the Cube Root of Impact Energy

Shot Number	Projectile Mass (milligrams)	Projectile Velocity (km/sec)	Impact Energy (kilojoules)	Impact Energy$^{1/3}$	Crater Diameter (cm)	Scaled Diameter (cm)	% Variation from STD
2384	45.78	6.900	1.089	1.029	1.65	1.67	+1.83
2385	45.80	7.052	1.139	1.044	1.67	1.67	+1.83
2386	45.89	7.034	1.135	1.043	1.64	1.64	0.00
2387	46.00	7.010*	1.130 ± .042	1.042	1.60	1.60	-2.44
2463	45.75	6.762	1.046	1.015	1.63	1.67	+1.83
2464	45.96	6.872	1.085	1.028	1.60	1.62	-1.22

* Velocity-measurement record destroyed (Fastax film broke).
Velocity estimated 7.01 ± .07 based on history of gun performance.

variations from standard are of the same order as the variations in uncorrected crater diameters. Hence, it is felt that the variations represent normal measurement scatter, and that the craters are virtually identical. It would therefore appear that the experiment is entirely reproducible.

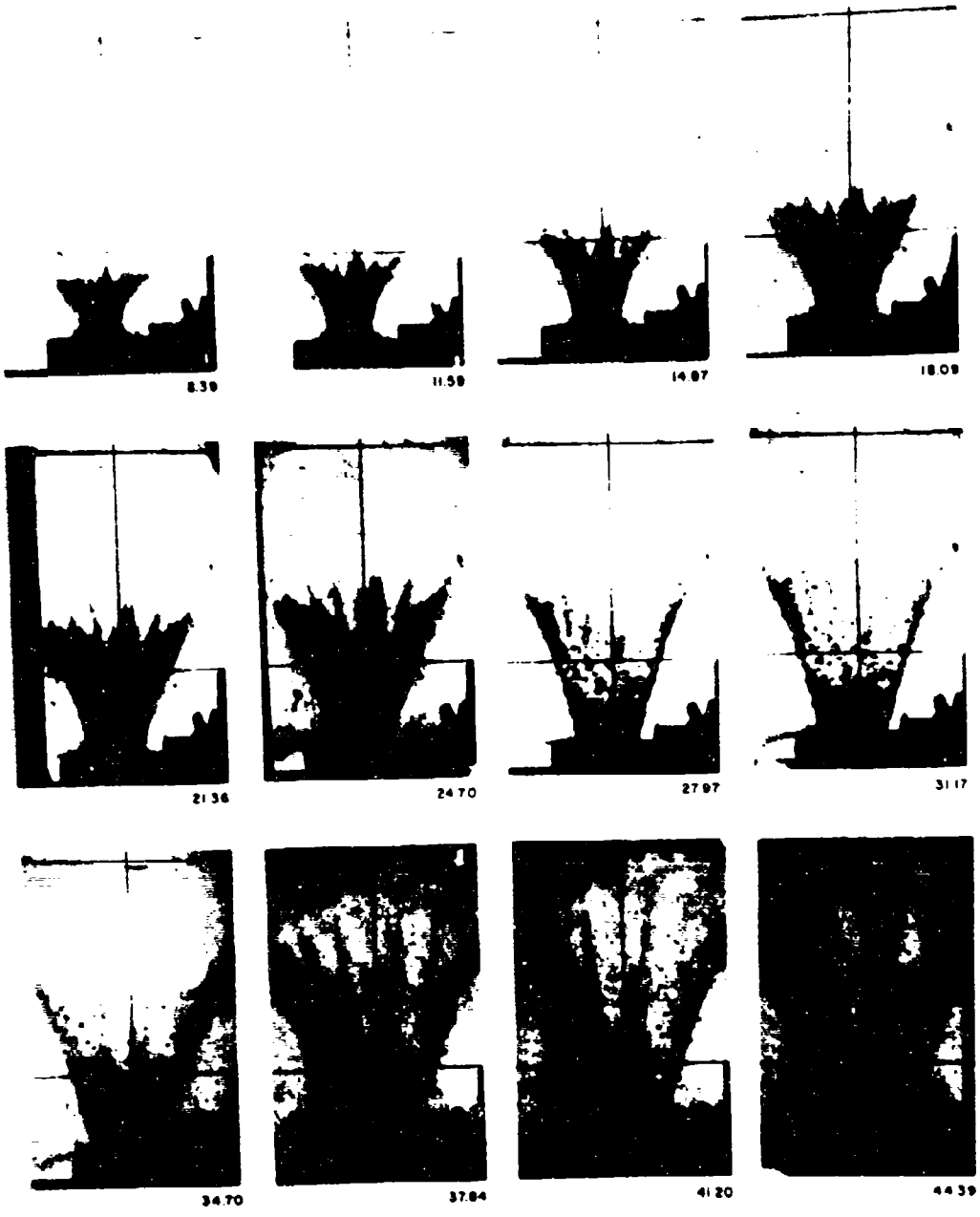

Fig. 32. Examples of Late-Time Framing Camera Photographs of Ejecta Cloud From Shot #2387 With Times From Impact (μ sec) [Magnification = 0.14 (nom)]

IV. Ejecta Cloud Investigation

Camera Layouts

Framing Camera. Because of the rapidity with which the ejecta cloud is formed, ultrahigh speed optical photography provides the best tool for observing its formation and growth. A Beckman & Whitley Model 300 framing camera was initially used to obtain optical photographs of the ejecta cloud (see Fig. 25). At the extremely high framing rates (4.5 million frames/sec) which this camera is capable of, shuttering is best accomplished by accurately controlling the synchronization and duration of the back lighting source. Since the spark light source employed had an extremely rapid rise time (on the order of one microsecond), it was necessary only to control light extinction. This was accomplished by using a Kerr cell which effectively cut the light off in less than 0.1 microseconds. A schematic of the optical layout employed with the B&W 300 camera appears in Fig. 26. An integrated schematic of both optical and x-ray layouts appears in Fig. 27.

The large ratio of frame exposure time to interframe time (1:4), low optical resolution, and inaccuracies in interframe time combined to reduce the precision of the resultant data to values unacceptable for the cloud-edge investigation. However, data from this camera proved sufficient for monitoring gross cloud dimensions and the motion of discrete ejecta particles.

IV. Ejecta Cloud Investigation

Camera Layouts

Framing Camera. Because of the rapidity with which the ejecta cloud is formed, ultrahigh speed optical photography provides the best tool for observing its formation and growth. A Beckman & Whitley Model 300 framing camera was initially used to obtain optical photographs of the ejecta cloud (see Fig. 25). At the extremely high framing rates (4.5 million frames/sec) which this camera is capable of, shuttering is best accomplished by accurately controlling the synchronization and duration of the back lighting source. Since the spark light source employed had an extremely rapid rise time (on the order of one microsecond), it was necessary only to control light extinction. This was accomplished by using a Kerr cell which effectively cut the light off in less than 0.1 microseconds. A schematic of the optical layout employed with the B&W 300 camera appears in Fig. 26. An integrated schematic of both optical and x-ray layouts appears in Fig. 27.

The large ratio of frame exposure time to interframe time (1:4), low optical resolution, and inaccuracies in interframe time combined to reduce the precision of the resultant data to values unacceptable for the cloud-edge investigation. However, data from this camera proved sufficient for monitoring gross cloud dimensions and the motion of discrete ejecta particles.

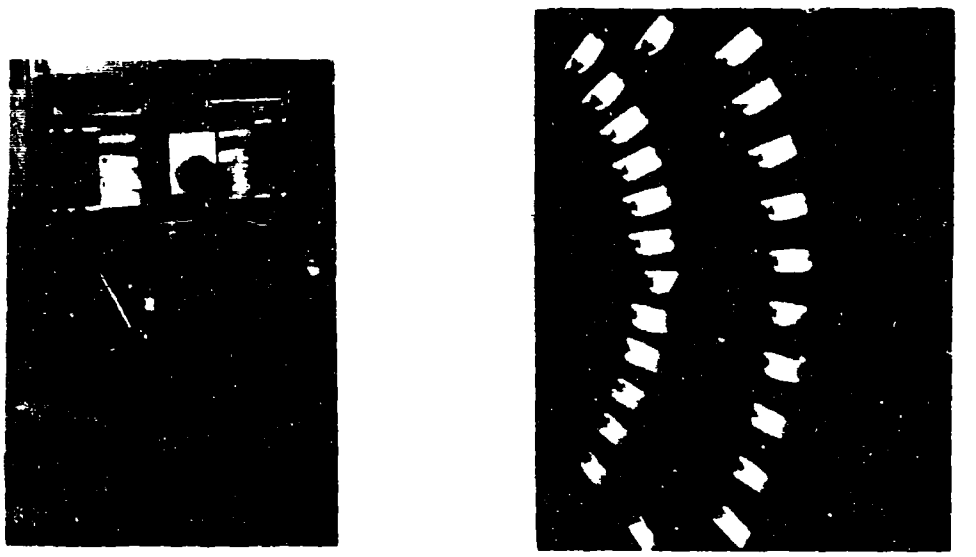

Fig. 25. Photograph of Beckman & Whitley Model 300 Framing Camera With Example of Picture Format

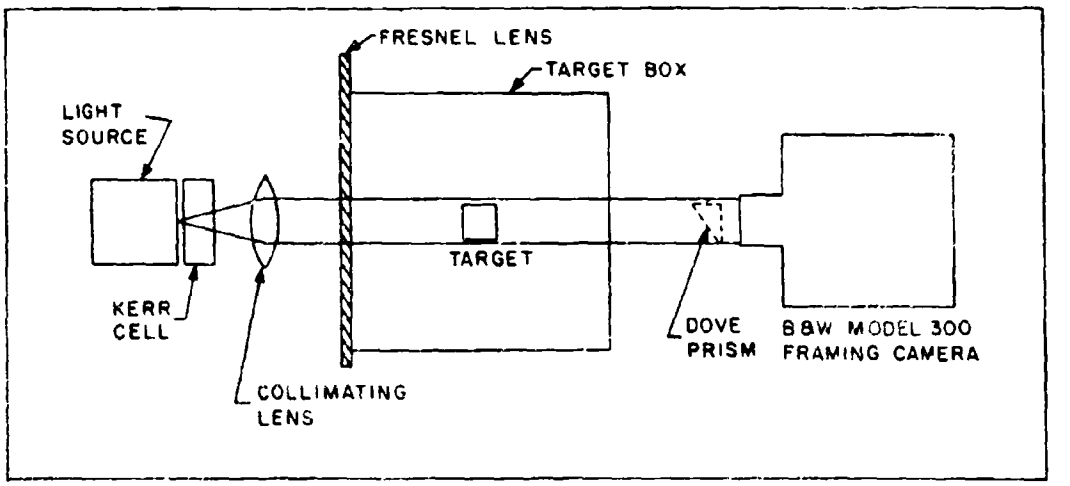

Fig. 26. Schematic of Arrangement of Beckman & Whitley Model 300 Framing Camera With Light Source and Kerr Cell

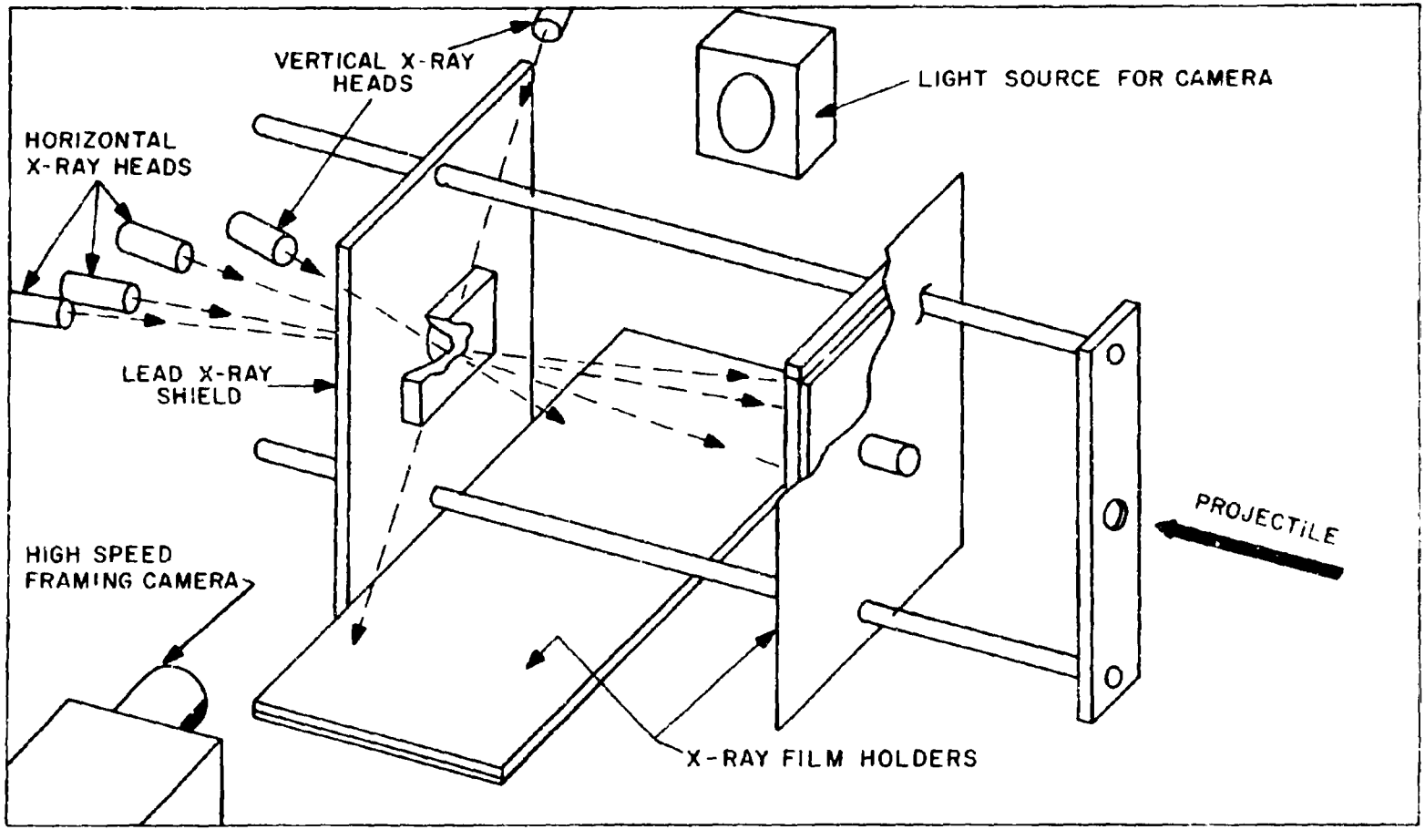

Fig. 27. Integrated Schematic of Instrumentation System Used in Experiments Employing Framing Camera and X-ray Setups

Image Converter Camera System. A three-frame image converter camera system was constructed to replace the framing camera as the principal source of cloud-edge data. The extremely short exposure times of the individual cameras (10 ns* and 1 ns**) together with variable and precisely measured interframe times provided an accurate time base for the cloud-edge experiments. The high and uniform optical resolution of the image converter cameras (15 line pairs per mm on the film plane) was sufficient to resolve all elements of the ejecta cloud of interest to this investigation.

The image converter cameras were aligned on the same optical axis through a system of mirrors as shown in Fig. 28. The topmost (1 ns) camera viewed the target through an angled mirror, silvered to transmit 10% and reflect 90% of the incident light. The second or middle camera was positioned below the first. It viewed the target by reflection off both the top mirror and a second mirror, parallel to and directly below the first, silvered to transmit 60% and reflect 40%. The bottom camera was aimed vertically upward and positioned directly beneath both mirrors. Hence it viewed the target through the lower mirror and by reflection off the upper mirror. A photograph of the cameras and mirrors in position appears as Fig. 29.

---

* Beckman & Whitley Model 500 Image Converter Camera.

** Experimental image converter camera loaned to AFML by Beckman & Whitley Corporation.

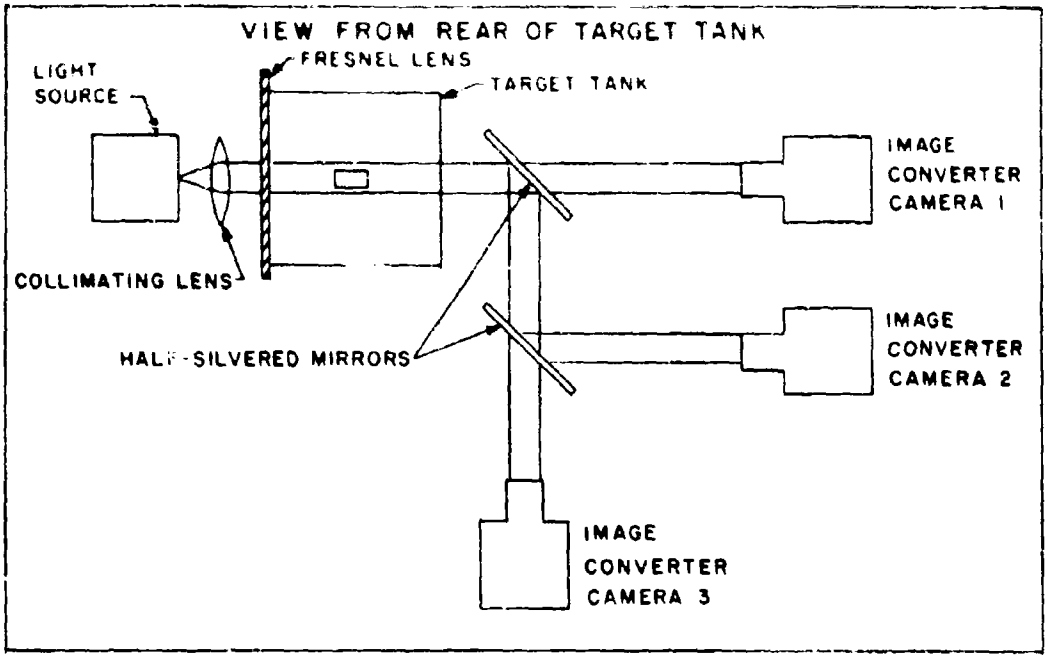

Fig. 28. Schematic of Optical Alignment of Image Converter Cameras

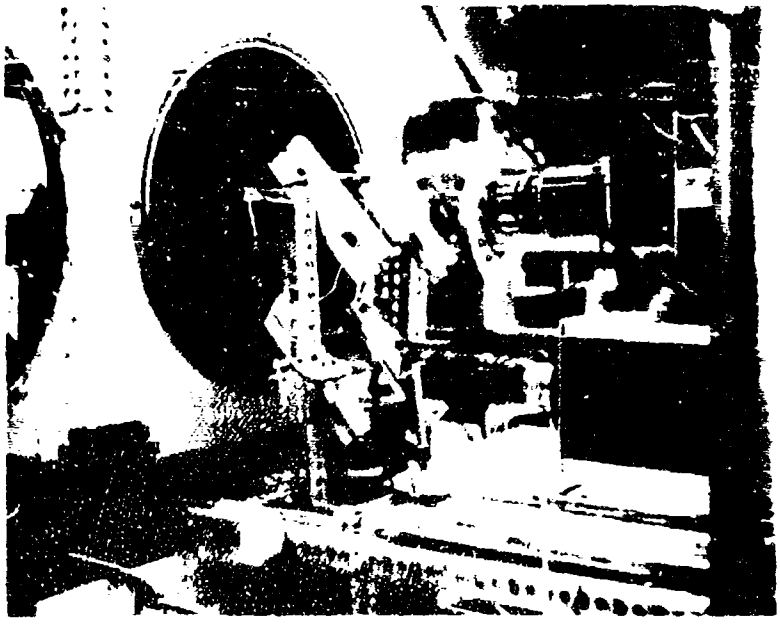

Fig. 29. Photograph of Image Converter Cameras and Mirrors in Position on the Range

Optical Results

Framing Camera Photographs. From photographs of a grid, it was determined that the B&W framing camera introduced a slight amount of optical distortion. A computer program was written to remove this distortion. In addition, the program corrected film dimensions to real space dimensions by application of a magnification factor. The magnification factor was determined independently for each frame. The film was aligned in the film reader so that the y-axis was parallel to the vertical arm of a set of crosshairs mounted permanently in the camera. Then the x- and y-coordinates of the crosshair intersection and of two points at known distances apart (in real space) were read. The program then computed the appropriate magnification factor to reduce all x-y film positions to real space coordinates. A simple orthogonal transformation was then made to shift the coordinate origin to the desired center of impact on the target face.

The ejecta cloud photographs of shot #2385 covered a time span from approximately .79 to 3.45 μ sec after impact. Representative samples of these photographs appear as Fig. 30. Upon close observations, it can be seen that the cloud is not perfectly symmetrical. Hence the two sides were treated separately. The coordinates of points along the edge of each side of the cloud in each frame were read on the microviewer and reduced to real-space coordinates by the computer program. (A length of plastic threaded rod had been screwed into the target holder ledge directly under the target; the thread ends

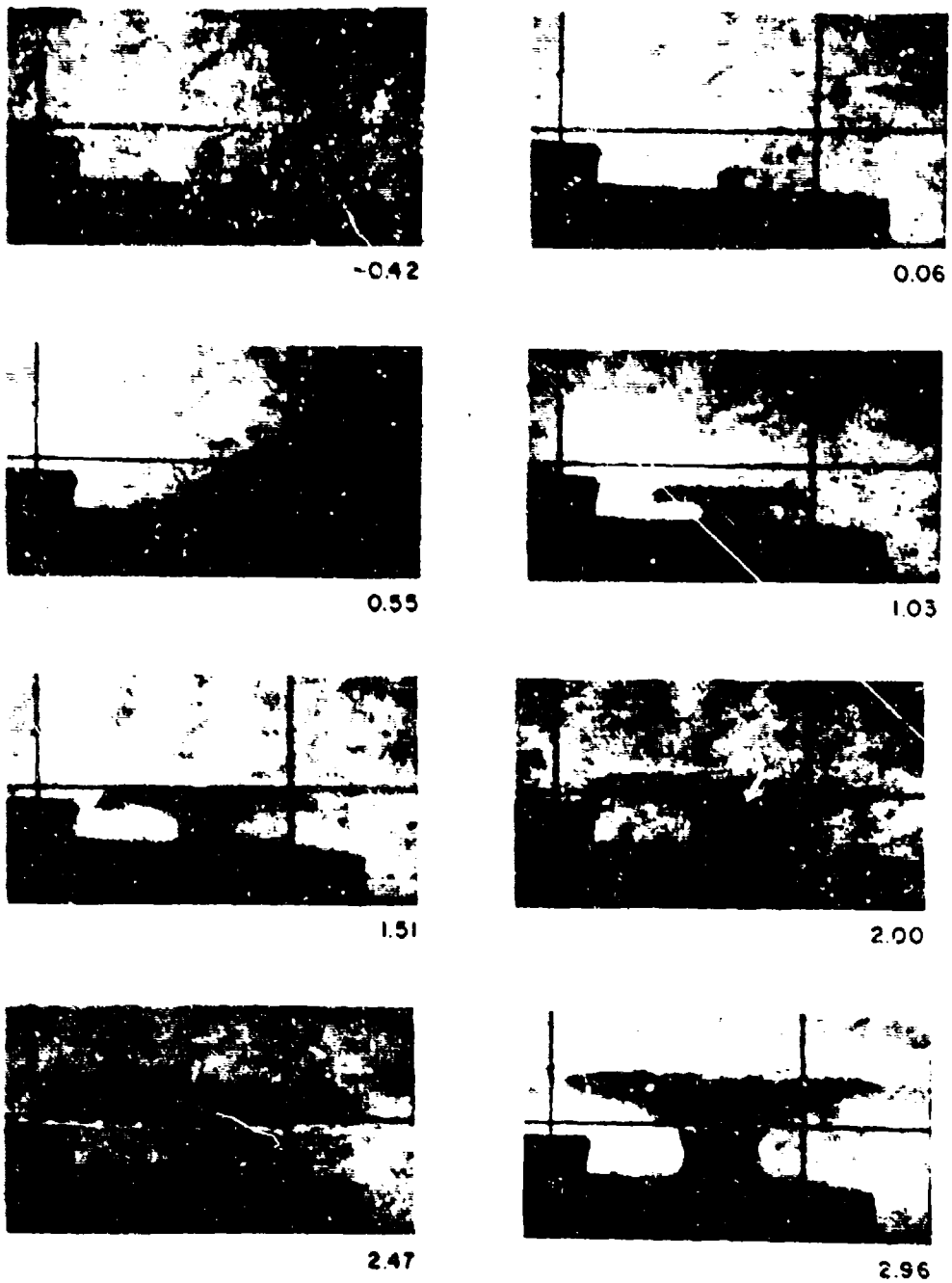

Fig. 30. Examples of Early-Time Framing Camera Photographs of Ejecta Cloud From Shot #2385 With Times From Impact (μ sec) [Magnification = 1.25 (nom)]

provided the required known-distance measurement.) Polynomials were then fit by the method of least squares to the cloud-edge coordinates. A satisfactory fit was achieved in all instances. The maximum RMS error for the top cloud edge curve was 1.47 mm; for the bottom curve, 1.83 mm.

Despite this apparent satisfactory fit of polynomials to the cloud edges, the cloud-edge program was able to find the required straight line trajectories for only a very limited number of points on these curves. A summary of the computer program output is presented in Table V.

It is quite apparent from these data that the program, with input data from shot #2385, is not giving realistic outputs. While the origin (and presumably the crater radius) is seen generally to increase with time, the entry for 230 nanoseconds reverses this trend. The apparent decrease in ejection angle with time, while unexpected, is not impossible in light of Gault's previously cited findings. However, for the ejection velocity to increase monotonically with time is a virtual impossibility. Were this the case, the entire model would be invalidated, since interparticle collisions would almost inevitably occur, and the assumption of constant velocity after ejection would no longer be tenable. Lastly, the inconsistency of the results obtained by changing only the third curve (from frame 22 to frame 20) strongly suggests that the data are not meaningful.

TABLE V

Cloud-Edge Computer Program Outputs, Shot #2385

Time of Ejection (ns)	Origin (cm)	Angle (Deg)	Velocity (km/sec)
20	.285	63.4	3.61
50	.287	62.1	3.87
80	.288	60.6	4.17
110	.291	59.0	4.50
140	.294	57.3	4.88
170	.297	55.1	5.40
220*	.253	64.5	2.11
230	.289	51.3	6.36
350*	.260	65.5	2.28

* Data obtained from frames 12, 16, and 20. All other data obtained from frames 12, 16, and 22.

A comparison of the artificial constant-velocity curve at a time after impact of 3.58 μ sec with the actual ejecta-edge curve of shot #2385 at 3.45 μ sec is presented in Fig. 31. The two cloud edges appear to be at least superficially similar in their lower portions. However, in the upper portions, the actual ejecta cloud appears to be flattening out more rapidly than the constant-velocity cloud. This suggests the possibility that the early ejecta is being decelerated by atmospheric drag. The earliest portions of the ejecta, being the least massive and the fastest would naturally undergo the greatest deceleration.

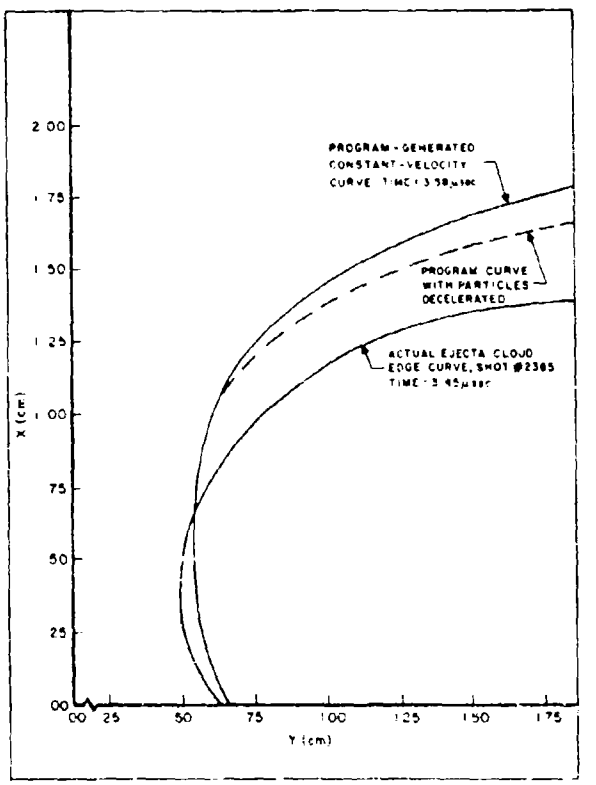

Fig. 31. Comparison of Observed Cloud Edge With Computer-Produced Constant-Velocity and Decelerating Particle Curves

To test further this possibility, a deceleration term was introduced into the cloud formation computer program. Particle velocity was reduced by a factor of e^{-kt}, where t = the time of flight of the particular particle, and k was arbitrarily selected as 3×10^{-4} divided by sequential particle number. This term, then, was based on the assumption that the earlier particles would experience more deceleration than the later, more massive particles. The curve resulting from this exercise is plotted on Fig. 31 as a dashed line. It is indistinguishable from the constant velocity computer curve in its lower region, but flattens out in its upper portion in generally the same fashion as does the actual curve.

The framing camera photographs from shot #2387 covered the entire time span from impact until ejection had virtually ceased. However, because the Kerr cell did not operate properly to cut off the light source, the frames are rewritten, i.e., in about half the frames, two separate images, one from early time and one from late time, are superimposed in the same frame. The early-time frames were deemed unusable, since cloud edges could not be accurately determined. On the late-time frames (Fig. 32), discrete particles are readily distinguishable. A number of these particles were identified by characteristic shapes, and their x-y coordinates determined in as many successive frames as was possible. The film positions were then converted to real-space positions through the computer program previously discussed. By dividing the x- and y-distance traveled by

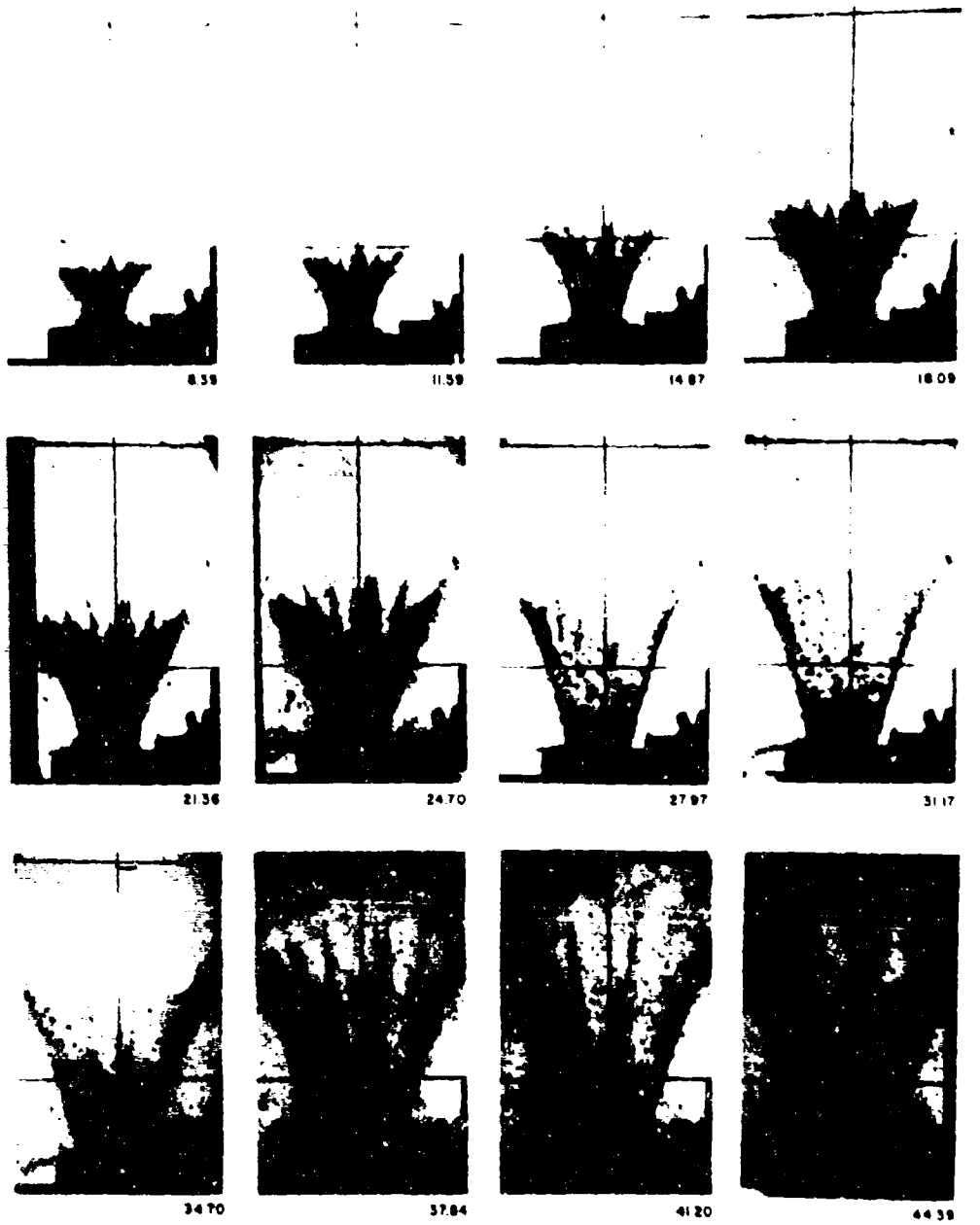

Fig. 32. Examples of Late-Time Framing Camera Photographs of Ejecta Cloud From Shot #2387 With Times From Impact (μ sec) [Magnification = 0.14 (nom)]

the time difference between frames, x- and y-components of velocity (V_x and V_y) were determined for each particle. Actual particle velocity (speed and angle) were then determined. Dividing the final x-distance of the particle by V_x yielded its time of flight, based on the assumption that its constant velocity free-flight phase had originated at the target surface. Similarly, this time-of-flight multiplied by V_y gave its y-travel, and this distance subtracted from its final y-distance yielded the assumed radial distance of particle departure from the target face.

The results of the application of these techniques to 20 particles identifiable in frames 36 and 44 of shot #2387 are presented in Table VI. (Raw data and sample calculations appear in Appendix B.) The data are listed by apparent time of ejection of the particle. The negative times are of course physically impossible. Since the time between frames of the B&W 300 camera is extremely difficult to determine accurately, it is entirely possible that all times shown could be in error by as much as .5 microseconds. Whatever time error exists would be applied equally to all particles.

These data are plotted graphically in Fig. 33. Clearly the scatter of the data for angle and velocity precludes determination of any trend. In the case of the origin (or assumed crater radius), if the data points for -1.31 and -4.38 microseconds are discarded, the remaining points do suggest increasing crater radius with time.

TABLE VI

Crater Parameters Determined from Discrete Ejecta Particle Movement, Frames 36 to 44, Shot #2387

Time of Ejection (μ sec)	Origin (cm)	Angle (Deg)	Velocity (km/sec)
-4.38	.551	53.8	.66
-1.31	.739	57.1	.67
-1.28	.203	57.1	1.07
-0.34	.320	57.5	1.26
-0.08	.381	43.8	.58
0.21	.386	57.4	1.08
0.50	.406	49.9	.64
0.87	.488	59.5	.98
0.93	.325	55.2	.94
1.30	.310	54.6	.91
1.42	.399	44.4	.57
1.50	.424	61.2	1.34
1.58	.381	56.2	.97
1.93	.381	56.0	.98
1.99	.457	60.2	1.16
2.06	.439	54.4	.90
2.30	.485	57.4	.94
2.43	.559	55.8	.79
2.84	.597	52.0	.64
2.85	.663	61.6	1.36

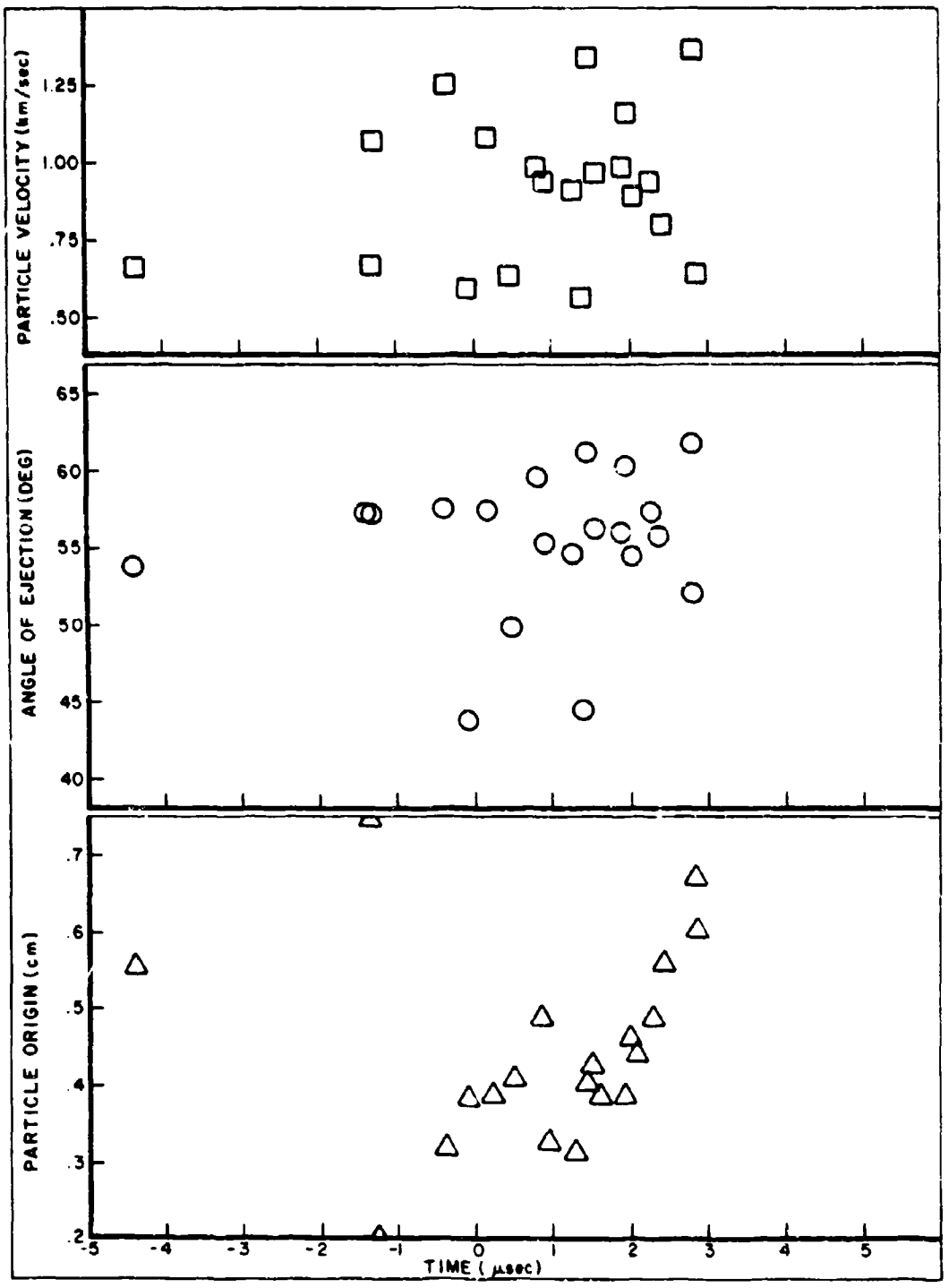

Fig. 33. Crater Parameters vs. Time Determined From Analysis of Discrete Particle Motion, Shot #2387

However, the scatter of even the remaining data is such as to warrant questioning its validity.

Image Converter Photographs. In an effort to overcome the problem of determining precisely photograph times with respect both to impact and to each other, three optically aligned image converter cameras were used to photograph the ejecta clouds of shots #2463 and #2464. For these shots target tank pressure was reduced as low as possible (.09-.175 torr). Spatial orientation was achieved by photographing a grid aligned with the projectile trajectory after each shot. Prior to target removal, the exact point of impact was determined by sighting down the gun tube with a telescope. The target was then removed from the target holder and the grid positioned so that the intersection of two specified grid lines marked the point of projectile impact. This was taken as the origin of the real-space x-y coordinate system.

Measurements of the grid photographs on the microviewer indicated that optical distortion was negligible (on the order of 1/4%). Therefore a single multiplication factor for each image converter photograph was determined from the grid photographs. The x- and y-axes from each grid photograph were transferred to the appropriate actual shot photograph by scribe marks, made while viewing the superimposed negatives on a light table. Examples of the image converter photographs appear in Fig. 34.

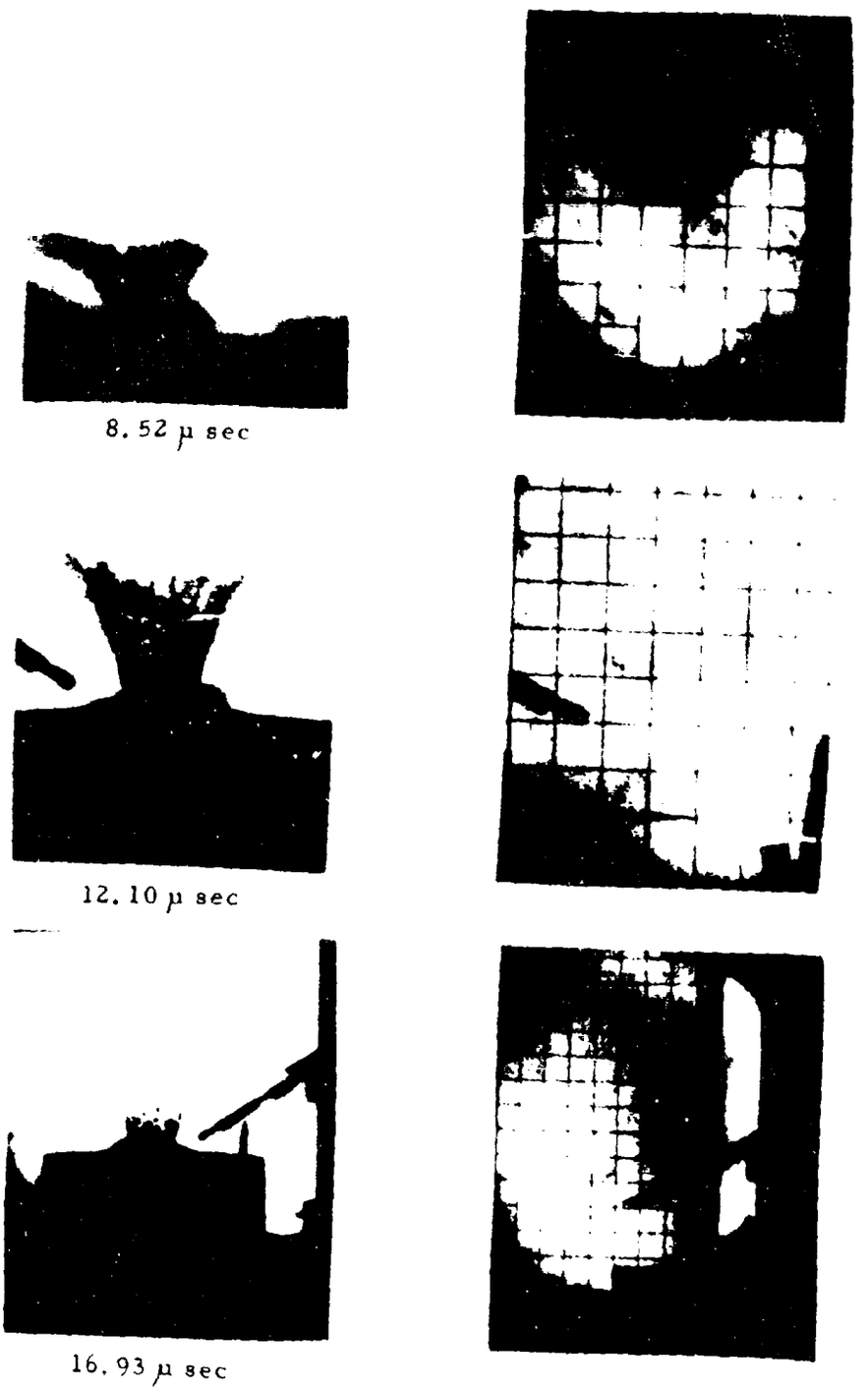

Fig. 34. Image Converter Photographs of Ejecta Cloud and Calibration Grid, Shot #2464 (Grid Wire Spacing is 1.27 cm)

An example of raw data from the image converter photographs of shot #2464 appears in Appendix B. As in the case of the B&W 300 ejecta cloud-edge photographs, polynomials were fit to the real-space coordinates of the cloud edges determined from the image converter photographs using a standard least-squares program. The two edges of the cloud were treated separately because, as in the earlier case, the cloud edges were not symmetrical. Fourth-order polynomials were employed in all cases, since the maximum RMS error of 0.3 mm was deemed acceptable. Examples of the computer program output appear in Table VII.

Unlike the earlier results, the computer output resulting from the image converter photograph data appears internally consistent, i.e., origin of ejection, angle, and velocity all appear to be behaving reasonably within the range of about 4.42 to 5.69 microseconds after impact. Since the time of the first photograph was only 8.52 microseconds after impact, erratic outputs for times approaching this value are to be expected due to the very short trajectory distance between the "A" curve and the origin. However, the failure of the program to obtain data for times earlier than 4.42 microseconds is not as easily understood. Analysis of the reason for convergence failure within the program indicates that just as was the case with shot #2385, the third or "C" curve is flattening out to such an extent that a correct geometric straight-line, constant-velocity solution cannot be obtained. As can be inferred from Fig. 31, particle deceleration appears

TABLE VII

Cloud-Edge Computer Program Outputs, Shot #2464

Time of Ejection (μ sec)	Origin (cm)	Angle (Deg)	Velocity (km/sec)
4.42	.282	61.5	3.42
4.54	.309	62.2	3.42
4.67	.324	62.4	3.41
4.79	.339	62.6	3.40
4.91	.353	62.7	3.39
5.02	.367	62.9	3.37
5.16	.384	63.1	3.35
5.27	.397	63.2	3.33
5.37	.410	63.4	3.30
5.47	.423	63.5	3.26
5.55	.435	63.6	3.20
5.63	.446	63.6	3.14
5.68	.457	63.6	3.04
5.69	.463	63.6	2.97

capable of producing this effect. A further reduction in target tank pressure might prevent particle deceleration, but such vacuums are difficult to secure and maintain.

Although neither the cloud-edge computer program nor the discrete-particle computations were successful in consistently determining crater parameters as functions of time, the changes in width of the base and throat of the ejecta cloud present an interesting insight into the method of crater formation. These two cloud parameters were determined in as many photographs as possible, and the resulting data are plotted on Fig. 35 along with the best-fit curve of crater diameter growth. The data are presented as ratios of the value of the appropriate parameter to its final value, as determined from late-time photographs in which the parameters stopped increasing and exhibited only random variations around the (assumed) final value. In very early times, the base width increases more rapidly than the actual crater as can be seen from Fig. 35. The throat lags behind both, clearly indicating that, in these times, the crater is expanding faster than the radial component of effective ejecta velocity.

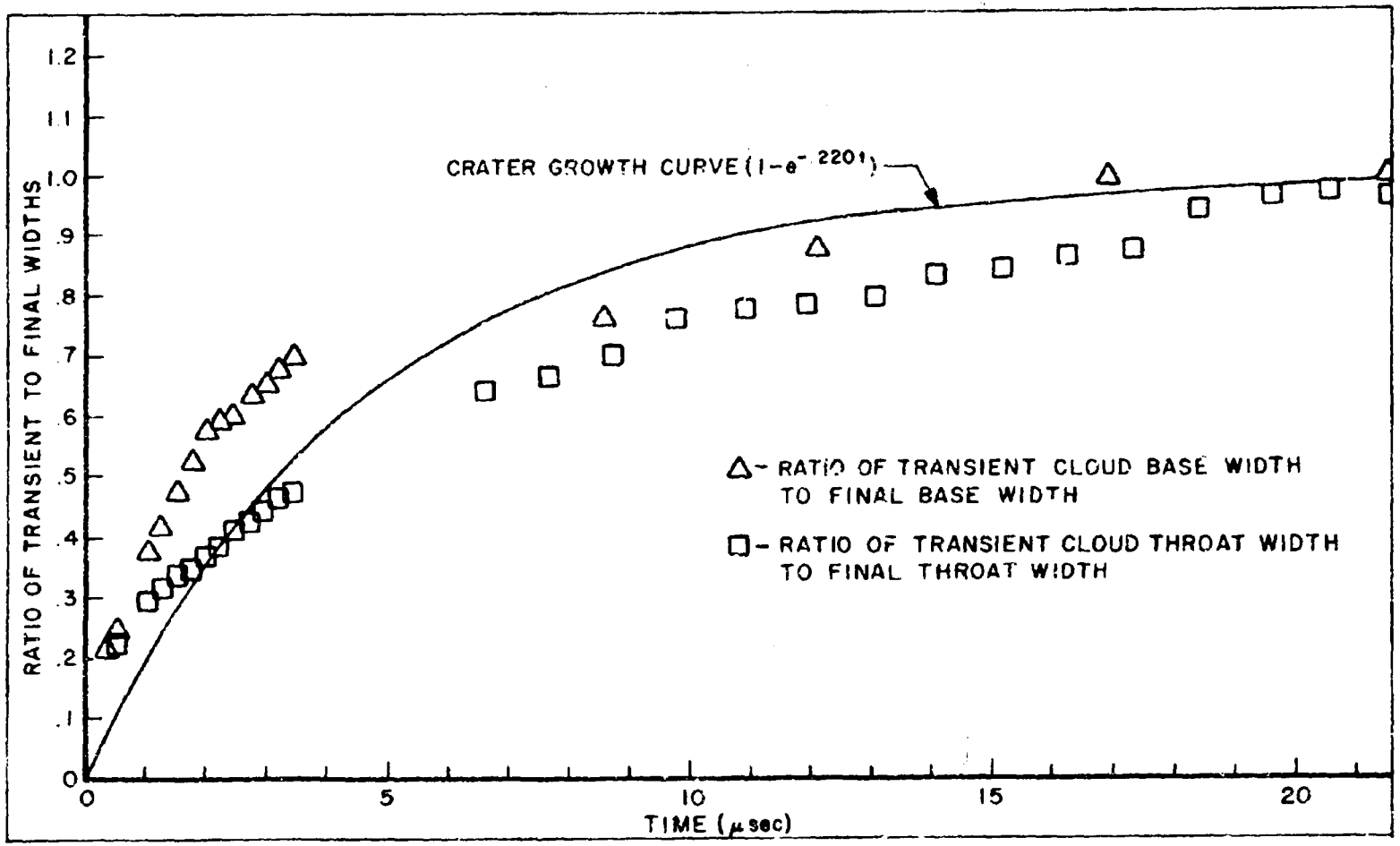

Fig. 35. Plots of Ejecta Cloud Base and Throat Growth

V. Discussion of Results, Conclusions, and Recommendations

Discussion of Results

The purpose, instrumentation, and general results of each of the six shots contributing data to this investigation are summarized in Table VIII. The internal consistency of crater growth data (Figs. 22 and 23) acquired from the radiographs is excellent. The shape of the diameter growth curve (Fig. 22) is in general agreement with results obtained by Charters *et al.* (Ref 3:281) for 1100-0 aluminum-on-aluminum impacts at only slightly higher velocities (7.4 km/sec vs. 7.0 km/sec used for this study). However, the absolute diameters reported by Charters are 30-40% greater than the crater diameters achieved in this study. [Crater parameters measured during this study appear consistent with previous AFML results and with other published results (Ref 26).] The cause of the disagreement is felt to lie in Charters' measurement technique. Apparently he measured the base of the ejecta cloud and considered it equivalent to crater diameter (Ref 3:280). Results achieved in the study being reported show that there is an appreciable and varying difference between these two parameters (see Fig. 22). To further clarify the relationships between cloud and crater dimensions, the ejecta cloud base diameters, throat widths, and crater diameter growth curve of the present study are plotted in Fig. 36 together with Charters' curve of crater diameter growth. It is doubtful that the slight difference in velocities between

TABLE VIII

Purpose, Instrumentation, and General Results of Shots

Shot No.	Date	Purpose	Instrumentation	Timing Initiation Method	General Results
2384	12-21-67	Early time optical pictures. x-rays at 4, 6, 8 μ sec.	B&W 300 camera 5 x-rays Fastax camera	Mylar-foil switch	No usable optical pictures (debris from foil switch) 5 usable x-rays: 3.38-5.28 μ sec Fastax film record OK
2385	12-28-67	Early time optical pictures. x-rays at 1, 2, 3 μ sec. Record of impact flash.	B&W 300 camera 5 x-rays Dynafax camera Fastax camera	Ion probe switch	13 usable frames of optics (Kerr cell cut early) 5 usable x-rays: 2.99-4.78 μ sec No Dynafax record (shutter mal function) Fastax film record OK
2386	12-29-67	same as 2385	same as 2385	Ion probe switch	Optical pictures badly rewritten Dynafax record

Table VIII (Continued)

Shot No.	Date	Purpose	Instrumentation	Timing Initiation Method	General Results
2386 (con't)					rewritten (ion switch failure) 5 usable x-rays: 13.26-15.66 μ sec Fastax film record OK
2387	1-4-68	Full optical coverage. x-rays at 15, 30, 45 μ sec Record of impact flash	same as 2385	Mylar-foil switch	Optics rewritten but usable (Kerr cell failure) 3 usable x-rays: 23-51 μ sec Impact flash recorded No Fastax film record (film broke)
2463	3-7-68	3 Image converter pictures at 4, 8, 12 μ sec	3 Image converters Dynafax camera Fastax camera	Photo-multiplier tube sensing impact flash	Pictures at 7.45, 10.89, 14.89 μ sec (film buckled in cassette on #1 camera) Impact flash recorded

Table VIII (Continued)

Shot No.	Date	Purpose	Instrumentation	Timing Initiation Method	General Results
2463 (con't)					Fastax film record OK
2464	3-8-68	3 Image converter pictures at 6, 11, 16 μ sec	same as 2463	same as 2463	Usable pictures at 8.52, 12.10, 16.93 μ sec Impact flash recorded Fastax film record OK

Note: Target tank ambient pressure was as follows:
Shot #2384-2387 - 25.2 torr
Shot #2463 - .175 torr
Shot #2464 - .090 torr

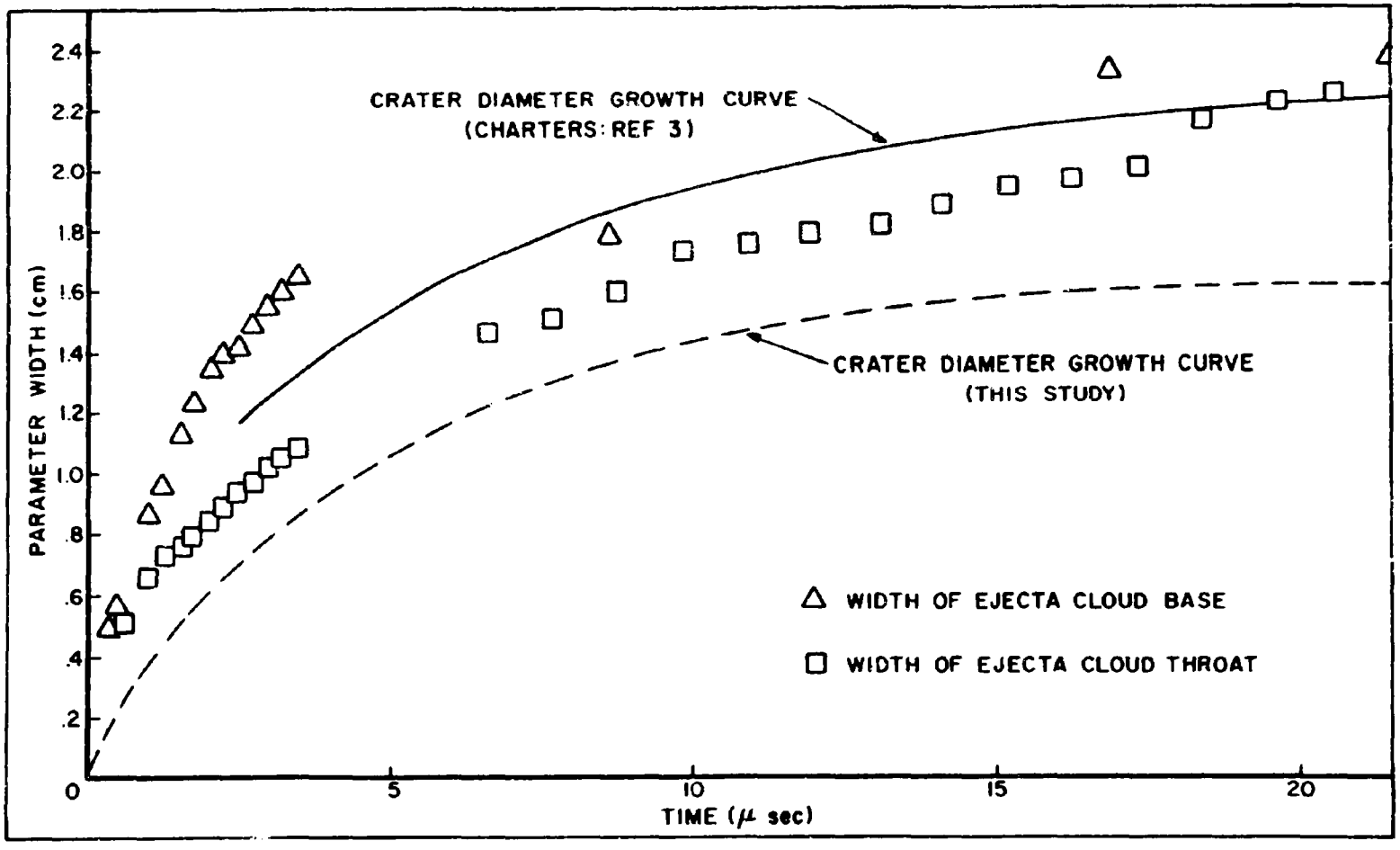

Fig. 36. Comparison of Ejecta Cloud Base and Throat Data With Crater Diameter Growth Curves

the two experiments could account for the large disparity in reported diameters. In any event, the figure demonstrates that cloud base cannot be considered equivalent to actual crater diameter.

Both crater diameter and depth data were found to follow very closely a growth law of the form $R = 1-e^{-kt}$, where R is the ratio of transient to final crater dimension, k is the fitting parameter ($k \approx 0.22$ for the case considered), and t = time in microseconds after impact. The decision to apply such an exponential curve to the data was based solely on the appearance of the data, and no physical justification for this type of growth law is proposed. If such an exponential growth law were to prove applicable over wider energy ranges and for a variety of target materials, it would provide a valuable tool for testing theoretical treatments.

The radiographs demonstrate that the crater assumes its characteristic shape very early in the cratering process and retains this shape as it grows in size. Ideal hypervelocity impact craters are almost universally described as "hemispherical". This judgment appears to be based largely (if not entirely) on the close agreement between values of depth and radius. But the tangent to a hemispherical crater at the target surface would always make an angle of 90 degrees with the target face. The value of this angle determined in this study remained almost constant at 77 ± 4 degrees. It is therefore concluded that the true shape of the crater is not hemispherical but is better represented by a paraboloid.

The x-ray techniques employed in this study appear very promising. In particular, the comparative technique for obtaining crater measurements appears to offer advantages of ease and simplicity over any absolute method, such as the use of reference grids. The capability of making usable radiographs of transient craters in solid aluminum targets has been demonstrated. It is felt that careful analysis of radiographs obtained earlier in the process, when the crater lip is first being formed, may give additional insight into the mechanics of crater formation and ejection.

The fact that the crater achieves its final shape early in the crater growth process increases the problems associated with using ejecta cloud information to predict crater growth parameters. It was discovered that no reasonable estimate of crater size and shape could be obtained from the ejecta cloud photographs. The failure of the computer program to predict correctly the time variation of crater growth parameters must result from one or more of the following causes: (1) inaccuracies in determining true ejecta cloud edge position from the photographs, (2) inaccuracies in determining the times at which the cloud edge photographs were taken, or (3) invalidity of the assumption that the ejecta travels in straight lines at constant velocities.

The importance of timing and positional errors was investigated by a series of program sensitivity tests. Artificially generated cloud curves (described in Chapter II) were altered by flattening out

the "C" curve. The resulting curve resembled the curve produced by decelerating particles. Then both the correct curves and the altered curves were inserted into the cloud-edge computer program with both correct and slightly altered time information. The results of these sensitivity tests appear in Table IX. Details of the sensitivity tests and complete output data are contained in Appendix D.

This exercise demonstrated that the computer program is sensitive to program inputs. An error of more than about 5% in the time between cloud edge positions or a systematic error of about 5% in the position of a cloud edge appears capable of invalidating program outputs. In particular, it is interesting to note the similarity between program output for the artificially flattened curve and that from shot #2385 (Table V). In both instances the computed ejecta velocity increased with time and the angle decreased. (These trends are the opposite of expected behavior.) Also, it appeared that the origin was starting to move back in toward the centerline on the last output from shot #2385, as it did consistently with the altered curves.

These similarities might indicate that the cloud edge data obtained with the B&W 300 camera records were insufficiently precise in either spatial or time resolution to permit program solution. On the other hand, the same result would occur if the particles were being decelerated. Particle deceleration computations (Appendix C) indicate that particles of 10 μ diameter would lose 5% of their velocity (assumed

TABLE IX

Results of Cloud-Edge Computer Program Sensitivity Tests

Test Conditions	Resultant Errors			
	Time of Ejection	Origin	Angle	Velocity
A. All Curves Spatially Correct				
1. Time of curve A decreased by 6% of (TB-TA)	error < 3%	-8 to 24%	-3 to 8%	+5 to 12%
2. Time of curve A increased by 6% of (TB-TA)	error <4%	+6 to 18% moves in wrong direction	+2 to 7%	-3 to 10%
3. Time of curve A increased by 2% of (TB-TA)	error < 2%	+3 to 8%	error < 3%	error < 5%
4. Time of curve A increased by 1% of (TB-TA)	no appreciable error	error < 4%	error < 2%	no appreciable error
B. Curve C Flattened by Increasing y-Values by 5% Above Throat of Curve (max. absolute error ~.5 mm)				
1. Times all correct	-25 to 50%	+12 to 35% moves in wrong direction	+5 to 14% and decreases	-20 to 32% and increases
2. Time of curve A increased by 5% of (TB-TA)	-28 to 55%	+19 to 44% moves in wrong direction	+8 to 17% and decreases	-24 to 37% and increases

initially at 7 km/sec) over a travel of about 2.4 cm. It does not seem unreasonable that particles in the early ejecta could be this small, or somewhat smaller.

In order to reduce the effects of atmospheric drag, a second series of impact experiments was carried out at an ambient pressure of only .09 torr. At this pressure, particles would have to approach 0.1 μ in size before they would experience a 5% velocity loss over 6.7 cm of travel. It appears extremely unlikely that all or a majority of the particles forming the cloud edge would be this small. A highly precise image converter camera system replaced the framing camera to eliminate significant time and positional errors from the cloud photographs in these experiments.

Finally, the results of the discrete-particle measurements of shot #2387 can hardly be ascribed to deceleration caused by atmospheric drag. All of these particles were in the range of 0.25 mm and larger. Particles of this size should travel more than 20 cm before experiencing a 5% velocity loss at 25.5 torr atmospheric pressure. So, clearly, the unreasonable ejection times obtained for these particles cannot be attributed to simple particle deceleration due to atmospheric drag. Although there was undoubtedly error in determining their positions, the errors should have been random and not such as to give the consistently early ejection times appearing in Table VI. It is proposed that the deceleration of these large particles is caused by their collision with smaller particles ejected at earlier

times and themselves decelerated. Hence the assumption of constant-velocity travel after ejection is not tenable.

It is appropriate here to review the assumptions that formed the basis for the ejecta cloud investigation and to assess their validity in the light of information provided by this study.

1. It was assumed that the angle between the crater wall at the target surface and the target face increases during crater growth. The radiographic investigation demonstrated that this angle remains approximately constant during almost the entire crater growth process.
2. It was further assumed that material departs the crater along vectors tangent to the crater wall at positions corresponding to the limits of crater radius. Measurements of cloud base and throat diameters do not agree with radiographic determination of instantaneous crater radius. No relationship between these parameters has yet been found.
3. The ejecta was assumed to travel in straight lines at constant velocity after departing the target face. It is strongly indicated that at normal range ambient pressures ($\sim$25 torr) the ejecta cloud is significantly decelerated by atmospheric drag over the distances required for the ejecta cloud study. Discrete particle measurements prove that

other deceleration forces are acting on at least the late time ejecta cloud.

4. It was assumed that as the pressure in the crater dissipates, the velocity of ejection decreases. Comparison of over-all movement of the early ejecta cloud with measured velocities of particles in the late time cloud grossly support this assumption.

5. Finally, it was assumed that at any instant, particles are being ejected at nearly identical velocities. No supporting or refuting evidence is available from this study.

The proven invalidity of assumptions 1 through 3 is felt to constitute the reasons for the failure of the computer program to predict crater parameters as a function of time. The assumption of constant-velocity, straight-line ejecta travel is essential for the proposed ejecta cloud solution. Therefore the direct determination of crater radius as a function of time from either cloud-edge data or discrete particle measurements does not appear promising. It may be possible to correlate crater radius with such gross parameters of the ejecta cloud as throat and base width, but further investigation will be required to establish a relationship between these parameters.

Conclusions

The conclusions drawn in the preceding discussion can be summarized as follows:

a. The crater assumes its final shape very early in the ejection process, certainly before 3 microseconds for the experiments being reported. This shape remains virtually unchanged as the crater continues to expand. No significant evidence of "springback" or reduction in crater size at late time was apparent in this investigation.

b. The tangent to the crater wall at the target surface was found to make an angle of 77 ± 4 degrees with the target face throughout the course of crater formation. Hence the crater is not actually hemispherical but is probably better represented by a paraboloid.

c. Radiographs appear to offer the best means of observing crater growth as a function of time. The determination of transient crater parameters by the direct comparison of radiographs taken during and after the event under identical geometric relationships is both feasible and preferable to any known absolute technique.

d. Of the two types of radiographs employed in the study, profile views of the crater seem far superior to plan views. The profile view permits simultaneous determination of both diameter and depth, while the plan view gives diameter information only. Moreover, the crater lip completely ringing the crater in the plan view makes

determination of true crater diameter more difficult than with the profile-view radiographs.

e. For spherical aluminum projectiles impacting thick 1100-0 aluminum targets at about 7 km/sec, the crater appears to follow an exponential growth law of the form $R = 1-e^{-kt}$, where R is the ratio of crater transient dimension to final dimension. With t measured in microseconds, the value of k determined in this investigation was $0.217 \pm .003$.

f. Use of three optically aligned image converter cameras to obtain optical data of high precision is entirely feasible. Used in conjunction with a Dynafax or similar streaking camera to record impact flash and camera shutter operations, this system is capable of providing time resolution on the order of 40 nanoseconds.

g. There may be a relationship between gross ejecta cloud parameters (such as width of throat and base) and crater radius. But additional evidence will be required to determine what relationship (if any) exists.

h. The simple model proposed at the outset of the study--ejecta particles departing the crater wall on a tangent and traveling in straight lines at constant velocity--does not agree with the physical reality. Particle interaction after ejection seems quite probable, with resultant changes in both particle speed and direction.

Recommendations

The following recommendations are made for additional work in areas investigated in this study:

a. Additional radiographs should be made to observe crater growth, especially in the very early ($< 3\ \mu$ sec) and middle (20-40 μ sec) stages. If the additional data points conform to the proposed growth law, comparison should be possible with theoretical blast-wave and hydrodynamic treatments.

b. Further study should be made of the precise shape of the crater during its formative stage. Again, these results should permit comparison with theoretical predictions.

c. Three image converter cameras should be used to photograph discrete-particle ejecta. In order to be able to identify and follow the particles, the pictures should be taken 2 to 3 μ sec apart. Time and spatial resolution should be sufficient to determine whether there is any deviation from straight line travel and any deceleration above that to be expected from atmospheric drag. These shots should be accomplished in as hard a vacuum as can be maintained.

Bibliography

1. Allison, F. E. "Mechanics of Hypervelocity Impact" in Proceedings of the Seventh Hypervelocity Symposium. Vol. V. Orlando, Florida: The Martin Company, 1965.

2. Carey, Donald A. An Investigation of the Debris Cloud Produced by the Impact of Spheres on Thin Metal Sheets. Unpublished thesis. Wright-Patterson Air Force Base, Ohio: Air Force Institute of Technology, June 1967.

3. Charters, A. C., et al. "Impact Physics, Meteoroids and Spacecraft Structures" in The Fluid Dynamics of Space Flight. AGARDograph 87, Vol. I. New York: Gordon & Breach, 1965.

4. Eichelberger, R. J. "Introduction--Experimental Studies" in Proceedings of the Fifth Symposium on Hypervelocity Impact. Vol. I. Golden, Colorado: Colorado School of Mines, 1962.

5. -----. "Summary: Theoretical and Experimental Studies of Crater Formation" in Proceedings of the Sixth Symposium on Hypervelocity Impact. Vol. II. Cleveland, Ohio: The Firestone Tire and Rubber Company, 1963.

6. Engel, Olive G. "Hypervelocity Cratering Data and a Crater-Depth Model for the Regime of Partial Fluidity" in Proceedings of the Sixth Symposium on Hypervelocity Impact. Vol. II. Cleveland, Ohio: The Firestone Tire and Rubber Company, 1963.

7. Feldman, James B., Jr. "Volume-Energy Relations from Shaped Charge Jet Penetrations" in Hypervelocity Impact: Fourth Symposium. Vol. II. Eglin Air Force Base, Florida: Air Proving Ground Center, 1960.

8. Frasier, J. T., et al. "The Behavior of Wax Targets Subjected to Hypervelocity Impacts" in Proceedings of the Seventh Hypervelocity Symposium. Vol. V. Orlando, Florida: The Martin Company, 1965.

9. Gault, Donald E. and Ezra D. Heitowit. "The Partition of Energy for Hypervelocity Impact Craters Formed in Rock" in Proceedings of the Sixth Symposium on Hypervelocity Impact. Vol. II. Cleveland, Ohio: The Firestone Tire and Rubber Company, 1963.

10. Gehring, J. William, Jr., et al. "Experimental Studies of Impact Phenomena and Correlation With Theoretical Models" in Proceedings of the Seventh Hypervelocity Symposium. Vol. V. Orlando, Florida: The Martin Company, 1965.

11. Halperson, S. M. "Comparisons Between Hydrodynamic Theory and Impact Experiments" in Proceedings of the Seventh Hypervelocity Symposium. Vol. V. Orlando, Florida: The Martin Company, 1965.

12. Hermann, Walter and Arfon H. Jones. "Correlation of Hypervelocity Impact Data" in Proceedings of the Fifth Symposium on Hypervelocity Impact. Vol. I. Golden, Colorado: Colorado School of Mines, 1962.

13. Hildebrand, Joel H. An Introduction to Molecular Kinetic Theory. New York: Reinhold Publishing Corp., 1963.

14. Kineke, John H., Jr. "Observations of Crater Formation in Ductile Materials" in Proceedings of the Fifth Symposium on Hypervelocity Impact. Vol. I. Golden, Colorado: Colorado School of Mines, 1962.

15. Kineke, J. H., Jr. and L. G. Richards. "Influence of Target Strength on Hypervelocity Crater Formation in Aluminum" in Proceedings of the Sixth Symposium on Hypervelocity Impact. Vol. II. Cleveland, Ohio: The Firestone Tire and Rubber Company, 1963.

16. Kinslow, Ray. "Properties of Spherical Shock Waves Produced by Hypervelocity Impact" in Proceedings of the Sixth Symposium on Hypervelocity Impact. Vol. II. Cleveland, Ohio: The Firestone Tire and Rubber Company, 1963.

17. MacCormack, Robert W. Impact Flash at Low Ambient Pressures. NASA Technical Note D-2232. Washington, D. C.: National Aeronautics and Space Administration, 1964.

18. Maiden, C. J., et al. "An Investigation of Spalling and Crater Formation by Hypervelocity Projectiles" in Hypervelocity Impact: Fourth Symposium. Vol. III. Eglin Air Force Base, Florida: Air Proving Ground Center, 1960.

19. Olshaker, A. E. and R. L. Bjork. "Hydrodynamics Applied to Hypervelocity Impact: I. Scaling Laws for Dissimilar Materials" in Proceedings of the Fifth Symposium on Hypervelocity Impact. Vol. I. Golden, Colorado: Colorado School of Mines, 1962.

20. Operating Manual. Model 300 Continuous Writing Framing Camera. San Carlos, California: Beckman & Whitley, May 1966.

21. Öpik, Ernst J. Physics of Meteor Flight in the Atmosphere. New York: Interscience Publishers, Inc., 1958.

22. Pond, R. B., et al. "Energy Balances in Hypervelocity Penetration" in Proceedings of the Sixth Symposium on Hypervelocity Impact. Vol. II. Cleveland, Ohio: The Firestone Tire and Rubber Company, 1963.

23. Rae, William J. and Henry P. Kirchner. "A Blast-Wave Theory of Crater Formation in Semi-Infinite Targets" in Proceedings of the Sixth Symposium on Hypervelocity Impact. Vol. II. Cleveland, Ohio: The Firestone Tire and Rubber Company, 1963.

24. Riney, T. D. and P. R. Chernoff. "Inertial, Viscous, and Plastic Effects in High Speed Impact" in Proceedings of the Fifth Symposium on Hypervelocity Impact. Vol. I. Golden, Colorado: Colorado School of Mines, 1962.

25. Rolsten, Robert F. Hypervelocity Impact Studies. Technical Report AFML-TR-66-40. Wright-Patterson Air Force Base, Ohio: AFML, March 1966.

26. Sorensen, Neil R. "Systematic Investigation of Crater Formation in Metals" in Proceedings of the Seventh Hypervelocity Symposium. Vol. VI. Orlando, Florida: The Martin Company, 1965.

27. Summers, James L. and A. C. Charters. "High Speed Impact of Metal Projectiles in Targets of Various Materials" in Proceedings of the Third Symposium on Hypervelocity Impact. Vol. I. Chicago: Armour Research Foundation, 1959.

28. Swift, H. F. The Air Force Materials Laboratory Hypervelocity Ballistic Range. Technical Report AFML-TR-67-2. Wright-Patterson Air Force Base, Ohio: AFML, January 1967.

29. Swift, H. F. and E. Strader. "Flash X-ray Actuated Trigger Switch". Review of Scientific Instruments (in press).

30. Walsh, J. M. and J. H. Tillotson. "Hydrodynamic of Hypervelocity Impact" in Proceedings of the Sixth Symposium on Hypervelocity Impact. Vol. II. Cleveland, Ohio: The Firestone Tire and Rubber Company, 1963.

Appendix A

Computer Program for Determining Crater Parameters From Ejecta Cloud Edge Positions

Since the logic of the program is discussed in Chapter II, this Appendix will be limited to a discussion of program inputs and outputs. Because all measurements were obtained in English units, the program was written with inputs and outputs expressed in these units. Conversion to the mks-cgs system was made prior to presentation of the data in the main body of this report. Program inputs and outputs are listed below, followed by a machine printout of the entire program.

Program Inputs

X(1, 1)	- Distance (in inches) from target face to starting point on first curve (curve A).
START	- Distance (in inches) on target face from cloud centerline to assumed point of origin of particle passing through X(1, 1).
XBLIM	- Limiting distance (in inches) from target face along curve B of acceptable solutions. (Outside the limits of measurement, the fitted curves do not necessarily represent actual cloud edge positions.)
XCLIM	- Similar limiting distance on curve C.

TBASE	- Assumed time after impact (in nanoseconds) of ejection of particle passing through X(1, 1).
TA	- Time after impact (in nanoseconds) of curve A.
TB	- Time after impact (in nanoseconds) of curve B.
TC	- Time after impact (in nanoseconds) of curve C.
C(I, J)	- Coefficients of curves fit to cloud edge data. I(1-3) identifies curves A-C. J(1-11) identifies coefficient of terms x^0 through x^{10}.
JLIM	- Number of straight-line trajectory outputs desired.
KLIM, LLIM, ILIM	- Internal iteration-number limits.
DELTAX	- Increment of x-movement desired along curve A between separate straight-line trajectory solutions.
TOLINT	- Acceptable tolerance on iteration routine to establish intersections of straight-line trajectories and cloud-edge curves.
DISTOL	- Acceptable tolerance on iteration routine to adjust distance-time ratios along straight-line trajectories between curves.
ADJFAC	- Sensitivity adjustment factor to control distance assumed origin is moved to correct above ratios.

Program Outputs

TIME	- Time after impact of ejection of particle (nanoseconds).
ORIGIN	- Lateral (or y-) distance (in inches) along target face from cloud centerline to point of ejection of particle (In the assumed model, this corresponded to crater radius.)
ANGLE	- Angle of ejection (in degrees) of particle measured from plane of target face.
VELOCITY	- Velocity of ejected particle (in feet/sec).
XA, YA	- Coordinates (in inches) of point on curve A through which particle passed.
XB, YB	- Same information for curve B.
XC, YC	- Same information for curve C.

```
C PROGRAM TO DETERMINE TIMES, ORIGINS, ANGLES, AND VELOCITIES OF EJECTA
C PARTICLES
C
C THIS IS THE MAIN PROGRAM
C
      COMMON C(3,11)
      DIMENSION X(3, 100), Y(3, 100), ORIGIN(100), PHIDEG(100), VPART(10
     10), TIME(100)

C CLEAR ARRAYS

    1 DO 51 J = 1, 100
      ORIGIN(J) = 0.0
      PHIDEG(J) = 0.0
      TIME(J) = 0.0
      DO 51 I = 1, 3
      X(I,J) = 0.0
   51 Y(I,J) = 0.0

C READ INPUT DATA - START POINT ON FIRST CURVE, ASSUMED ORIGIN,
C OUTER DATA LIMITS,PHOTO TIMES, COEFFICIENTS OF CURVES, COUNTER LIMITS,
C DELTAX, INTERSECTION TOLERANCE, DISTANCE TOLERANCE, AND ADJUSTMENT
C FACTOR
C
C DISTANCES ARE IN INCHES, TIMES IN NANOSECONDS
C
```

```
C
  999 READ (5, 101) X(1,1), START, XBLIM, XCLIM, TBASE, TA, TB, TC
  101 FORMAT (7F10.0/F10.0)
      READ (5, 102) ((C(I,J), J = 1, 11), I = 1, 3)
  102 FORMAT (1P5E14.6/1P5E14.6/1PE14.6)
      READ (5, 103) JLIM, KLIM, LLIM, ILIM
  103 FORMAT (4I10)
      READ (5, 104) DELTAX, TOLINT, DISTOL, ADJFAC
  104 FORMAT (1P4E10.4)
      WRITE (6, 11) X(1, 1), START, XBLIM, XCLIM, TBASE, TA, TB, TC
   11 FORMAT (1H1, 5HXA = , F7.5, 9H START = , F7.5,9H XBLIM = , F7.5,
     19H XCLIM = , F7.5, 9H TBASE = , F7.1, 6H TA = , F10.1, 6H TB = ,
     2F10.1, 6H TC = , F10.1)
      WRITE (6, 12) ((C(I,J), J = 1, 11), I = 1, 3)
   12 FORMAT (1H , 18HCURVE COEFFICIENTS/1P5E14.6/1P5E14.6/1PE14.6)
      WRITE (6, 13) DELTAX, TOLINT, DISTOL, ADJFAC
   13 FORMAT (1H , 9HDELTAX = , F7.5, 10H TOLINT = , F7.6, 10H DISTOL =
     1, F10.9, 10H ADJFAC = , F5.3)
  200 J = 1
      XB = X(1,J)*(TB - TBASE)/(TA - TBASE)
      XINTA = 0.0
      XINTB = 0.0
  204 GUESS = START
  202 K = 1
  205 CALL VALUE (1, YA, X(1,J))
  208 SLOPE = X(1,J)/(YA - GUESS)

C FIND INTERSECTION OF LINE AND SECOND CURVE

  206 CALL NEWTON (2, XBINT, XB, GUESS, SLOPE, TOLINT, 0)
      IF (MOVEOR .EQ. 1) GO TO 208
  207 IF (XBINT .LT. XINTA .OR. XBINT .GT. XBLIM) GO TO 201
      XB = XBINT
      GO TO 151
```

```
201 K = K + 1
    IF (K .GT. KLIM) GO TO 203
    IF (XBINT .LT. XINTA) XB = 1.05*XB
    IF (XBINT .GT. XBLIM) XB = 0.95*XB
    GO TO 206

C INCREMENT J AND GO TO NEXT POINT ON FIRST CURVE

203 J = J + 1
    IF (J .GT. JLIM) GO TO 157
    X(1,J) = X(1,1) + FLOAT(J-1)*DELTAX
    XB = X(1,J)*(TB - TBASE)/(TA - TBASE)
    GO TO 204
151 CALL VALUE (2, YB, XB)

C FIND INTERSECTION OF LINE AND THIRD CURVE

    K = 1
    XC = X(1,J) + (XB - X(1,J))*(TC - TA)/(TB - TA)
216 CALL NEWTON (3, XCINT, XC, GUESS, SLOPE, TOLINT, 0)
    IF (MOVEOR .EQ. 1) GO TO 208
217 IF (XCINT .LT. XINTB .OR. XCINT .GT. XCLIM) GO TO 211
    XC = XCINT
    GO TO 161
211 K = K + 1
    IF (K .GT. KLIM) GO TO 203
    IF (XCINT .LT. XINTB) XC = 1.05*XC
    IF (XCINT .GT. XCLIM) XC = 0.95*XC
    GO TO 216
161 CALL VALUE (3, YC, XC)
```

```
C COMPUTE  DISTANCES BETWEEN INTERSECTIONS

      L = 1
  500 DISONE = DIST (XB, X(1,J), YB, YA)
      DISTWO = DIST (XC, XB, YC, YB)
      ERROR = DISTWO/(TC - TB) - DISONE/(TB - TA)
      IF (ABS(ERROR) .LE. DISTOL) GO TO 501

C ADJUST ORIGIN TO CORRECT DISTANCE RATIO

  502 ADJUST = (ADJFAC*(TA - TBASE)/(TC - TA))*(DISTWO*(TB - TA)/(DISONE
     1*(TC - TB)) - 1.0)*(-1.0)
  503 ADJOR = GUESS + ADJUST
      L = L + 1
      IF (L .GT. LLIM) GO TO 203
      IF (ADJOR .GT. YA .OR. ADJOR .LT. 0.0) GO TO 504
      GUESS = ADJOR
      K = 1
      GO TO 208
  504 ADJUST = ADJUST/2.0
      GO TO 503

C STORE ORIGIN, ANGLE, VELOCITY, TIME OF EJECTION, AND COORDINATES

  501 ORIGIN(J) = GUESS
      PHIDEG(J) = 57.295795*ATAN(X(1,J)/(YA - GUESS))
      VPART(J) = (DISONE + DISTWO)/((TC - TA)*12.0E-9)
      TIME(J) = TA - DIST(X(1,J), 0.0, YA, GUESS)*(TC - TA)/(DISONE + DI
     1STWO)
      Y(1,J) = YA
      X(2,J) = XB
      Y(2,J) = YB
      X(3,J) = XC
      Y(3,J) = YC
```

```
C PRINT OUT RESULTS
      WRITE (6, 153) J, TIME(J), GUESS, PHIDEG(J), VPART(J), X(1,J), YA,
     1XB, YB, XC, YC
  153 FORMAT (1H0, 2HJ=, I2, 6H TIME=, F8.1, 8H ORIGIN=, F6.5,7H ANGLE=,
     1F6.3, 5H VEL=, F10.1, 4H XA=, F7.5, 4H YA=, F7.5, 4H XB=, F7.5,
     24H YB=, F7.5, 4H XC=, F7.5, 4H YC=, F7.5)

C INCREMENT J AND RETURN TO BEGINNING OF PROGRAM

      J = J + 1
      IF (J .GT. JLIM) GO TO 157
      TBASE = TIME(J-1)
      X(1,J) = X(1,J-1) + DELTAX
      GO TO 202

C PRINT OUT STORED DATA AT COMPLETION OF PROGRAM

  157 WRITE (6, 154)
  154 FORMAT (1H1, 12H TIME (NSEC), 12H ORIGIN (IN), 12H ANGLE (DEG),
     115H VELOCITY (FPS), 4X, 8H XA (IN), 4X, 8H YA (IN), 4X, 8H XB (IN)
     2, 4X, 8H YB (IN), 4X,8H XC (IN), 4X, 8H YC (IN)/)
      WRITE (6, 155) (TIME(J), ORIGIN(J), PHIDEG(J), VPART(J), X(1,J),
     1Y(1,J), X(2,J), Y(2,J), X(3,J), Y(3,J), J = 1, JLIM)
  155 FORMAT (3X, F7.1, 5X, F7.5, 5X, F6.3, 8X, F8.1, 8X, F7.5, 5F12.5)

C RECYCLE TO BEGINNING OF PROGRAM FOR ADDITIONAL INPUTS

      GO TO 1

      END
```

```
C SUBROUTINE TO COMPUTE VALUE OF A POLYNOMIAL

      SUBROUTINE VALUE (I, YVAL, XVAL)
      COMMON C(3, 11)
      YVAL = C(I,1)
      DO 301 J = 2, 11
  301 YVAL = YVAL + C(I,J)*XVAL**(J-1)
      RETURN
      END


C SUBROUTINE TO COMPUTE VALUE OF FIRST DERIVATIVE OF A POLYNOMIAL
      SUBROUTINE PRIME (I, YPRIME, XVAL)
      COMMON C(3, 11)
      YPRIME = C(I,2)
      DO 302 J = 3, 11
  302 YPRIME = YPRIME + FLOAT(J-1)*C(I,J)*XVAL**(J-2)
      RETURN
      END


C FUNCTION TO COMPUTE DISTANCE BETWEEN TWO POINTS

      FUNCTION DIST (XOUT, XIN, YOUT, YIN)
      DIST = SQRT((XOUT - XIN)**2 + (YOUT - YIN)**2)
      RETURN
      END
```

```
C SUBROUTINE TO FIND INTERSECTION OF CURVE AND STRAIGHT LINE
      SUBROUTINE NEWTON (I, XINT, XGUESS, GUESS, SLOPE, TOLINT, MOVEOR)
      COMMON C(3, 11)
      N = 1
      XINT = XGUESS
  310 XOLD = XINT
      CALL VALUE (I, YN, XINT)
      CALL PRIME (I, YNP, XINT)
      EX = YN - (XINT/SLOPE) - GUESS
      EXP = YNP - (1.0/SLOPE)
      XINT = XOLD - (EX/EXP)
      ERFUN = ABS(1.0 - (XOLD/XINT)) - TOLINT
      IF (ERFUN) 311, 312, 312
  312 N = N + 1
      IF (N .GT. 150) GO TO 313
      GO TO 310
  313 GUESS = 0.95*GUESS
      MOVEOR = 1
  311 RETURN
      END
```

Appendix B

Raw Data and Sample Computations

1. Time Computations (Shot 2464)

The computations carried out to determine times after impact of image converter camera shutter operations are presented as an example of similar time-determinations made on all experiments. Three separate readings were obtained for each distance on both the Fastax and Dynafax film records. In the interest of brevity, only one set of readings and computations will be presented. T_o represents the winker fired by the PM tube output.

Fastax Record:

Average film speed (mm/millisec)	60.052
Distance: T_o-Shutter Signal 1 (mm)	.480
T_o-Shutter Signal 2 (mm)	.696
T_o-Shutter Signal 3 (mm)	.994

Distances were then divided by speeds to obtain times:

Time: T_o-Shutter Signal 1 (μsec)	7.993
T_o-Shutter Signal 2 (μsec)	11.590
T_o-Shutter Signal 3 (μsec)	16.552

Dynafax Record:

Distance: T_o-Shutter Signal 1 (in)	.0781
T_o-Shutter Signal 2 (in)	.1115
T_o-Shutter Signal 3 (in)	.1572
Impact - T_o (in)	.0040

Distances were divided by (Fastax) times to obtain film speed values:

Apparent film speed:	T_o-Shutter Signal 1 (in/μsec)	.0097710
	T_o-Shutter Signal 2 (in/μsec)	.0096204
	T_o-Shutter Signal 3 (in/μsec)	.0094973
Average film speed	(in/μsec)	.0096296

This value of Dynafax film speed was then applied to determine relative times:

Impact - Shutter Signal 1	8.526 μsec
Impact - Shutter Signal 2	11.994 μsec
Impact - Shutter Signal 3	16.740 μsec

The time values from each of the three separate computations were then averaged to produce the final values of 8.52, 12.10, and 16.93 μsec.

2. Optical Data

a. Discrete Particle Computations. Twenty discrete particles were identified in B & W 300 camera frame 36 of shot #2387 and followed through frame 44. Their x- and y-travel over this time-span (8.62 μsec) were determined. Distances divided by time yielded x- and y- components of velocity. Total distance traveled and total velocity were then determined. The ejection angle was determined as $\tan^{-1}(\Delta x/\Delta y)$. The x-distance of each particle from the target face divided by its x-velocity gave the time of flight. This value substracted from the time of frame 44 (42.236 μsec after impact) yielded the time of ejection. The time of flight of each particle multiplied by its y-velocity gave its y-travel. This value subtracted from its y-distance from cloud centerline gave its radial distance of ejection

(origin). The data for the 20 identified particles appear in Table X. Measurements were made in English units and these are retained in the table. Conversion to the mks system was made as the last step prior to presenting the results in the main body of the report.

b. Image Converter Camera Data. Coordinates of cloud-edge positions were read on the microviewer and converted to true-space coordinates by the application of a demagnification factor determined from the appropriate grid picture (see Fig. 34). Film and real-space x- and y-coordinates for the edges of the outermost or "C" curve are presented in Table XI. The demagnification was 3.34. Distances are in inches for both film and real space.

3. Radiographs

The radiographs from shots #2384, 2385 and 2387 appear as Figs. 37-42.

4. Crater Depth Measurements

Maximum crater depths were measured from the plane of the undisturbed target face. Two diameter measurements were made of each crater along perpendicular traverses. The point was removed from the depth gage in making these measurements to preclude getting an erroneous measurement which would result if the side of the point contacted the crater lip before the point. To compensate for the absence of the point, the shaft diameter was added to the measured value of crater diameter since, at the extremity of each traverse, the shaft contacted the crater wall a distance of one shaft radius prior to

TABLE X

Data Used in Discrete Particle Investigation

Particle No.	ΔX (in)	ΔY (in)	V_x (in/μsec)	V_y (in/μsec)	Distance Traveled (in)	Velocity (fps)	Ejection Angle (deg)	X-POS (in)	Time of Flt. (usec)	Time of Eject. (usec)	Y-POS (in)	Y-Travel (in)	Origin (in)
1	.137	.143	.016	.016	.198	1910	43.8	.677	42.312	-0.08	.817	.677	.150
2	.135	.138	.016	.016	.193	1870	44.4	.653	40.812	1.42	.810	.653	.157
3	.170	.133	.020	.015	.216	2090	52.0	.788	39.400	2.84	.826	.591	.235
4	.247	.177	.029	.020	.304	2940	54.4	1.165	40.172	2.06	.976	.803	.173
5	.261	.182	.030	.021	.318	3080	55.2	1.239	41.300	0.93	.995	.867	.128
6	.287	.194	.033	.022	.332	3210	56.0	1.330	40.303	1.93	1.037	.887	.150
7	.309	.198	.036	.023	.367	3550	57.4	1.513	42.028	0.21	1.119	.967	.152
8	.359	.229	.042	.026	.426	4120	57.5	1.788	42.571	-0.34	1.233	1.107	.126
9	.405	.219	.047	.025	.460	4450	61.6	1.851	39.383	2.85	1.245	.984	.261
10	.165	.139	.019	.016	.216	2090	49.9	.793	41.737	0.50	.828	.668	.160
11	.252	.179	.029	.021	.309	2990	54.6	1.187	40.931	1.30	.982	.860	.122
12	.398	.219	.046	.025	.454	4390	61.2	1.874	40.739	1.50	1.185	1.013	.167
13	.287	.169	.033	.020	.333	3220	59.5	1.365	41.364	0.87	1.019	.827	.192
14	.273	.183	.032	.021	.329	3180	56.2	1.301	40.656	1.58	1.004	.854	.150
15	.267	.171	.031	.020	.317	3070	57.4	1.238	39.935	2.30	.990	.799	.191
16	.306	.198	.035	.023	.364	3520	57.1	1.523	43.514	-1.28	1.081	1.001	.080
17	.342	.196	.040	.023	.394	3810	60.2	1.610	40.250	1.99	1.106	.926	.180
18	.190	.123	.022	.014	.226	2190	57.1	.958	43.545	-1.31	.901	.610	.291
19	.180	.132	.021	.015	.223	2160	53.8	.979	46.619	-4.38	.916	.699	.217
20	.222	.151	.026	.018	.268	2600	55.8	1.035	39.808	2.43	.936	.716	.220

TABLE XI

Film and Real-Space Coordinates of Cloud Edge "C" from Image Converter Photograph, Shot #2464

Film Coordinates			Real-Space Coordinates		
	Lt. Curve	Rt. Curve		Lt. Curve	Rt. Curve
X	Y	Y	X	Y	Y
.0291	-.1332	.1284	.097	-.445	.429
.0541	-.1353	.1330	.181	-.452	.445
.0791	-.1386	.1387	.264	-.464	.464
.1041	-.1426	.1436	.348	-.477	.480
.1291	-.1506	.1504	.432	-.504	.503
.1541	-.1580	.1593	.515	-.528	.533
.1791	-.1639	.1667	.599	-.548	.558
.2041	-.1701	.1740	.683	-.569	.582
.2291	-.1763	.1814	.766	-.590	.607
.2541	-.1821	.1911	.850	-.609	.639
.2791	-.1903	.2018	.933	-.636	.675
.3041	-.2016	.2097	1.017	-.674	.701
.3291	-.2147	.2244	1.101	-.718	.750
.3541	-.2243	.2335	1.184	-.750	.781
.3791	-.2357	.2453	1.268	-.788	.820
.4041	-.2548	.2549	1.352	-.852	.852
.4291	-.2670	.2660	1.435	-.893	.890
.4541	-.2750	.2780	1.519	-.920	.930
.4791	-.2923	.2858	1.602	-.978	.956
.5041	-.3166	.3037	1.686	-1.059	1.032
.5291	-.3361	.3187	1.770	-1.124	1.066
.5541	-.3538	.3499	1.853	-1.183	1.170
.5791	-.3962	.3774	1.937	-1.325	1.262
.6041	*	.4153	2.020	-	1.389
.6291	*	.4467	2.104	-	1.494

*Cloud edge too indistinct to permit determination of coordinate.

During Shot

After Shot

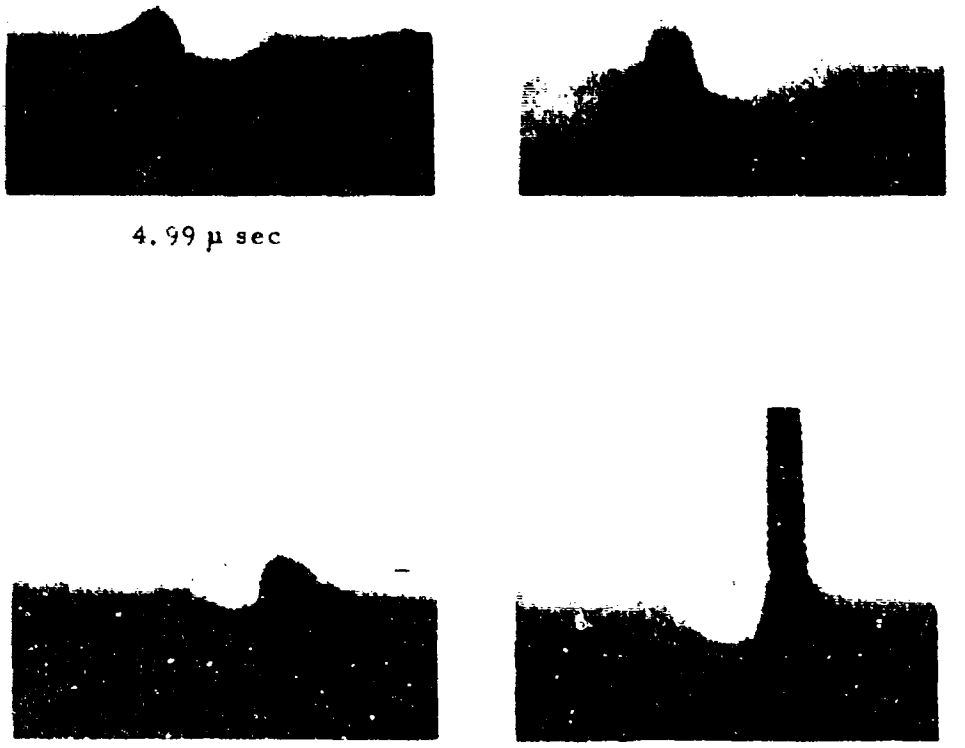

4.99 μ sec

5.28 μ sec

Fig. 37. Radiographs of Crater Profile During and After Shot #2384 (Vertical X-ray Setup)

During Shot

After Shot

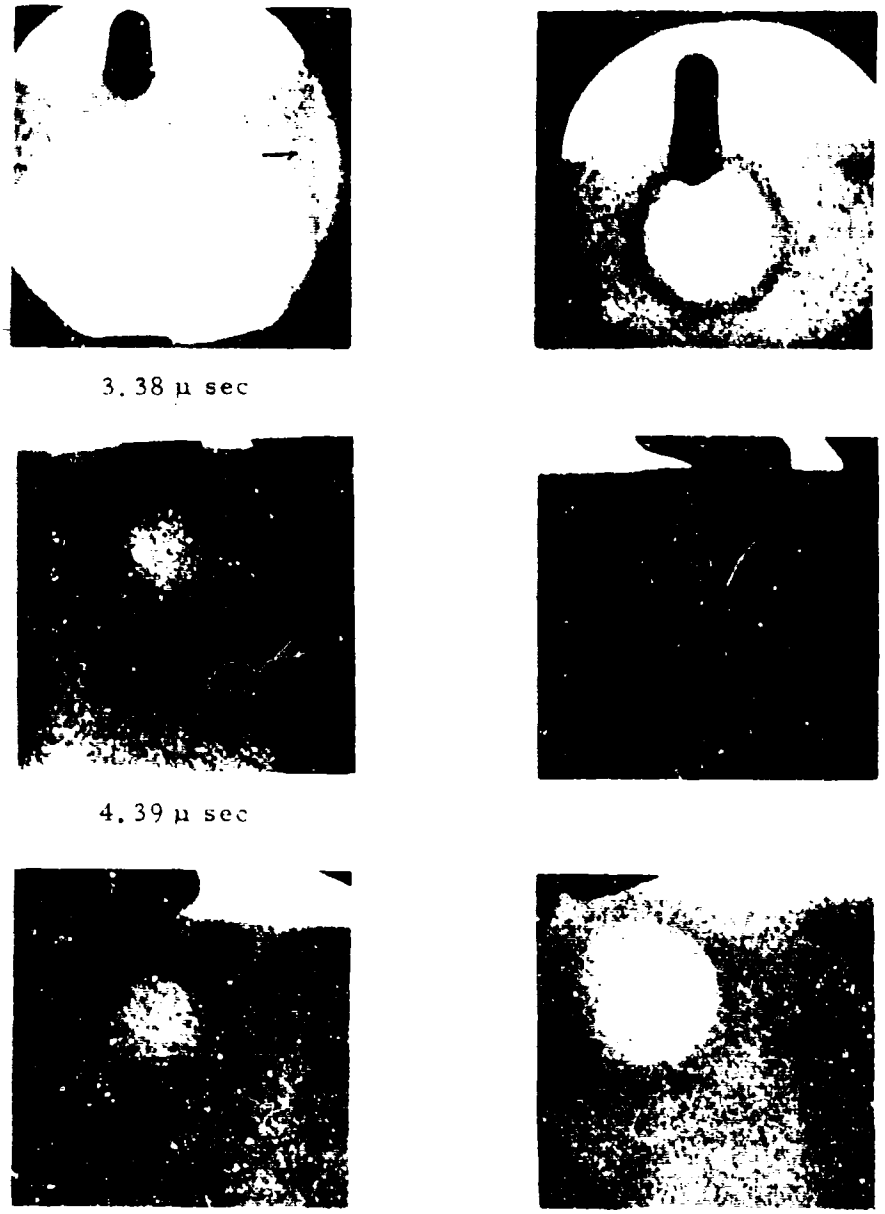

3.38 μ sec

4.39 μ sec

4.44 μ sec

Fig. 38. Radiographs of Crater Diameter During and After Shot #2384 (Horizontal X-ray Setup)

During Shot

After Shot

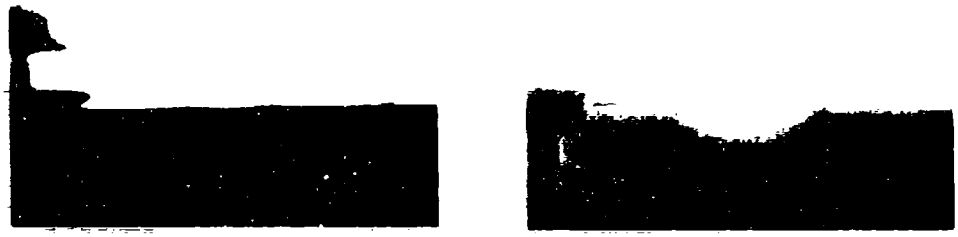

3.44 μ sec

4.78 μ sec

Fig. 39. Radiographs of Crater Profile During and After Shot #2385 (Vertical X-ray Setup)

During Shot

After Shot

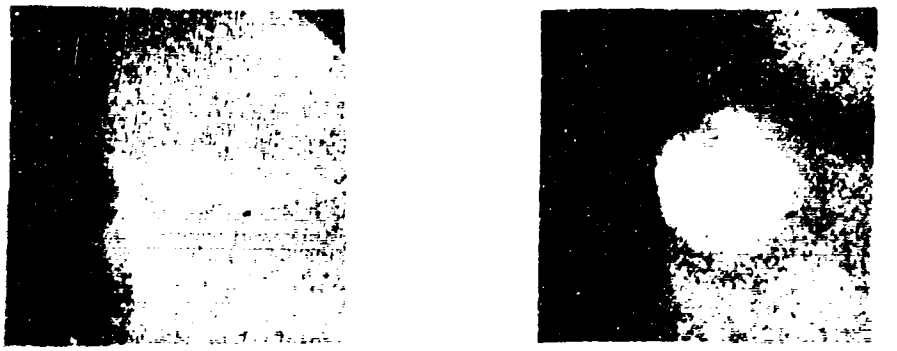

2.99 μ sec

3.21 μ sec

4.10 μ sec

Fig. 40. Radiographs of Crater Diameter During and After Shot #2385 (Horizontal X-ray setup)

During Shot

After Shot

37.00 μ sec

51.23 μ sec

Fig. 41. Radiographs of Crater Profile During and After Shot #2387 (Vertical X-ray Setup)

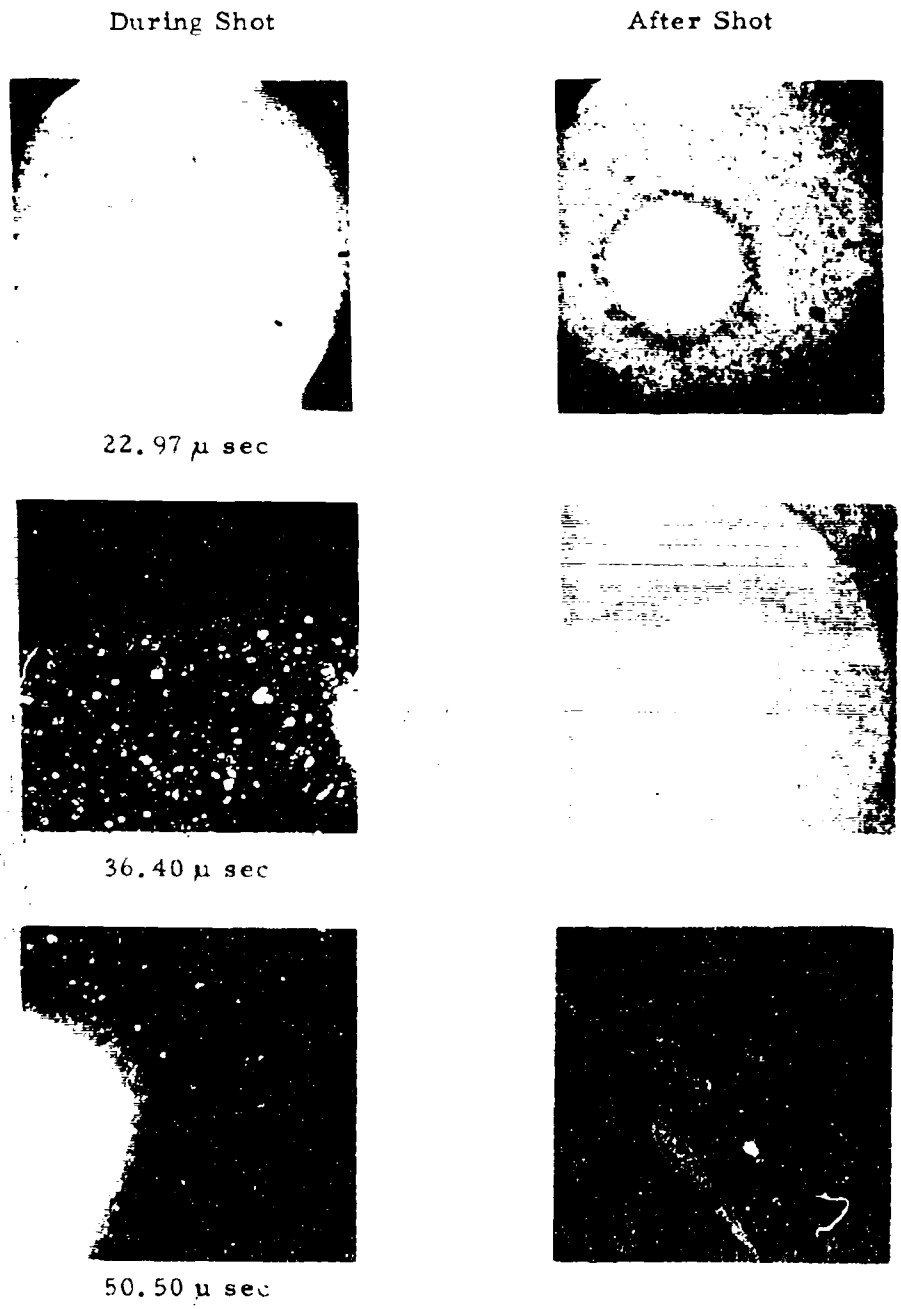

Fig. 42. Radiographs of Crater Diameter During and After Shot #2387 (Horizontal X-ray Setup)

actual shaft centerline position. All diameter measurements were made in the plane of the undisturbed target face. The depth and two diameter measurements for each of the six craters appear in Table XII. All measurements are in inches.

TABLE XII

Crater Measurement Raw Data

Shot Number	Depth	Diameter 1	Diameter 2
2384	.3554	.6446	.6566
2385	.3663	.6580	.6569
2386	.3635	.6496	.6454
2387	.3391	.6311	.6301
2463	.36[illegible]3	.6490	.6333
2464	.3413	.6239	.6354

Appendix C

Atmospheric Drag Effects

The results of both cloud-edge and discrete particle investigations suggested that the ejecta was being decelerated. To test this hypothesis, relationships between particle size, atmospheric pressure, and resultant drag were investigated. Work by Öpik (Ref 21) and MacCormack (Ref 17) provided the background for this investigation. For the size particles under consideration, Öpik finds that the drag force can be represented by

$$F_D = \frac{1}{4} K S \rho V^2 \qquad (1)$$

where F_D is the drag force, K is the drag coefficient, S is the area of minimum convex envelope of the body, ρ is the atmospheric density, and V is particle velocity (Ref 21:29-38). Öpik further points out that the particles can be treated as spheres; hence the equation can be rewritten

$$F_D = K \pi r^2 \rho V^2 \qquad (2)$$

where F_D, K, ρ, and V have the same meanings as in the previous equation, and r is the radius of the (assumed) spherical particle.

As atmospheric pressure (and therefore density) is reduced, the value of K changes. At relatively high atmospheric densities, K has a value of 0.5. In this area, hydrodynamic flow prevails, and the drag equation assumes the familiar form

$$F_D = \frac{1}{2} \pi r^2 \rho V^2 \qquad (3)$$

At very low atmospheric densities, free molecular flow exists. Here K attains its maximum value of 1. Values of K for both flow regimes and for the transition regime between are presented in Table XIII.

TABLE XIII

Kinetic Thickness and Drag Coefficient

$d = 0.75r/\lambda'$	K
0	1
1	0.75
2	0.625
4	0.562
∞	0.5
	(From Ref 21:38)

Here d is the average kinetic thickness of the aircap formed in front of the particle. The term λ' required to compute d represents the half-energy range of an air molecule at the velocity of the particle, or the range of travel required for the molecule to lose through collisions one-half its initial kinetic energy. For a particle velocity of 7 km/sec (taken to be a reasonable estimate of the velocity of early-time post-jetting-phase particles), $\lambda' \cong 6 \times 10^{-8}$ gm-cm$^{-2}/\rho$, where ρ is the atmospheric density measured in c. g. s. units (Ref 21:81).

To simplify the calculations, it will be assumed that nitrogen

molecules comprised 100% of the atmosphere in the target tank. From the ideal-gas equation of state, atmospheric densities in the target tank at 68°F were computed for pressures of 25.2 and .09 torr:

$$\rho_{25.2} = 3.86 \times 10^{-5} \text{ gm/cm}^3;$$

$$\rho_{.09} = 1.38 \times 10^{-7} \text{ gm/cm}^3$$

The appropriate values of λ' are then

$$\lambda'_{25.2} = \frac{6 \times 10^{-8}}{3.86 \times 10^{-5}} = 1.55 \times 10^{-3} \text{ cm};$$

$$\lambda'_{.09} = \frac{6 \times 10^{-8}}{1.38 \times 10^{-7}} = 4.35 \times 10^{-1} \text{ cm}$$

The deceleration of particles of characteristic dimension (diameter) of 10^{-1}, 10^{-2}, 10^{-3}, 10^{-4}, and 10^{-5} cm will be investigated.

Computer program sensitivity tests (Appendix D) indicated that a decrease in particle velocity of 5% would surely invalidate the computer output. Therefore, a 5% change in velocity was selected as the limit of investigation. Since the value of λ' is only weakly velocity-dependent, λ' and consequently K will be considered to remain constant over the velocity regime of interest.

From Newton's Second Law, Eq (2) can be rewritten

$$K \pi r^2 \rho_a V^2 = -\frac{4}{3} \pi r^3 \rho_b \frac{dV}{dt}$$

where ρ_a and ρ_b are the densities of the target tank atmosphere and the (assumed spherical) aluminum particle respectively.

Rewriting, $\frac{dV}{dt} = \frac{-3K}{4r} \frac{\rho_a}{\rho_b} V^2$

Since $V = \frac{dx}{dt}$, the equation can be rewritten

$$\frac{1}{V}\frac{dV}{dt} = \frac{dt}{dx}\frac{dV}{dt} = \frac{dV}{dx} = \frac{-3K\rho_a}{4r\rho_b} V$$

Rearranging for integration over a 5% velocity decrease

$$\int_{V_o}^{.95V_o} \frac{dV}{V} = \frac{-3K\rho_a}{4r\rho_b} \int_0^x dx \; ; \quad \ln .95 = \frac{-3K\rho_a}{4r\rho_b} x$$

Solving for x, the distance the particle travels in experiencing a 5% loss in velocity,

$$x = \frac{-4\rho_b}{3\rho_a} (\ln .95) \left(\frac{r}{K}\right) \qquad (4)$$

Values of particle travel for various-size particles at the two pressures of interest appear in Table XIV.

These computations are simplified in that ablation of the particle is ignored. However, the results for .09 torr compare favorably with results obtained by MacCormack who dealt with ablation. He concluded that in an atmosphere of 0.2 torr, particles with radii greater than 8×10^{-6} cm would not experience a 10% velocity loss from an original velocity of 10 km/sec over a time-span of 5 microseconds (Ref 17:13). They are also in general agreement with Carey's conclusion that a 0.25 mm particle will not decelerate appreciably over a distance of 30 cm in a pressure of 25.2 torr. (Ref 2:111).

TABLE XIV

Approximate Distances Traveled by Various Size Particles in Losing 5% of Initial Velocity of 7 km/sec in Atmospheric Pressures of 25.2 and .09 Torr

Pressure (torr)	Atmospheric Density (ρ_a) (gm/cm^3)	Particle Radius (r) (cm)	$d = \frac{.75\lambda'}{r}$	k	Distance Traveled (x) (cm)
25.2	3.86×10^{-5}	5×10^{-2}	2.32×10^{-2}	.994	2.39×10^{2}
25.2	3.86×10^{-5}	5×10^{-3}	2.32×10^{-3}	1.000	2.38×10^{1}
25.2	3.86×10^{-5}	5×10^{-4}	2.32×10^{-4}	1.000	2.38×10^{0}
25.2	3.86×10^{-5}	5×10^{-5}	2.32×10^{-5}	1.000	2.38×10^{-1}
25.2	3.86×10^{-5}	5×10^{-6}	2.32×10^{-6}	1.000	2.38×10^{-2}
.09	1.38×10^{-7}	5×10^{-2}	6.52×10^{0}	.500	1.33×10^{5}
.09	1.38×10^{-7}	5×10^{-3}	6.52×10^{-1}	.837	7.95×10^{3}
.09	1.38×10^{-7}	5×10^{-4}	6.52×10^{-2}	.984	6.76×10^{2}
.09	1.38×10^{-7}	5×10^{-5}	6.52×10^{-3}	.998	6.66×10^{1}
.09	1.38×10^{-7}	5×10^{-6}	6.52×10^{-4}	1.000	6.65×10^{0}

Appendix D

Computer Program Sensitivity Tests

Details of the computer program sensitivity tests (discussed in Chapter V) appear in Table XV. All values are presented in English units as program output.

TABLE XV

Detailed Results of Computer Program Sensitivity Tests

Test Conditions	Results								
	Point	Time (μsec)	% Error	Origin (in)	% Error	Ejection Angle (Deg)	% Error	Velocity (fps)	% Error
A. Correct Inputs (Standard for Comparison)	1	679.7	----	.08558	----	56.541	----	18860.3	----
	2	683.0	----	.08936	----	57.656	----	18364.0	----
	3	692.4	----	.09124	----	58.366	----	18084.6	----
	4	706.9	----	.09189	----	58.783	----	17968.4	----
	5	724.2	----	.09202	----	59.058	----	17937.1	----
B. Time of Curve A (TA) decreased by 6% of (TB-TA)	1	699.2	+2.9	.06523	-23.8	52.026	-8.0	21122.4	+12.0
	2	698.4	+2.2	.07277	-18.6	53.774	-6.7	20257.2	+10.3
	3	700.0	+1.1	.07836	-14.1	55.218	-5.4	19577.4	+8.2
	4	705.4	-0.2	.08214	-10.6	56.314	-4.2	19090.4	+6.2
	5	714.6	-1.3	.08459	-8.1	57.117	-3.3	18767.4	+4.6
C. TA Increased by 6% of (TB-TA)	1	653.8	-3.8	.10062	+17.6	60.215	+6.5	17070.7	-9.5
	2	669.4	-2.0	.10078	+12.8	60.541	+5.0	16993.0	-7.5
	3	690.7	-0.2	.09990	+9.5	60.613	+3.8	17062.4	-5.6
	4	715.4	+1.2	.09850	+7.2	60.537	+3.0	17225.7	-4.1
	5	740.5	+2.2	.09716	+5.6	60.448	+2.4	17408.1	-2.9

Table XV (Cont.)

Test Conditions	Point	Time (μsec)	% Error	Origin (in)	% Error	Ejection Angle (Deg)	% Error	Velocity (fps)	% Error
D. TA Increased by 2.4% of (TB-TA)	1	670.3	-1.4	.09211	+7.6	58.101	+2.8	18103.4	-4.0
	2	676.7	-0.9	.09453	+5.8	58.940	+2.2	17749.5	-3.3
	3	690.9	-0.2	.09510	+4.2	59.354	+1.7	17627.9	-2.5
	4	709.1	+0.3	.09489	+3.3	59.572	+1.3	17624.2	-1.9
	5	730.0	+0.8	.09429	+2.5	59.666	+1.0	17696.5	-1.3
E. TA Increased by 1.2% of (TB-TA)	1	674.6	-0.8	.08906	+4.1	57.367	+1.5	18457.3	-2.1
	2	679.6	-0.5	.09208	+3.0	58.328	+1.2	18041.1	-1.8
	3	691.3	-0.2	.09328	+2.2	58.885	+0.9	17842.6	-1.3
	4	708.0	+0.2	.09342	+1.7	59.185	+0.7	17792.8	-1.0
	5	726.9	+0.4	.09321	+1.3	59.376	+0.5	17809.3	-0.7
F. Curve "C" flattened by increasing y coordinate of all points above throat by 5%. Input times correct.	1	347.6	-48.8	.11588	+35.4	64.237	+13.6	12763.7	-32.3
	2	400.3	-41.4	.11238	+25.8	63.647	+10.4	13165.2	-28.3
	3	453.6	-34.5	.10871	+19.1	63.003	+7.9	13617.2	-24.7
	4	503.2	-28.8	.10536	+14.6	62.420	+6.2	14056.9	-21.8
	5	545.9	-24.6	.10270	+11.6	61.991	+5.0	14421.1	-19.6
G. Curve "C" altered as above. TA increased by 6% of (TB-TA)	1	303.0	-55.4	.12315	+43.9	66.257	+17.2	11841.3	-37.2
	2	379.9	-44.4	.11808	+32.1	65.237	+13.1	12458.8	-32.2
	3	449.9	-35.7	.11327	+24.1	64.282	+10.1	13076.4	-27.7
	4	509.8	-27.9	.10918	+18.8	63.498	+8.0	13626.2	-24.2
	5	*	----	*	----	*	----	*	----

* Program failed to find a solution

Unclassified
Security Classification

DOCUMENT CONTROL DATA R&D

(Security classification of title, body of abstract and indexing annotation must be entered when the overall report is classified)

1. ORIGINATING ACTIVITY (Corporate author)	2a. REPORT SECURITY CLASSIFICATION
Air Force Materials Laboratory Wright-Patterson AFB, Ohio 45433	Unclassified
	2b. GROUP

3. REPORT TITLE

INVESTIGATION OF CRATER GROWTH AND EJECTA CLOUD RESULTING FROM HYPERVELOCITY IMPACT OF ALUMINUM SPHERES ON THICK ALUMINUM TARGETS

4. DESCRIPTIVE NOTES (Type of report and inclusive dates)

Technical Report

5. AUTHOR(S) (Last name, first name, initial)

Smith, Russell H., Lt. Col., USAF

6. REPORT DATE	7a. TOTAL NO. OF PAGES	7b. NO. OF REFS
June 1968	118	30

8a. CONTRACT OR GRANT NO.	9a. ORIGINATOR'S REPORT NUMBER(S)
b. PROJECT NO. 7360	AFML-TR-68-175
c. Task No. 736006	9b. OTHER REPORT NO(S) (Any other numbers that may be assigned this report) GSF/mc/68-10
d.	

10. AVAILABILITY/LIMITATION NOTICES

This document has been approved for public release and sale; its distribution is unlimited.

11. SUPPLEMENTARY NOTES	12. SPONSORING MILITARY ACTIVITY Air Force Materials Laboratory Air Force Systems Command Wright-Patterson AFB, Ohio 45433

13. ABSTRACT

An experimental investigation was conducted of crater growth and ejecta cloud formation from the impact of 3.2 mm aluminum spheres on thick aluminum targets at 7 km/sec. Crater growth and transient shape were determined through sequential flash x-rays. Growth followed a decaying exponential pattern, and the tangent angle to the crater wall at the target surface remained virtually constant. Relationships between ejecta-cloud parameters and crater diameters were investigated. Cloud-edge motion was determined and an effort made to determine particle origin. Velocities of discrete particles in the cloud were determined. No direct relationship between cloud parameters and crater dimensions could be established.

DD FORM 1 JAN 64 1473

Unclassified
Security Classification

KEY WORDS	LINK A		LINK B		LINK C	
	ROLE	WT	ROLE	WT	ROLE	WT
Impact Hypervelocity Impact Cratering						

INSTRUCTIONS

1. ORIGINATING ACTIVITY: Enter the name and address of the contractor, subcontractor, grantee, Department of Defense activity or other organization *(corporate author)* issuing the report.

2a. REPORT SECURITY CLASSIFICATION: Enter the overall security classification of the report. Indicate whether "Restricted Data" is included. Marking is to be in accordance with appropriate security regulations.

2b. GROUP: Automatic downgrading is specified in DoD Directive 5200.10 and Armed Forces Industrial Manual. Enter the group number. Also, when applicable, show that optional markings have been used for Group 3 and Group 4 as authorized.

3. REPORT TITLE: Enter the complete report title in all capital letters. Titles in all cases should be unclassified. If a meaningful title cannot be selected without classification, show title classification in all capitals in parenthesis immediately following the title.

4. DESCRIPTIVE NOTES: If appropriate, enter the type of report, e.g., interim, progress, summary, annual, or final. Give the inclusive dates when a specific reporting period is covered.

5. AUTHOR(S): Enter the name(s) of author(s) as shown on or in the report. Enter last name, first name, middle initial. If military, show rank and branch of service. The name of the principal author is an absolute minimum requirement.

6. REPORT DATE: Enter the date of the report as day, month, year; or month, year. If more than one date appears on the report, use date of publication.

7a. TOTAL NUMBER OF PAGES: The total page count should follow normal pagination procedures, i.e., enter the number of pages containing information.

7b. NUMBER OF REFERENCES: Enter the total number of references cited in the report.

8a. CONTRACT OR GRANT NUMBER: If appropriate, enter the applicable number of the contract or grant under which the report was written.

8b, 8c, & 8d. PROJECT NUMBER: Enter the appropriate military department identification, such as project number, subproject number, system numbers, task number, etc.

9a. ORIGINATOR'S REPORT NUMBER(S): Enter the official report number by which the document will be identified and controlled by the originating activity. This number must be unique to this report.

9b. OTHER REPORT NUMBER(S): If the report has been assigned any other report numbers *(either by the originator or by the sponsor)*, also enter this number(s).

10. AVAILABILITY/LIMITATION NOTICES: Enter any limitations on further dissemination of the report, other than those imposed by security classification, using standard statements such as:

(1) "Qualified requesters may obtain copies of this report from DDC."

(2) "Foreign announcement and dissemination of this report by DDC is not authorized."

(3) "U. S. Government agencies may obtain copies of this report directly from DDC. Other qualified DDC users shall request through _____."

(4) "U. S. military agencies may obtain copies of this report directly from DDC. Other qualified users shall request through _____."

(5) "All distribution of this report is controlled. Qualified DDC users shall request through _____."

If the report has been furnished to the Office of Technical Services, Department of Commerce, for sale to the public, indicate this fact and enter the price, if known.

11. SUPPLEMENTARY NOTES: Use for additional explanatory notes.

12. SPONSORING MILITARY ACTIVITY: Enter the name of the departmental project office or laboratory sponsoring *(paying for)* the research and development. Include address.

13. ABSTRACT: Enter an abstract giving a brief and factual summary of the document indicative of the report, even though it may also appear elsewhere in the body of the technical report. If additional space is required, a continuation sheet shall be attached.

It is highly desirable that the abstract of classified reports be unclassified. Each paragraph of the abstract shall end with an indication of the military security classification of the information in the paragraph, represented as *(TS)*, *(S)*, *(C)*, or *(U)*.

There is no limitation on the length of the abstract. However, the suggested length is from 150 to 225 words.

14. KEY WORDS: Key words are technically meaningful terms or short phrases that characterize a report and may be used as index entries for cataloging the report. Key words must be selected so that no security classification is required. Identifiers, such as equipment model designation, trade name, military project code name, geographic location, may be used as key words but will be followed by an indication of technical context. The assignment of links, rules, and weights is optional.

Unclassified
Security Classification